Macroporous materials: microfluidic fabrication, functionalization and applications

Bingjie Wang,[ab] Pepijn Prinsen,[b] Huizhi Wang,[c] Zhishan Bai,*[a] Hualin Wang,[a] Rafael Luque[b] and Jin Xuan*[c]

This article provides an up-to-date highly comprehensive overview (594 references) on the state of the art of the synthesis and design of macroporous materials using microfluidics and their applications in different fields.

1. Introduction

A number of materials fabricated by humankind are nature inspired. Porous materials, one of the most attractive ones, are found in sediments, pollens, *etc.* Both well-ordered and low-ordered structures can lead to a wide variety of applications, *e.g.* graphite used in absorptive separations. The fabrication

[a] State Environmental Protection Key Laboratory of Environmental Risk Assessment and Control on Chemical Process, School of Mechanical and Power Engineering, East China University of Science and Technology, Shanghai 200237, China. E-mail: baizs@ecust.edu.cn, wanghl@ecust.edu.cn

[b] Departamento de Quimica Organica, Universidad de Cordoba, Campus de Rabanales, Edificio Marie Curie (C-3), Ctra Nnal IV-A, Km 396, Cordoba, E14014, Spain. E-mail: q62alsor@uco.es

[c] School of Engineering and Physical Sciences, Heriot-Watt University, Edinburgh, EH14 4AS, UK. E-mail: j.xuan@hw.ac.uk

of novel artificial functional porous materials often comes in waves, impulsed by the development of novel research areas, *e.g.* water treatment, drug delivery, fuel cells, *etc.* According to the IUPAC defined pore dimensions, porous materials are classified as microporous, mesoporous and macroporous structures, with the corresponding pore sizes of <2 nm, 2–50 nm and >50 nm, respectively.[1–4] They can be applied as stationary phases in separation science,[5,6] resins for solid phase organic and peptide synthesis,[7] ion-exchange resins,[8] scavengers,[9] enzyme supports[10] and catalysts.[11] Important parameters of these materials, in view of their particular application, are: average pore size, average particle diameter, mean effective porosity, specific surface area, particle shape, *etc.* Porous materials are fabricated with a wide range of morphologies, from simple porous spheres with a smooth "skin"[12–17] to open cellular structures,[18,19] from dense to hollow porous particles,[14,20,21] from zero dimensional spheres[22–24] to

Bingjie Wang received his BS degree from East China University of Science and Technology (ECUST) in 2013. Following this, he has been undertaking a PhD study under the supervision of Prof. Zhishan Bai at ECUST and Dr Jin Xuan at Heriot-Watt University. Currently, he is working as a visiting student in the group of Prof. Rafael Luque at the University of Cordoba for PhD research. His research interests focus on the microfluidic-based fabrication, multifunctionalization and performance evaluation of advanced materials for wastewater treatment and catalytic application.

Bingjie Wang

Dr Pepijn Prinsen recently started to work as a postdoctoral researcher in the Group of Nanoscale Chemistry and Biomass/Waste Valorization (University of Cordoba, Spain). In 2005, he graduated as a Bioengineer at the University of Ghent (Belgium). He obtained an International PhD in Chemistry in 2013 at the University of Seville in the Group of Lignocellulosic Materials of Industrial Interest at the Institute of Natural Resources and Agrobiology, followed by a postdoctoral research project on lignin depolymerisation and carbon synthesis in the Group of Heterogeneous Catalysis and Sustainable Chemistry (Van't Hoff Institute for Molecular Sciences, University of Amsterdam, The Netherlands, 2014–2016).

Pepijn Prinsen

This journal is © The Royal Society of Chemistry 2017

Chem. Soc. Rev., 2017, **46**, 855–914 | 855

one dimensional rods,[19,25,26] from irregular structures[27] to well-designed scaffolds[28,29] and so on.

Many applications require an open cellular structure with a specific average pore size and distribution.[19] In particular, the need for hierarchical structures pleads for research in the field of micro-manufacturing. Hierarchical structures are those whose pores exist on different length scales from micro- to meso- to macropores regardless of their assembly being ordered or not. Obtaining hierarchical porosity is not a straightforward process; often it is found that the macroporous structure collapses during the creation of micropores or otherwise. Hierarchical porous systems have obvious advantages over monomodal ones for several reasons.[30–46] In the first place, the hierarchy in porosity enables the selective entrance and exit of chemicals with different molecular dimensions while reducing the diffusion limitation effects.[47] To understand this, it can be compared with the time needed for people to arrive at work by car; no matter the amount of available car parking areas (micropores), people will not arrive in time when the highways (macropores) or the exits to parking areas (mesopores) are not well designed. In this comparison, 'people' does not only refer to chemicals but also to energy such as electric currents[30] or optical signals. A porous hierarchy facilitates the interaction with substrates of different sizes such as small molecules, biomacromolecules and even nanoparticles, and it allows better functionalization of the material itself.

Among others, suspension, precipitation, dispersion and seeded emulsion polymerization, membrane/microchannel emulsification and microfluidics are the main techniques for the fabrication of porous materials. Pore formation can be regarded as a process of phase separation, either in suspension or in swelling and polymerization. The pore size can be indirectly controlled by regulating several parameters, for instance, the effect of the ratio of a cross-linking monomer to porogen, the reaction temperature, the swelling ratio of the seed polymer, *etc.*[48–53] However, when it comes to precise and strict control of the final morphology, the microfluidics technique is more attractive. Flow lithography, which combines microfluidics and photolithography, has emerged as

Huizhi Wang received her PhD in Mechanical Engineering from the University of Hong Kong in 2012. She worked as a Postdoctoral Fellow at the University of Hong Kong during 2012–2014. Huizhi joined the School of Engineering and Physical Sciences at Heriot-Watt University as an assistant professor in 2014. Her research interest lies in electrochemistry for energy storage and carbon conversion.

Huizhi Wang
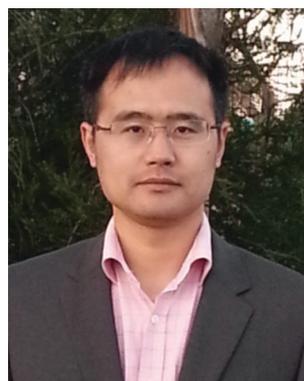
Zhishan Bai received his PhD in Chemical and Mechanical Engineering from East China University of Science and Technology (ECUST) in 2009. He is currently a professor in School of Mechanical and Power Engineering at ECUST. He won the second prize of the National Scientific and Technological Progress Award, P. R. China, in 2007 and 2009. His research interests lie in novel adsorbent synthesis and optimization for

Zhishan Bai

wastewater treatment, efficient separation and reuse of multiphase pollutants, and the separation mechanism of complex pollutants.

Rafael Luque is Deputy Head of Department from Departamento de Quimica Organica at Universidad de Cordoba, with a significant experience in biomass and waste valorisation practises to materials, fuels and chemicals as well as flow and nanoscale chemistry and heterogeneous catalysis. He has published over 280 peer-reviewed research articles, filed 3 patent applications and edited 8 books as well as numerous contributions to book chapters and keynote and plenary lectures in scientific events worldwide.

Rafael Luque

Jin Xuan was born in Zhejiang, China, in 1984. He obtained his PhD degree in Mechanical Engineering from The University of Hong Kong in 2011. He was a Faculty Member in East China University of Science and Technology, and a visiting researcher at The University of Hong Kong and City University of Hong Kong during 2011–2014. In 2014, he moved his academic career to U.K., taking his current position as an assistant professor at Heriot-Watt University.

Jin Xuan

Dr Xuan's research interests include microsystems, microfluidics and microreactors for energy and carbon conversion and management.

a novel and efficient approach to fabricate complicated microparticles of equal size and specific shape in a continuous way.[54]

To date, several excellent reviews on the fabrication and applications of porous microparticles have been published already.[47,55–75] The review by Okay[55] in 2000 dealt with particle characteristics and fabrication methods of macroporous copolymers, but without an in-depth discussion of applications. Serra[76] reviewed the use of microfluidic devices for the fabrication of microparticles, focusing on the final particle morphology as a function of the device geometry. In 2010, Kim[71] reviewed the state-of-the-art fabrication of microparticles and microcolloids by microfluidic techniques, but with a focus on biology rather than on more widespread applications. In 2012, Gokmen[58] published a comprehensive and complete review on porous polymer particles including their synthesis, characterization, functionalization and applications. However, the microfluidic method was introduced only briefly. Besides, it was not clear whether to compare the latter in terms of pore sizes. Testouri[75] reviewed how millifluidic techniques can be used to generate porous solids with highly monodisperse and ordered pore structures and how to construct a versatile lab-on-a-chip. In summary, the existing reviews deal with different fabrication methods of porous materials in general. The reviews that describe the microfluidic method more in detail focus mainly on the fabrication of spherical morphologies and their deformations, such as hemispheres or rods. However, a comprehensive review pinpointing the fabrication of macroporous materials using microfluidic techniques is still lacking. This review aims to provide these insights, including their fabrication, functionalization and application. Moreover, not only randomly distributed macroporous materials are described, but also the inverse-opals and scaffolds with well-ordered uniform macropores. Moreover, attention is paid to materials with hierarchical porosity, as mentioned above. Ultimately, we outline the bottlenecks and future developments in this particular field.

2. Microfluidic devices

In 1998, Whitesides introduced a soft lithography technique to design polydimethylsiloxane (PDMS) devices,[77,78] which enabled to study the fluid behavior at laminar flow in narrow well-defined channels, referred to as microfluidics today. PDMS based chips have become popular devices for microparticle production. Nevertheless, their 2D characteristics and incompatibility with several organic solvents limit their applications. Weitz and co-workers[79–81] introduced glass capillary-based devices to transform initial 2D microfluidic geometries into truly 3D ones. However, the fabrication of these devices can be tedious and difficult. Both types of devices were further improved,[82–84] but recently Weitz' team presented a novel route to coat the inner walls of PDMS devices with glass,[85] reducing the complications caused by swelling. Other studies used pure glass[86] or organic polymers[87–89] to replace PDMS. Serra et al.[90,91] utilized a steel tee connected to the discrete phase pipe making it possible to use capillaries instead of discrete phase needles.[92–95] Two main types of microfluidic devices exist depending on the polymerization time: (1) emulsification of liquid monomers, immiscible with another fluid phase, polymerization and generation of disperse droplets and (2) direct polymerization through continuous flow photolithography.[76]

2.1. Emulsification based devices

Emulsification can be carried out in PDMS devices and in capillary devices (Fig. 1). In the PDMS devices, both continuous and dispersed phases flow inside microchannels, while in the capillary ones the dispersed phase is introduced by a capillary of small dimensions inserted into the tube where the continuous phase flows.

2.2. Flow photolithography based devices

Flow photolithography[54] based devices employ a transparency mask which can be designed with various morphologies to
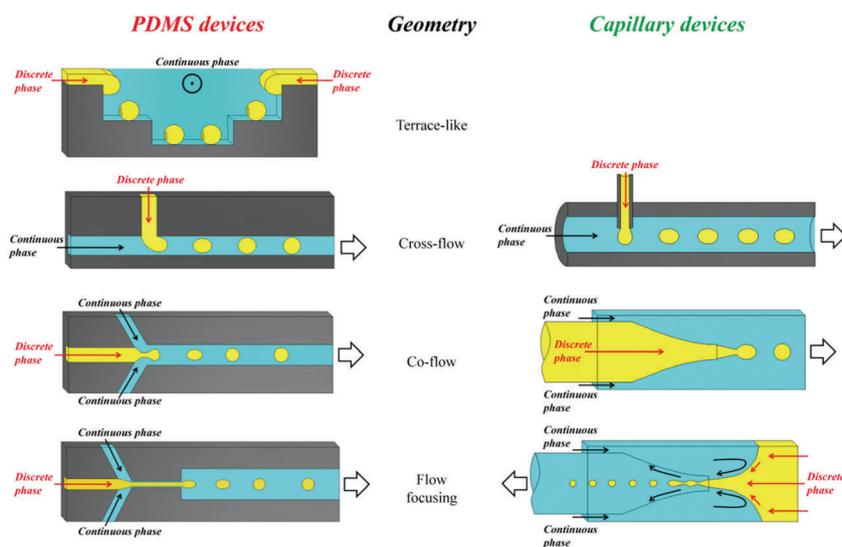

Fig. 1 (left) PDMS and (right) glass capillary microfluidic devices. Both phases are pumped at constant rates by the use of syringe pumps. The largest arrows point the direction of the total flow and droplet motion.
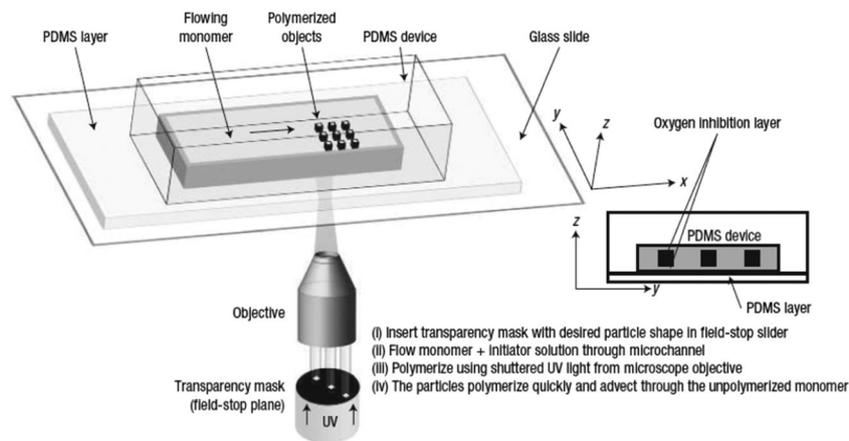
This journal is © The Royal Society of Chemistry 2017

Chem. Soc. Rev., 2017, 46, 855–914 | 857

Fig. 2 Scheme of continuous flow photolithography. Reproduced with permission from ref. 54. Copyright 2006 Nature Publishing Group.

polymerize and "print" the desired particle (Fig. 2). This technique relies on: (1) quick polymerization avoiding random shape deformation during irradiation and (2) oxygen permeation to form a thin oxygen inhibition layer in the PDMS microchannel avoiding the formation of sticky particles.

3. Fabrication methods of macroporous particles

Macroporous polymer resins have a permanent well-defined porous structure comprising pores in the size range of 10–10 000 Å.[53,55,96] Their preparation methods can be divided into 2 types: synthesis of monolithic resins and synthesis of particulate materials.[2,97–108] Table 1 compares several fabrication methods.

The resins can be applied either as porous monoliths[99,102,121–123] or as porous beads.[124] Rigid monoliths perform better in high-throughput separation processes and in catalytic reactions.[2,98–103] Unfortunately, they suffer from high initial flow resistance and alter ions in the breakthrough curve. In contrast, the size distribution of particulate macroporous resins obtained by milling macroscopic materials to form irregular particles is controlled by subsequent fractionations.[125] Though easy to fabricate, these particles show poor packing behavior and may block the column due to the presence of tiny secondary particles.[97] Alternatively, heterogeneous techniques such as suspension polymerization can be practical and useful for the synthesis of microspheres with diameters in the range of 0.1–1.5 mm and relatively broad size distributions.[12,55]

Suspension polymerization[53,55,96] and seeded emulsion polymerization[104,105] are among the most common preparation methods. In the former, drops of a mixture of a monomer, an initiator and an inert solvent (porogen) are dispersed in the immiscible continuous phase aided by vibration jetting, stirring or sonication. Often, the residual porogen is more miscible with the monomer rather than with the polymer phase. Residual porogens and monomers can be removed by solvent extraction or steam distillation, while enhancing the particle porosity. Generally, particles <200 μm are obtained with a broad range

of sizes, depending on the precise control of the emulsification process and the hindrance of droplet coalescence in the poly-merization stage. In contrast, seeded emulsion polymerization can render polymer particles <50 μm with more narrow size distributions. This occurs in 2 steps:[104–107] (1) quick swelling of monodisperse latex emulsions (seeds) followed by polymeriza-tion to solid particles and (2) removal of immiscible solvent residues to form a porous structure. Using seed particles with a low cross-linking degree is time-consuming, especially when particles >100 μm are envisioned. For macroporous particles with diameter <10 μm, precipitation polymerization in organic solvents can be used. For instance, toluene and xylene were used as co-solvents in acetonitrile to fabricate monodisperse highly cross-linked divinylbenzene particles.[108]
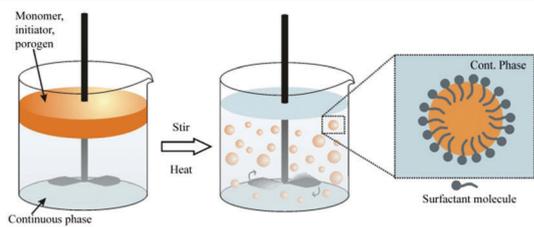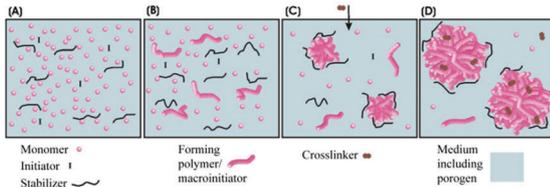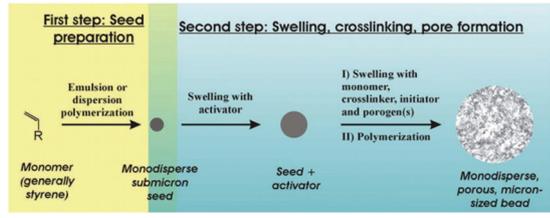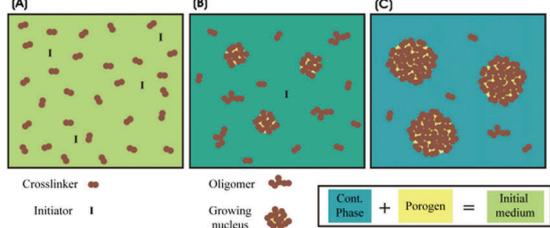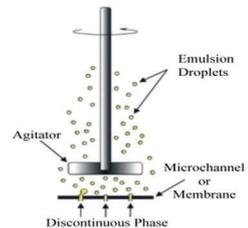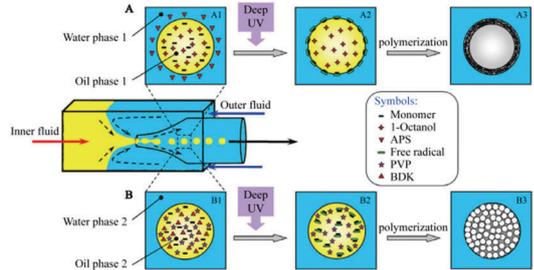
Advantages of microfluidic devices include low reagent consumption, facile mass/heat transfer, high safety and a high surface-area-to-volume ratio, with various outstanding features superior to conventional approaches.[126–131] Most importantly, the size distribution of the macroporous particles obtained by microfluidic synthesis can be controlled more precisely thanks to the flow-focusing mechanism of monomer emulsification. Besides, on-chip continuous polymerization prevents droplet coalescence. Particles synthesized by microfluidic synthesis have a finer and more ordered internal structure. However, the generation of particles with diameters in the range of 50–100 μm employing microfluidic methods may be more challenging; particles fab-ricated by suspension polymerization[132] show specific surface areas around 400 m^2 g^{-1} compared to only 30 m^2 g^{-1} for particles with the same composition obtained by the micro-fluidic technology.[133]

4. Microfluidic methods for the preparation of macroporous particles

Recently, microfluidic techniques have been employed using single setup devices (lab-on-a-chip) to produce monodisperse porous particles.[133,134] The microfluidic technique is an advanced version of conventional suspension polymerization, where

858 | Chem. Soc. Rev., 2017, 46, 855–914

This journal is © The Royal Society of Chemistry 2017

Table 1 Comparison of different fabrication methods of macroporous particles

Method (discovery)	Diameter of beads (μm)	Minimum CV of beads	Fabrication easiness/cost	Schematic illustration	Ref.
Suspension polymerization (1920s)	5–2000	Very high	Easy/cheap		55, 58, 59, 97 and 109–112
Dispersion polymerization (1970s)	0.1–20	2–3%	Easy/cheap		55, 58, 59, 110, 111, 113 and 114
Seeded suspension polymerization (1980s)	0.5–200	2–3%	Cheap/time consuming		55, 58, 97 and 110
Precipitation polymerization (1990s)	0.1–8	2–3%	Easy/costly		55, 58, 110, 111, 115 and 116
Membrane/ microchannel emulsification (1990s)	10–1000	10% (membrane) or 2–3% (channel)	Difficult/ costly		58, 117 and 118
Microfluidics (2000s)	10–1000	<1%	Costly device		18, 69, 70, 76, 119 and 120

monomer droplets are formed one by one in a controlled and reproducible manner. In general, droplet fabrication between 2 immiscible liquid phases can be obtained by various setups such as T-junction (also known as cross-flow[135]), flow focusing or co-flow geometries.[81] By a precise selection of the discrete phase, various morphologies can be obtained including non-porous particles,[126] capsules[136] and porous particles.[28,126,133,134] According to the pore formation mechanism, microfluidic methods are divided into 5 methods (Fig. 3): polymerization with/without porogens, sacrificial template, flow reaction, self-assembly and
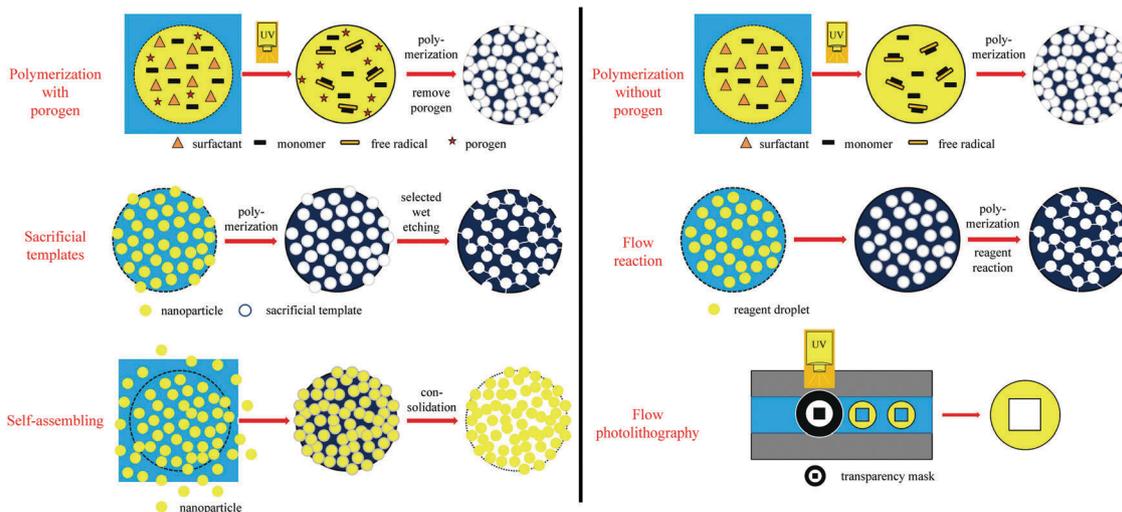
This journal is © The Royal Society of Chemistry 2017

Chem. Soc. Rev., 2017, 46, 855–914 | 859

Fig. 3 Schematic representation of microfluidic pore formation mechanisms of macroporous particles.

Table 2 Detailed comparison between the 5 microfluidic-based porous particle fabrication methods

Microfluidic-based porous particle fabrication methods	Merits	Demerits	Applicability
Polymerization with porogens	Wide universality Wide variety of porogens	Need post-processing to obtain a porous structure Pores' random distribution Unmanageable pore size	Radially "opened" macroporous particles with regular shape
Polymerization without porogens	Without post-processing	For specific phase component Pores' random distribution Unmanageable pore size	Radially "skin" or "opened" macroporous particles with regular shape
Sacrificial templates	Excellent pore shape Uniform pore size	Complicated process	Ordered or radially hierarchical porous particles with regular or irregular shape
Flow reaction	High porosity	For specific phase component and reaction Unstable pores' formation	Radially "skin" or "opened" macroporous particles with regular shape
Self-assembling	High porosity	Unmanageable particle shape Pores' random distribution Unmanageable pore size	Radially "opened" macroporous particles with regular or irregular shape
Flow photolithography	Customized particle shape Customized pore shape and distribution	High cost of designed photomask Low-yield	Customized ordered or hierarchical porous particles with regular or irregular shape

flow lithography. Besides, a detailed comparison between the different microfluidic-based porous particle fabrication methods is included (Table 2).

4.1. Radially macroporous particles

4.1.1. "Skin" or "closed" macroporous particles. "Skin" particles, also denominated "closed" macroporous particles, are microparticles with pores having their interior area mostly hindered. These morphologies can be obtained by varying the monomer composition, the chemical reagent dosage, the conditions (reaction time, temperature, *etc.*) and the pore-formation mechanism (porogens, chemical reaction, self-assembly, *etc.*). However, some molecules with certain dimensions can permeate this skin and reach the interior of the beads.[12–15,21,132,137] Further classification is addressed in this review: smooth "skin" microspheres and golf-ball-shaped microparticles.

4.1.1.1. Smooth "skin" spheres. Smooth "skin" spheres have their surface covered with a thin dense layer with some small pores, if any. Ford *et al.*[15] reported the formation of a dense and smooth layer when using (chloromethyl) styrene and divinylbenzene added in 4-methyl-2-pentanol. Detailed mechanistic information on particle formation lacked in the study. Pelzbauer *et al.*[13] fabricated a similar architecture on the surface of poly(glycidyl dimethacrylate–ethylene methacrylate) macroporous particles when cyclohexanol or cyclohexanol–dodecanol was added as a porogen. They discovered that the formation of the smooth "skin" can be suppressed by tuning the polymer composition. Dubinsky *et al.*[17] synthesized poly(glycidyl methacrylate–ethylene dimethacrylate) (poly(GMA–EGDMA)) droplets using dioctyl phthalate (DOP), diisodecyl phthalate (DDP) and their mixtures as porogens. Subsequently, the droplets were exposed to UV-irradiation for 60 s on-chip and 180 s off-chip after polymerization. Then, the porogen liquids were removed
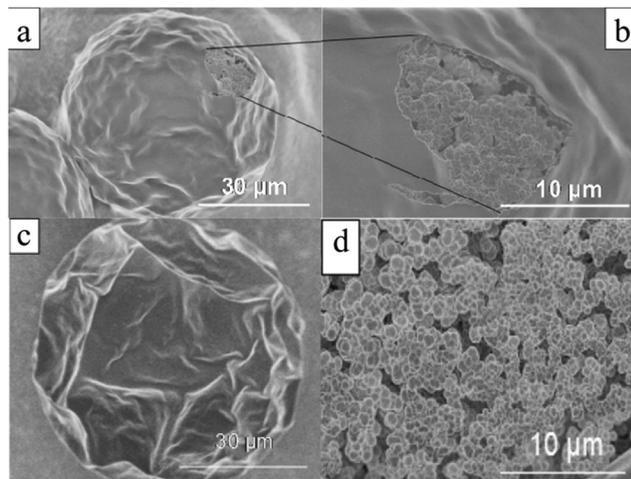
860 | *Chem. Soc. Rev.*, 2017, **46**, 855–914

This journal is © The Royal Society of Chemistry 2017

Fig. 4 SEM images of (a and c) surface and (b and d) internal structure of "skin" macroporous poly(GMA–EGDMA) particles, synthesized in the presence of (a and b) DBP/DOP 1:1 (v/v) and (c and d) DOP (0.5 wt% Triton X-100). Reproduced with permission from ref. 17. Copyright 2009 American Chemical Society.

Fig. 6 SEM images of (a) broken porous microparticles with a smooth surface and internal porous structure, (b) hemispherical microparticles, (c) triangular microparticles with an inclined side wall and (d) stellate microparticles with a curved surface. Scale bars are 1 μm (a) and 10 μm (b–d). Reproduced with permission from ref. 140. Copyright 2014 Wiley-VCH.

by washing microparticles with methanol and acetone. They observed smooth "skinned" surfaces and had some control over the internal particle structure (Fig. 4).

The employment of porogens leads to porosity development,[18,138] but it imposes an extra step for the removal of these agents. Watanabe et al.[139] reported the controlled preparation of polyelectrolyte particles in the 10–100 μm range through selective solvent extraction in a cross-flow microfluidic device. Mixtures of poly(styrene sulfonate) and water (dispersed phase) were introduced into the T-junction to form plugs in hexadecane (continuous phase). Subsequently, the obtained plugs were introduced into methyl ethyl ketone which is miscible with hexadecane and water but not with poly(styrene sulfonate) in a flow-focusing microchannel (in situ precipitation) or in a prepared vessel (ex situ precipitation) (Fig. 5a and b). Smooth "skin" macroporous particles were obtained (Fig. 5c) with a gradient internal porous structure (Fig. 5d).
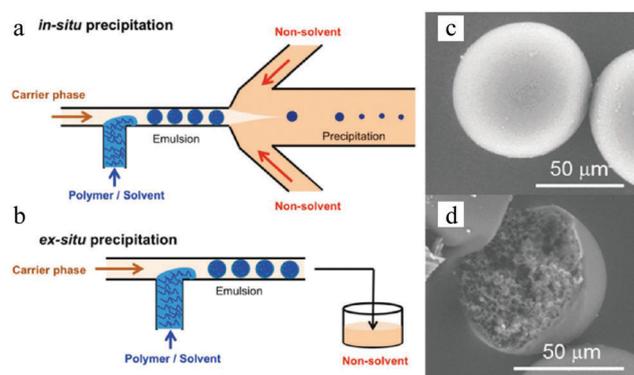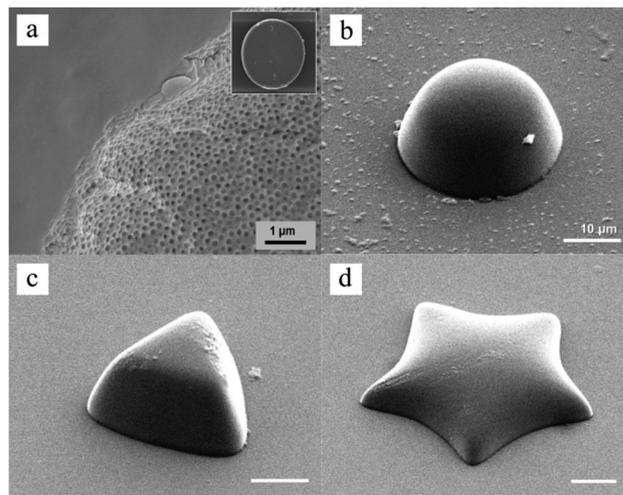

Fig. 5 (left) Illustration of (a) in situ and (b) ex situ preparation via microfluidic emulsification, precipitation and solvent extraction. (right) SEM images of the (c) smooth "skin" surface and (d) internal structure. Reproduced with permission from ref. 139. Copyright 2014 American Chemical Society.

Besides, Sim et al.[140] fabricated microparticles whose top or side surface was not flat but curved, such as circular, square, triangular and stellate microdisks (Fig. 6a–d), by introducing a novel double-layered PDMS microfluidic device, combining conventional photolithography and multilayer soft-lithography (microfluidic molding). Two straight control channels, used for pneumatic actuation of the membrane to mold and release the particles, were situated on the top layer while a T-junction channel, used for suspension flow, was integrated in the bottom layer. Interestingly, by controlling the pressurization in the top channel, the membrane was either deformed to confine the suspension into the designed shape and then polymerized by UV-irradiation or recovered to the original shape by releasing the obtained particles. Finally, microparticles could exit through the bottom channel.

The cycle of molding, polymerization and particle release could only be achieved by pneumatic force in the microfluidic device. By introducing a photo curable suspension of silica nanoparticles in the microfluidic molding process and subsequent selective wet-etching of the silica nanoparticles with a HF solution, a polymerized matrix with regular pores and structural colors was obtained.

Unlike the works of Pelzbauer et al.[13] and Dubinsky et al.[17] in which porogens were used to obtain closed macroporous particles, more recently, Udoh et al.[141] employed a microfluidic solvent extraction approach to prepare "skin" polymer particles (Fig. 7). At the same time, they also deeply investigated the effect of polymer solution thermodynamics in the particle fabrication process by comparing two different non-solvents (ethyl acetate (EA) and methyl ethyl ketone (MEK)) in the extraction of a polymer/solvent (NaPPS/H_2O) system. The outstanding control of particle size and closed porous structure verified that the solvent extraction method is more convenient than ones that need conventional porogens or a complex post-processing process.
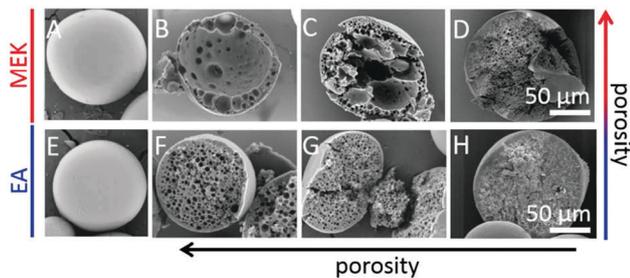
This journal is © The Royal Society of Chemistry 2017

Chem. Soc. Rev., 2017, 46, 855–914 | 861

Fig. 7   SEM images of (A and E) external surface and (B–D and F–H) cross sections of "skin" polymer particles obtained by extraction in MEK and EA. (A, C, E and G) $C_{NaPSS;t=0}$ = 3.5 wt%, (B and F) $C_{NaPSS;t=0}$ = 1.0 wt%, (D and H) $C_{NaPSS;t=0}$ = 10 wt%. Reproduced with permission from ref. 141. Copyright 2016 American Chemical Society.

4.1.1.2. Golf-ball-shaped particles. Golf-ball-shaped microparticles[142–144] show dimple surface patterns or internal pore structures and therefore have larger surface areas than smooth microparticles. Therefore they improve the adhesion and prolong the distance of flight by reducing the air drag force.[145–148] Conventional fabrication methods include:[142,143,149–154] (1) seeded dispersion/emulsion polymerization and (2) emulsion stabilization using small colloidal particles. However, the former techniques cannot be applied in biological systems (toxicity) and the latter one lacks precise control of the particle internal architecture. Microfluidic methods have emerged as a versatile alternative for this type of microparticles. Kim *et al.*[155] used photocurable suspended droplets containing colloidal silica nanoparticles. The surface of these monodisperse emulsion droplets, obtained from 2 coaxial glass capillaries with different diameters,[156] was decorated with a hexagonal array of silica particles. After UV-irradiation for 1 s, raspberry-like microparticles[154,157] were obtained and transformed to golf-ball-shaped structures (Fig. 8) by etching away the silica nanoparticles on the surface of the raspberry-like microparticles using either 1 wt% NaOH or 5 wt% HF.
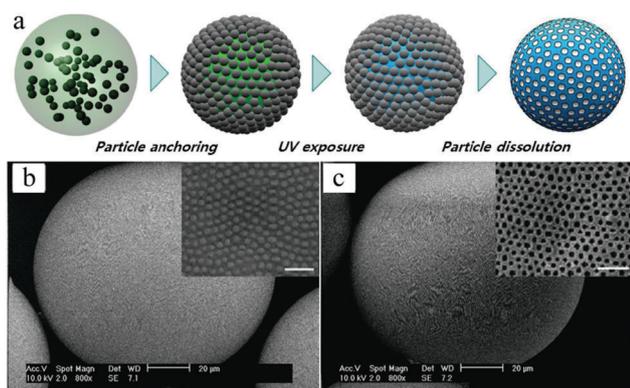

Fig. 8   (a) Illustration of the fabrication steps of golf-ball-shaped microparticles. SEM images including close-up of microparticles with arrays of 235 nm silica nanoparticles (b) before and (c) after the wet etching process. Scale bars in (b) and (c) are 20 μm, while 1 μm in close-up images. Reproduced with permission from ref. 155. Copyright 2009 IOP Publishing Ltd and Deutsche Physikalische Gesellschaft.
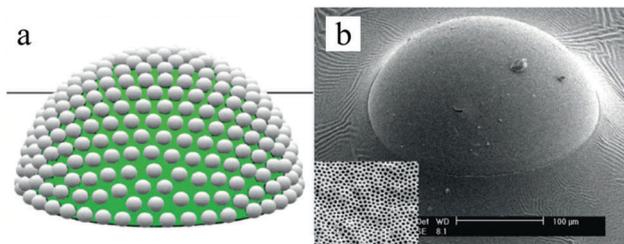

Fig. 9   (a) Illustration of patterned polymeric domes, (b) SEM image of a single polymeric dome, including magnification of the porous surface morphology. Scale bar is 100 μm. Reproduced with permission from ref. 158. Copyright 2009 Wiley-VCH.

In the same year, Kim *et al.*[158] adapted the technique for the controlled fabrication of hemispherical golf-ball-shaped structures or so-called photonic domes by using photocurable emulsion droplets as templates.[156] The patterned polymeric domes (Fig. 9) were prepared in 3 steps: (1) fabrication of ethoxylated trimethylolpropane triacrylate (ETPTA) droplets containing a high load of silica nanoparticles, (2) UV-irradiation of droplets for 10 s inducing polymerization and (3) selective removal of silica nanoparticles on the surface by a HF solution.[156,159] Kim *et al.*[160] added a post-treatment of these golf-ball-shaped microparticles by reactive ion etching with sulfur hexafluoride resulting in microparticles composed of super hydrophobic and hydrophilic surfaces.

Hwangbo *et al.*[161] proposed a novel method to obtain microparticles with both a golf-ball-shaped surface and an internal porous structure using various polymers in a one-pot method (no post-treatment), similar to the breath figure method.[148] In their fabrication process, an inert organic volatile phase change material (PCM) was employed, *e.g.* dichloromethane (DCM). Dimple patterns were created already in the first stage by fast DCM evaporation (Fig. 10a).

Along with DCM evaporation, phase separation between the polymer and PCM led to PCM droplet formation inside the oil droplets. The particle solidification process was accompanied by volume shrinkage. Eventually, surface dimples formed on the PCM surface covering the oil phase droplet, while the PCM inside the oil phase droplet contributed to form a closed porous structure. Soft stirring of the aqueous medium before surface solidification generated smaller and more even dimples. Interestingly, the SEM images (Fig. 10b–g) showed that the golf-ball-shaped microparticles exhibited a dimple surface pattern with no pores using amorphous polymers (PSf and PDLA), while the ones obtained with semi-crystalline polymers (PLLA and PCL) contain surface pores.

Based on Hwangbo *et al.*'s work, Lee *et al.*[162] could enhance the diameter of the surface dimples (thereby lowering the specific number of dimples) by increasing the PCM to PLGA ratio in the same tube-type microfluidic device (Fig. 11). A subsequent study found that because of this unique structure, active agents can be released faster from surface dimples than from interior dimples, which opened routes for drug release strategies. Compared to hollow and open porous microparticles, golf-ball-shaped ones can avoid interference from the external environment with the internal encapsulated material.
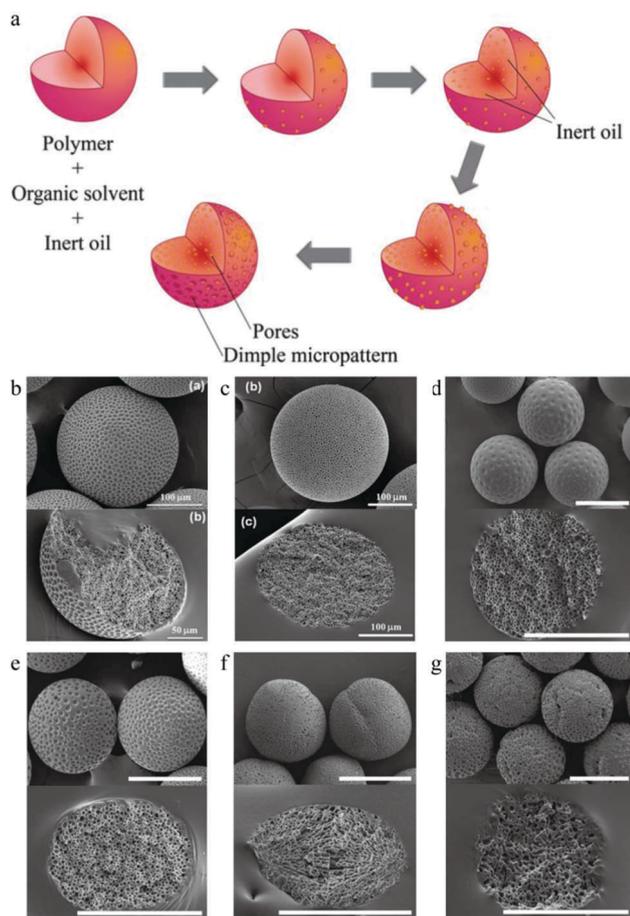
Fig. 10 (a) Illustration of golf-ball-shaped microparticle fabrication. SEM images of the surface (up) and internal structure (down) using (b) poly(D,L-lactide-co-glycolide) (PLGA), (c) poly(methyl methacrylate) (PMMA), (d) polysulfone (PSf), (e) poly(D,L-lactide) (PDLA), (f) poly(L-lactide) (PLLA) and (g) poly(ε-caprolactone) (PCL). Scale bars are 50 μm (b, down), 100 μm (b, up and c) and 200 μm (d–g). Reproduced with permission from ref. 161. Copyright 2011 The Royal Society of Chemistry.

4.1.2. "Opened" macroporous particles.

"Opened" macroporous microparticles have macropores distributed not only on their surface, but also in their interior. Besides, the internal and external pores are interconnected, which facilitates rapid mass/energy exchange between external media and the polymer matrix. Generally, the fabrication of these particles in microfluidic devices is based on 4 methods: (1) simple polymerization with or without porogens, (2) phase emulsions as templates, (3) flow reactions under specific conditions and (4) nano- or micro-particle self-assembly.[17–19,133,134,156,163–172] These macroporous particles can show a microsphere morphology or an irregular microstructure.

4.1.2.1. Macroporous spheres.

Polymeric cryogels, which are sponge-like materials with a super macroporous structure, are of interest as new chromatographic supports, cell scaffolds and drug carriers in biological and biomedical areas. In general, the matrices of the gels are prepared in the form of monoliths by polymerization under cryogenic conditions. Alternatively, the
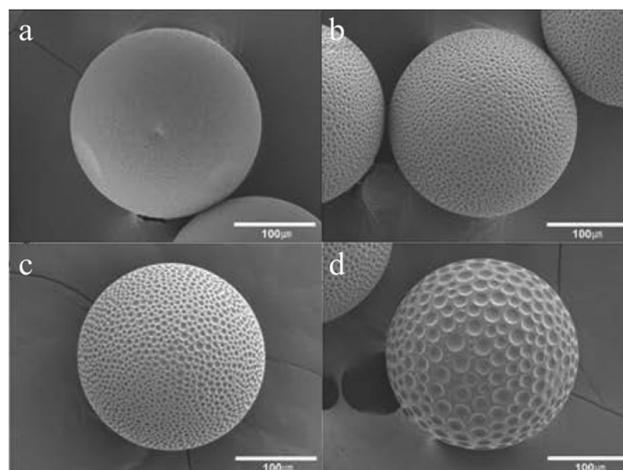

Fig. 11 SEM images of golf-ball-shaped microparticles with PLGA : PCM ratios of (a) 9 : 1, (b) 8 : 2, (c) 7 : 3 and (d) 6 : 4. Reproduced with permission from ref. 162. Copyright 2014 American Chemical Society.

cryogels can be produced in the form of suitable adsorbent microspheres. Yun et al.[168] provided a novel approach by combining the microchannel flow focusing technique with cryo-polymerization for the preparation of polyacrylamide-based gel microspheres with narrow particle size distribution (Fig. 12).

Dubinsky et al.[133] reported a semi-continuous photo-initiated microfluidic synthesis method of macroporous polymer microspheres in the size range of 10–100 μm with narrow size distribution. Monodisperse droplets were obtained with different compositions by employing different porogens: diethyl phthalate (DEP), diisobutyl phthalate (DBP), dioctyl phthalate (DOP) and diisodecyl phthalate (DDP), followed by UV-induced polymerization and washing with methanol and acetone for porogen removal (Fig. 13). The surface of the microspheres had a well-defined and interconnected porous structure, depending on the type of porogen used. The mean particle diameter increased in the order DEP < DBP < DOP < DDP, while the specific surface area decreased in the same order. Dubinsky et al.[17] added variations to this preparation method by applying not only different porogens, but also their mixtures. Fig. 14 shows the surface morphology and the internal structure of macroporous poly(GMA–EGDMA) particles using a DBP : DOP (3 : 1 v/v) mixture as a porogen. Interestingly, the interconnected morphology remained, but the surface morphology changed to porous or smooth. Additionally, they built a map (Fig. 15) demonstrating the relationship between the solubility parameter and the interfacial tension "map", which predicts the surface morphology as a function of the monomer and porogen.

Kim et al.[156] introduced a two-step method composed of photopolymerization and wet etching for the synthesis of porous photonic spheres in a co-flow capillary device (Fig. 16a). Interestingly, the pores packed on the outer layer showed well-ordered arrays, while near the core the structure became less ordered due to the high curvature. By tuning the diameters of the embedded silica particles from 145 to 152 and 190 nm, the emulsion droplets exhibited different colors from blue to green and red, opening potential application in optical research.

This journal is © The Royal Society of Chemistry 2017

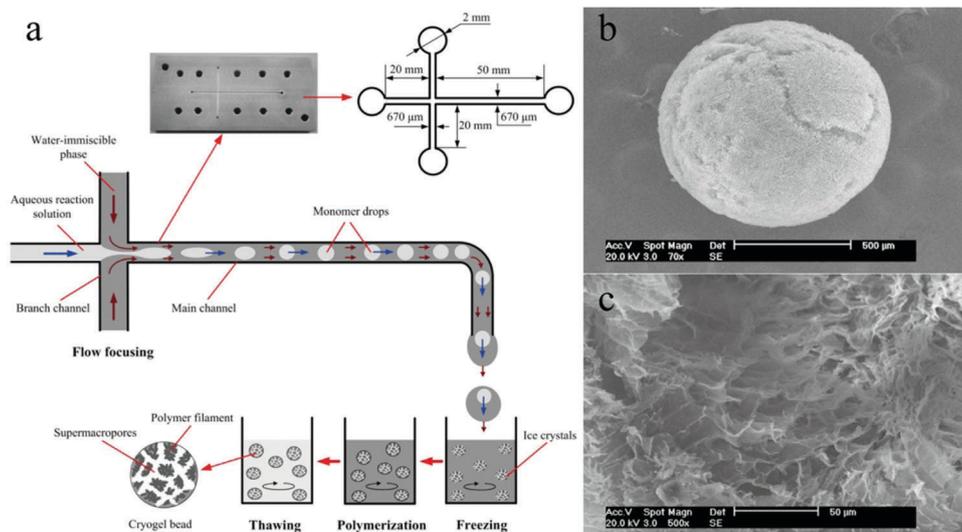Chem. Soc. Rev., 2017, 46, 855–914 | 863

Fig. 12 (a) Illustration of the cryo-polymerization process for the synthesis of macroporous microspheres. SEM images of (b) surface morphology and (c) internal structure. Scale bars are 500 μm (b) and 50 μm (c), respectively. Reproduced with permission from ref. 168. Copyright 2012 Elsevier B.V.
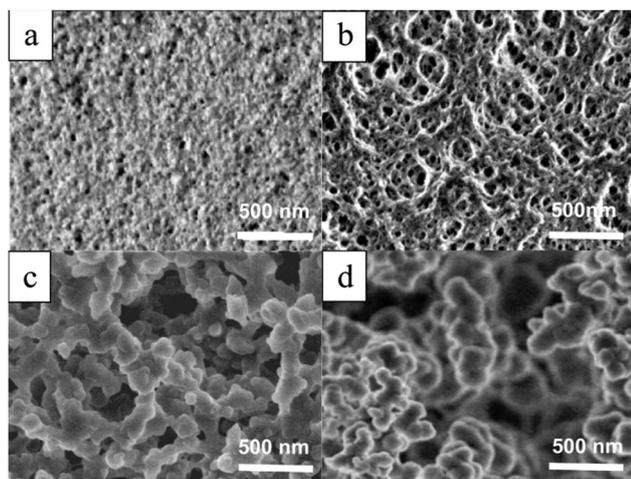

Fig. 13 SEM images of surface morphology of macroporous microspheres prepared with (a) DEP, (b) DBP, (c) DOP and (d) DDP as porogens. Scale bar is 500 nm. Reproduced with permission from ref. 133. Copyright 2008 American Chemical Society.
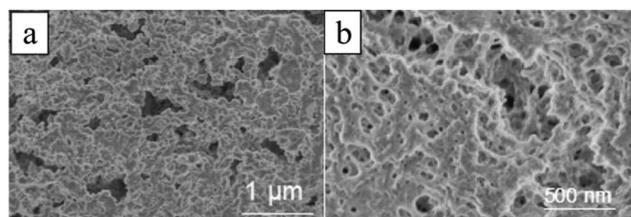

Fig. 15 Map of interfacial tension (γ) and solubility parameter (δ) of porogens using a 2.5 wt% aqueous solution as the continuous phase and different porogen solvent compositions as the dispersed phase. Reproduced with permission from ref. 17. Copyright 2009 American Chemical Society.

Fig. 14 SEM images of the (a) internal structure and (b) surface morphology of macroporous microbeads, generated with mixtures of DBP : DOP 3 : 1 (v/v). Reproduced with permission from ref. 17. Copyright 2009 American Chemical Society.

The introduction of porosity in microbeads requires porogens which are emulsified with other microbead components during the synthesis. To produce the pores effectively, porogens must be removed in a second leaching process, which requires harsh conditions. Therefore, the removal may be assisted by taking away the encapsulated active compounds also.[173,174] This limitation can be overcome by using new miscible porogens or new synthesis strategies, like those that employ permanent geometric templates or scaffolds to avoid the leaching step.[175–177] Duncanson et al.[169] introduced a self-assembling perfluorinated–dendrimer–dye complex as a novel pore forming agent to generate monodisperse macroporous microspheres (Fig. 17) in a microfluidic flow-focusing device (FFD). After removing the organic solvent, residual water and gas were released from the microspheres under vacuum conditions followed by further drying and solidification of the droplets. The porogen not only acted
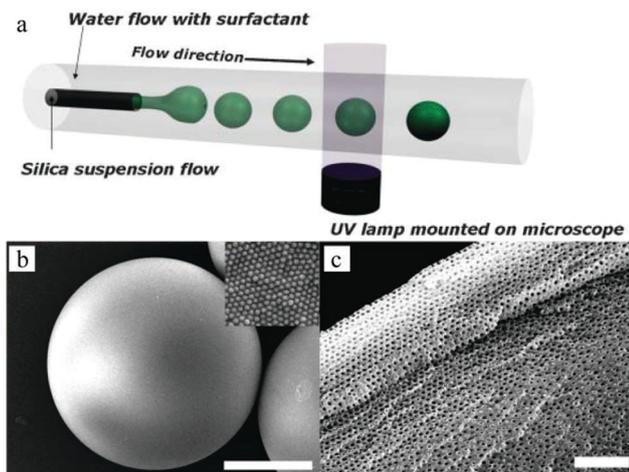
Fig. 16 (a) Illustration of uniform droplets generated in the microfluidic device. SEM images of (b) whole photonic sphere embedded with 165 nm silica particles and (c) porous surface of the sphere. Reproduced with permission from ref. 156. Copyright 2008 Wiley-VCH.

Fig. 17 SEM micrographs of macroporous microspheres made by using the (a) [G 1.5]–dye complex and (b) [G 3.5]–dye complex. Reproduced with permission from ref. 169. Copyright 2012 The Royal Society of Chemistry.
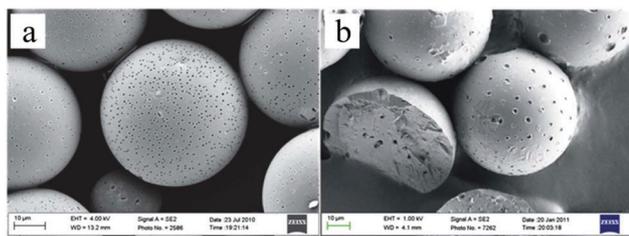
as a pore formation agent, but also played a role as a carrier for additional active materials. It encapsulated efficiently active materials avoiding their disruptive removal. These microbeads could be applied in liquid–gas mixtures.

Jiang *et al.*[178] created a new type of discrete immunebeads using microfluidic microspheres. Three interesting features are associated with their synthesis route: (1) SR454 serving as a trivinyl cross-linker increased the pore dimensions and therefore enhanced the transport and exchange of biomolecules, (2) decyl alcohol was adopted as a safer porogen rather than conventional phthalate plasticizers, without compromising the precise control of the final pore morphology and (3) the microfluidic apparatus was simple and cheap compared to conventional ones.[77,179,180] The immune active ligands were first decorated on the porous surface followed by macropore formation (Fig. 18a). The proteins (anti-IgG) were anchored on the porous surface with 2 separate processing routes, using either glutaraldehyde (GLU) or *N*-gamma-maleimido-butyryloxy-succinimide (GMBS). In the former, the GMA surface epoxides were reacted first with ethylenediamine and then consented with GLU through aldehyde–amine interaction (Fig. 18b).[181] The remaining free aldehyde group on GLU was then reacted with IgG primary amines to decorate the antibodies on the polymer surface.[182] Some interference was observed due to background fluorescence and unsaturated imine formation. In the GMBS procedure, a thiol group was first grafted onto the monolith *via* epoxide–cysteamine reaction. Subsequently, GMBS was anchored on the newly formed thiol group, by reacting with the GMBS maleimide terminus. The auto fluorescence interference was repressed in this procedure. As a result, the microspheres grafted with bioactive proteins gradually evolved to discrete immune sensor elements.
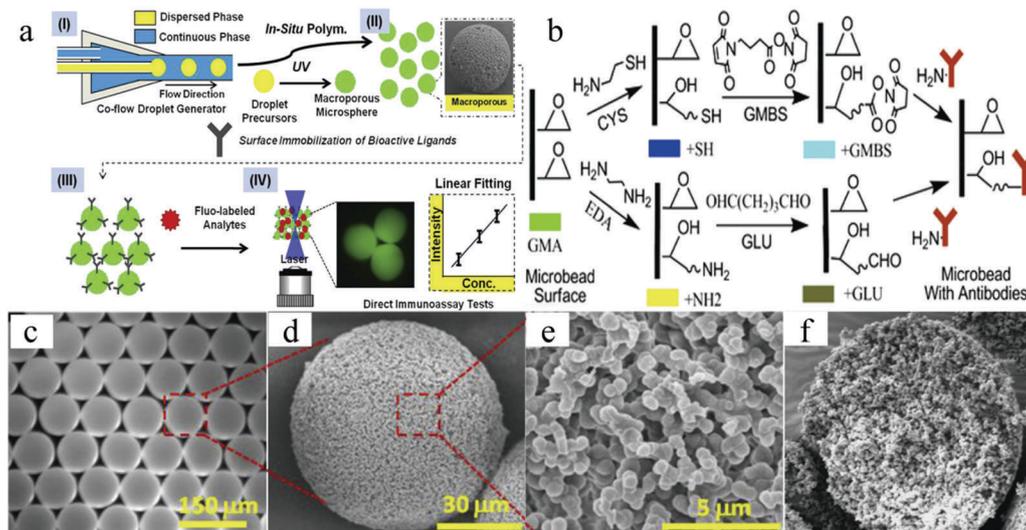

Fig. 18 Illustration of (a) macroporous microsphere fabrication and surface modification for ligand anchoring, (b) GMBS and GLU approaches for anchoring an antibody on the polymer surface and (c) optical image of the macroporous microspheres. SEM images of the (d) whole microsphere, (e) macroporous surface and (f) cleaved microspheres showing a uniform and cellular structure throughout the whole particle. Reproduced with permission from ref. 178. Copyright 2012 Elsevier Ltd.
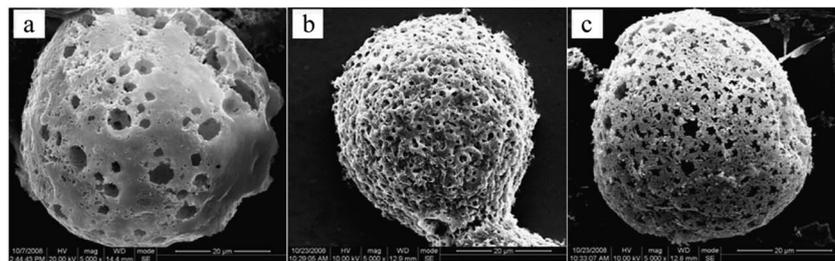
Fig. 19 SEM images of macroporous poly(HEMA–MMA) microspheres with PVP/(HEMA + MMA) wt% of (a) 3%, (b) 5% and (c) 7%. Scale bar is 20 μm. Reproduced with permission from ref. 18. Copyright 2009 Elsevier Inc.

Emulsion templating is among the most convenient and commonly used macroporous microparticle fabrication methods. By fabricating monomer-comprised single emulsions as templates in a microfluidic device, with appropriate initiators and different types of porogens, microspheres can be controllably prepared with a monodisperse and highly interconnected structure. Zhang et al.[18] proposed a novel and simple method to prepare monodisperse poly(HEMA–MMA) microbeads with macroporous structures, using oil-in-water (O/W) emulsions as templates with 2,2-dimethoxy-2-phenylacetophenone as a photo-initiator and poly(vinyl pyrrolidone) (PVP) as a porogen in a flow-focusing capillary microfluidic device.[81,183] The microbeads showed slow biodegradability, increased chemical stability due to their polymeric 3D networks (formed after free radical co-polymerization of MMA with 2-hydroxyethyl methacrylate (HEMA))[184] and high specific surface area. SEM images (Fig. 19) illustrate that upon altering the [PVP]/([HEMA] + [MMA]) mass ratio, the final morphology of microspheres varied significantly. Remarkably, the mechanical strength decreases with increasing contents of PVP.

High-internal-phase emulsion (HIPE) is another emulsion templating method,[185–189] where the volume fraction of the dispersed phase exceeds the 0.74 threshold value for monodisperse emulsions and can reach up to 0.99. PolyHIPE beads contain larger cavities within an average size range of 10–100 μm. These cavities are interconnected by a series of smaller pores that enable them to communicate with the adjacent ones. For their fabrication, first water, an initiator and a salt were mixed together for the formation of the interior phase. Then, this interior phase was mixed with the organic phase and an emulsifier to constitute a water-in-oil (W/O) HIPE. Finally, after polymerization of the continuous phase and removal of the aqueous droplets, porous particles with spherical geometry were obtained[190–194] under controlled conditions. Gokmen et al.[19,195,196] also fabricated poly(HIPE) microspheres using a microfluidic approach. Both dimension and morphology of the microspheres were precisely controlled. The obtained beads showed significantly smaller pore diameter, even down to 15 μm (Fig. 20). A post-modification was also demonstrated to modify the chemical functionality of the internal structure.

Double emulsions such as water-in-oil-in-water (W–O–W) and oil-in-water-in-oil (O–W–O) are complex colloidal systems, where dispersed droplets contain smaller droplets. They are potential devices to encapsulate active substances, e.g. cosmetics,[197] drugs,[198–200] living cells,[201] and food supplements.[202,203]
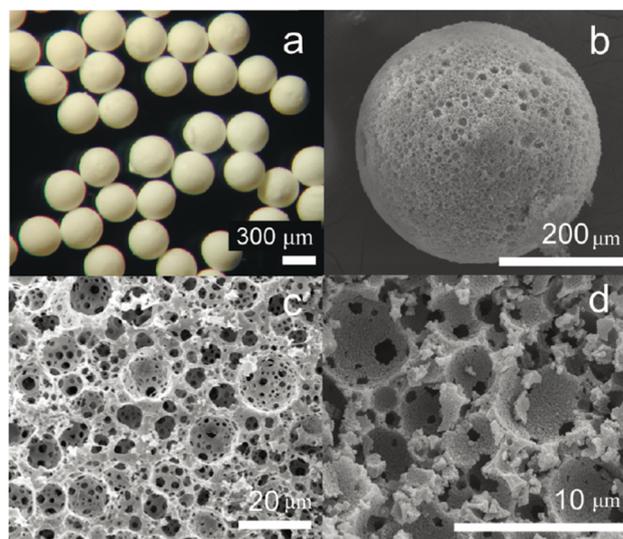
Fig. 20 (a) Optical microscopy images of porous poly(HIPE) beads. SEM images of (b) whole microspheres, (c) surface of a microsphere and (d) inner structure of the microspheres. Reproduced with permission from ref. 19. Copyright 2009 American Chemical Society.

Stable double emulsions can be fabricated in fluidic devices based on microchannels, both in PDMS devices and in capillaries. Two-step droplet break-up at the T-junction[204,205] and hydrodynamic flow focusing[79,128,206,207] were the common setups used. The double emulsions often rendered excellent characteristics, such as uniformity in terms of diameter, shape, wall thickness and the number of encapsulated droplets. Moreover, simple fluidic devices constructed from glass capillary tubes, needles and PVC tubes were also developed for this purpose.[196,208–210] Choi et al.[175] introduced a fluidic device with one extra fluid channel in the above described system (3 flow channels totally), yielding uniform double emulsions (Fig. 21a). In this W–O–W system, both the W–O emulsion obtained in the first step and the W–O–W emulsion obtained after the second step were prepared in a dripping mode, leading to more uniform dimensions than those obtained in a jetting mode.[211,212] The W–O–W emulsion droplets evolved gradually to large interconnected pores (Fig. 21b and c). This method was employed in numerous studies.[192,213–215]

Jeong et al.[170] created photo- and thermoresponsive macroporous core–shell spheres with reversible membrane permeability

866 | Chem. Soc. Rev., 2017, 46, 855–914

This journal is © The Royal Society of Chemistry 2017
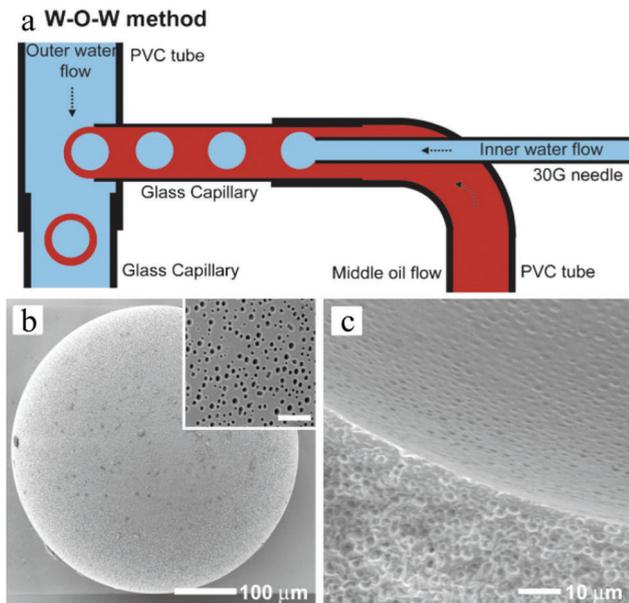
Fig. 21 (a) Illustration of the microfluidic apparatus for W–O–W emulsions. SEM images of (b) the porous surface including a close-up (scale bar is 5 µm) and (c) the cross-sections and the internal structure of PLGA microbeads. Reproduced with permission from ref. 175. Copyright 2009 Wiley-VCH.

using a simple microfluidic device (Fig. 22). Highly uniform W–O–W double emulsion droplets with an aqueous core and interconnected porous shell were generated as templates, whose outer layer is then covered with an ethyl cellulose membrane with densely packed poly(*N*-isopropylacrylamide) (pNIPAAm) nanoparticles containing gold rods, which endowed the macroporous spheres with thermoresponsivity. The size of the pores was in the range of submicrometers to several micrometers. The ethyl cellulose membrane aided in the mechanical strength and was hardly affected by light, heat and chemicals. Interestingly, the permeability of the pNIPAAm nanoparticle embedded

membrane was regulated by temperature, as a function of its phase transition behavior. When the temperature was raised beyond a certain value, the microspheres shrunk and start to allow much bigger molecules to pass through. This feature would not be achieved without the gold nanorods on the microspheres. By using near-infra-red (NIR) irradiation, the reversible membrane permeability could be remote controlled.

Next to single and double emulsion templates, a three phase emulsion was used by Wan *et al.*[134] to produce porous polyacrylamide microspheres. The emulsion consisted of gas, water and oil, applied in flow focusing or T-junction devices, FFD (Fig. 23a) and FFT (Fig. 23b), respectively. Individual gas bubbles were encapsulated by monodisperse photopolymerizable acrylamide (AAm) aqueous droplets (Fig. 23c). After UV-irradiation, these droplets gradually evolved to highly porous microspheres. The gas pressure played a major role in the droplet size in the FFT device, but it was only marginally affected in the DFF device.

The formation of macropores by reaction between reagents, *e.g.* thiol–ene and thiol–yne reactions,[216,217] has become an attractive alternative because it omits tedious templates and porogen removal procedures. Prasath *et al.*[164] presented a method to apply thiol–ene and thiol–yne reactions followed by UV-induced polymerization in a simple co-flow capillary device as a one-step preparation procedure of macroporous microspheres containing different functional groups with different morphologies (Fig. 24). Li *et al.*[218] improved this strategy by two reactions occurring successively in a single droplet: an exothermic free radical polymerization of an acrylate monomer followed by an endothermic polycondensation with a urethane oligomer, activated by the heat generated from the first reaction. As a result, an interpenetrating polymer network is obtained within the macroporous structure.

As a variation of this method, Gong *et al.*[163] prepared porous beads *via* simultaneous reactions within a single droplet in a microfluidic FFD. Monodisperse droplets, containing a H_2O_2 solution, were fabricated with several precursors: NOA 61

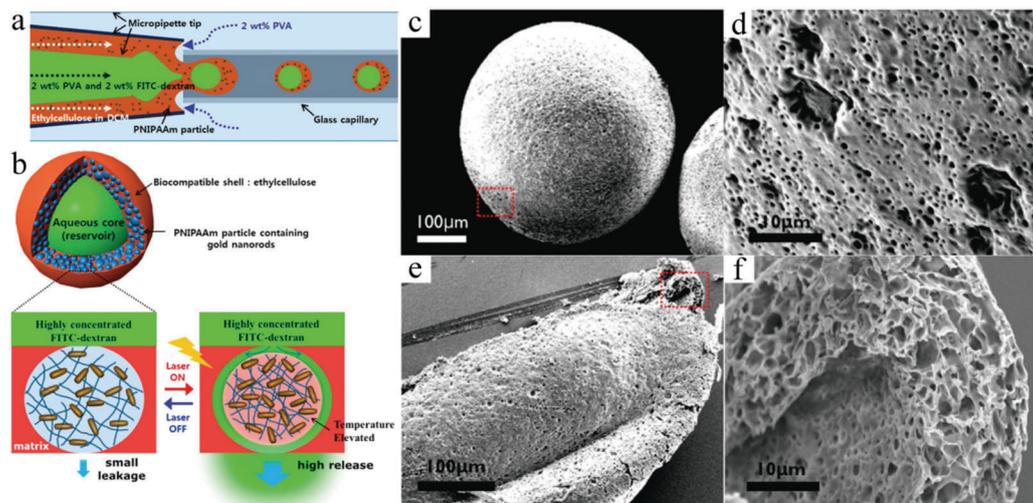**Fig. 22** Illustration of (a) the fabrication and (b) the structure of macroporous core–shell pNIPAAm microspheres with the corresponding SEM images of (c and d) porous surface and (e and f) cross-sections. Reproduced with permission from ref. 170. Copyright 2013 American Chemical Society.
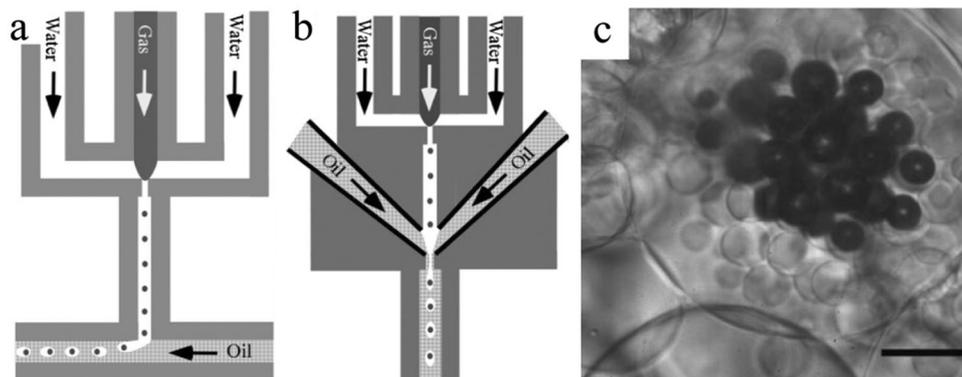
This journal is © The Royal Society of Chemistry 2017

Chem. Soc. Rev., 2017, **46**, 855–914 | **867**

Fig. 23 Illustration of the (a) DFF and (b) FFT microchannel geometry of the microfluidic apparatus and (c) optical image of microspheres from three-phase emulsions (scale bar is 50 μm). Reproduced with permission from ref. 134. Copyright 2008 Wiley-VCH.
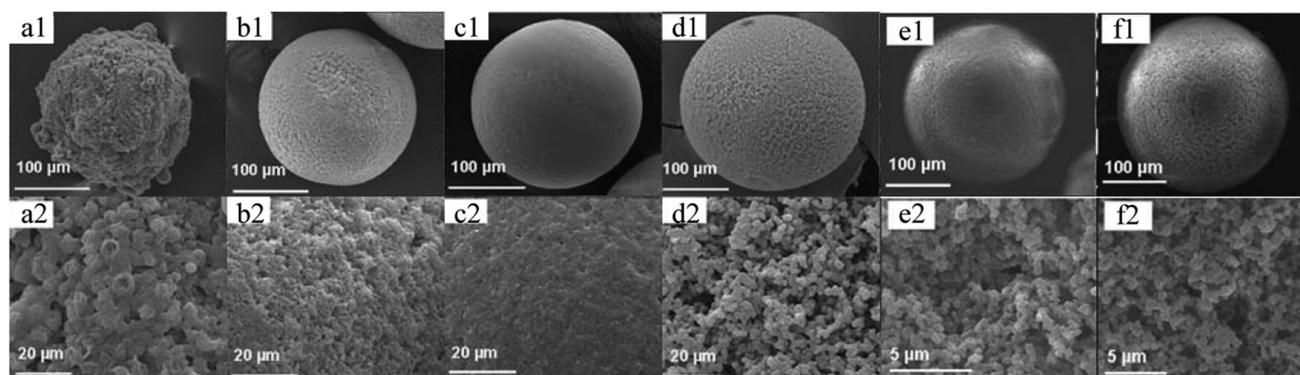

Fig. 24 SEM images of (a1–d1) whole microparticles and (a2–d2) surface morphology of macroporous microparticles generated from the "thiol–ene" formation of (a1 and a2) TT/(DAP + AA)$^{\alpha}$, (b1 and b2) TT/(DAP + AA)$^{\beta}$, (c1 and c2) TT/PTE$^{\beta}$ and (d1 and d2) (TT + MA)/TTT$^{\beta}$. SEM images of (e1 and f1) whole microparticles and (e2 and f2) relative surface morphology from the "thiol–yne" formation of (e1 and e2) TT/(OY + PA)$^{\beta}$ and (f1 and f2) TT/(OY + DPPD)$^{\beta}$. Reproduced with permission from ref. 164. Copyright 2010 The Royal Society of Chemistry.

(a mixture of trimethylolpropane diallyl ether, isophorone diisocyanate ester, trimethylolpropane tris thiol and a benzophenone photo-initiator),[219–222] EGDMA or tripropylene glycol diacrylate (TPGDA).[127,223] The droplets were further encapsulated in the outer phase (either liquid paraffin for NOA 61 or silicon oil for EGDMA and TPGDA) and exposed to UV-irradiation until the desired number of cores was generated. The UV-light and/or heat induced the polymerization of the shell and the decomposition of H$_2$O$_2$, and the precursors were solidified while oxygen and water vapor (after further heating) were released through the shell creating a porous structure (Fig. 25). These porous microspheres had a pore dimension in the range of 1–100 μm and a maximum internal void volume fraction up to 70%, similar to the HIPE microbeads.

The microfluidic technology provides a method to precisely control the fabrication of porous beads. However, microfluidic devices are often limited in channel size and therefore complications may arise when materials are difficult to solidify, *e.g.* when they are light/heat sensitive or absorb light too strongly. Photopolymerization or photo cross-linking can help the precursors to react and solidify more rapidly. Superparamagnetic porous microbeads can be subjected to an external magnetic
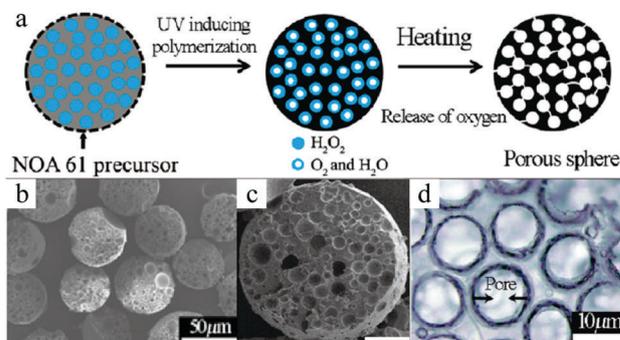
Fig. 25 (a) Illustration of the structural evolution from emulsion to macroporous microspheres. SEM images of (b and c) polyTPGDA microspheres and (d) cross-section of polyNOA microspheres. Scale bar is 50 μm (c). Reproduced with permission from ref. 163. Copyright 2009 American Chemical Society.

field to simplify the particle separation process.[224–226] Moreover, particles can be selected on the basis of size and magnetic susceptibility in miniaturized on-chip systems.[227] They are fabricated with porogens or double emulsions in microfluidic channels with good control over size and distribution.[17–19,58,133,134,163,228]

868 | *Chem. Soc. Rev.*, 2017, **46**, 855–914

This journal is © The Royal Society of Chemistry 2017
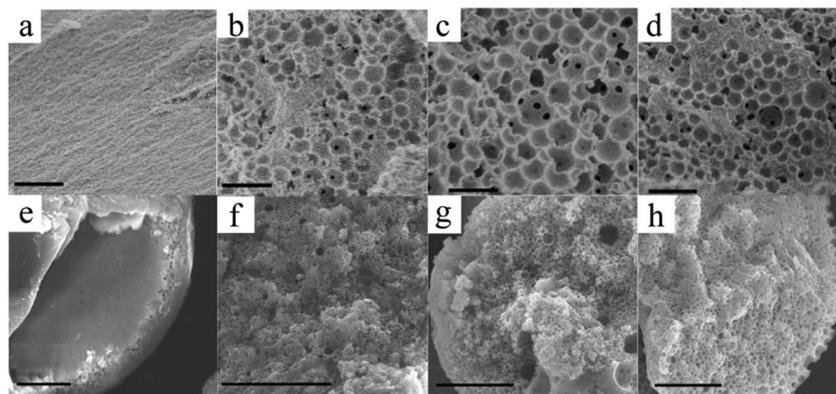
Fig. 26 SEM images of the internal structure of the macroporous microbeads collected in (a) 0, (b) 25, (c) 50 and (d) 100 mM SDS solutions, and of the microbead interior using (e) chloroform, (f) THF : toluene mixture (3 : 2), (g) toluene and (h) hexane as the dispersed phase. Scale bars are 1 μm (a–d) and 10 μm (e–h). Reproduced with permission from ref. 167. Copyright 2012 American Chemical Society.

However, superparamagnetic iron oxide nanoparticles (SPIONs) absorb light strongly, thus being more difficult to photopolymerize. Paquet et al.[167] addressed this limitation by preparing superparamagnetic microbeads based on the assembly of materials rather than any other chemical transformation such as polymerization or cross-linking, so making it suitable for fabrication with materials which are sensitive to light or heat. Different microbead morphologies resulted from alterations in the assembly processes, depending on the rate of solvent depletion from the droplet, the absorption of sodium dodecyl sulfate (SDS) at the droplet interface and the solubility of the SPIONs in the droplet phase. By adjusting the SDS concentration (Fig. 26a–d) and the polarity of the disperse phase (Fig. 26e–h), the porosity gradually evolved from non-porous to a dense and opened cellular structure. Wacker et al.[166] combined evaporation-induced solidification and silica nanoparticle self-assembly to fabricate porous microspheres. Upon changing the nanoparticles' dimension from 50 to 500 nm, the porous microspheres present different surface morphologies (Fig. 27). Their hypothesis states that if the pores were too small, evaporation of water to vapor affected the final morphology resulting in wrinkled surfaces. In contrast, when the pores were wide enough, the water vapor passed through the surface without any obstacle.

4.1.2.2. Macroporous irregular microstructure. Non-spherical particles are rather difficult to fabricate in microfluidic devices due to their high droplet surface tension and their microchannel geometry. Therefore, stabilizers are added to reduce the surface tension, combined with a meticulously designed confined space which determines the final particle shape. Both spherical and non-spherical shapes were obtained by Gokmen et al.[19] The non-spherical shape of poly(HIPE) particles was rather difficult to reproduce. This was dramatically improved by applying a different HIPE formulation,[229] resulting in the reproducible fabrication of porous rods (Fig. 28). For this, (PEO–PPO–PEO) 4000 was used as a surfactant instead of (PEO–PPO–PEO) 2800. The poly(HIPE) porous rods had a diameter of around 0.2 mm, which was considerably smaller than the 0.8 mm inner diameter of the continuous channel, suggesting that the viscosity of
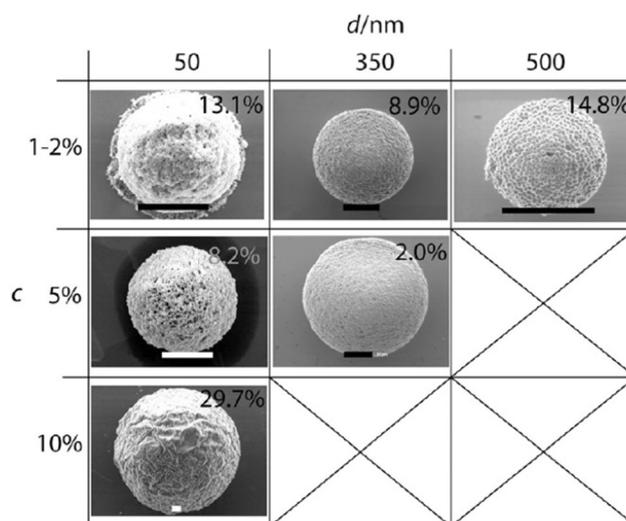
Fig. 27 SEM images of porous spheres assembled by silica nanoparticles with increasing diameter (*d*/nm) and colloid weight concentrations (c). Scale bars are 10 μm. Reproduced with permission from ref. 166. Copyright 2011 American Chemical Society.

the dispersed phase regulated the final shape rather than the microchannel geometry.

Wacker et al.[166] also obtained rod-like micro-objects, deformed from porous spheres (Fig. 29), in this case by evaporation-induced solidification and silica particle self-assembly. Increasing the oscillation time resulted in more elongated shapes and a too high oscillation frequency led to smaller clusters rather than porous rod-like structures.

Important in view of possible applications, the morphology of microgels directly affected the response rate to external stimuli. For instance, conventional poly(N-isopropylacrylamide) PNIPAAm microgels usually showed a homogeneous but disconnected internal structure, which slowed down the response rate.[230,231] Several attempts were made to improve the response rate of microgels, such as constructing a more heterogeneous internal structure,[231–235] grafting functional groups onto the microgels[236,237] or employing different porogens to improve the

This journal is © The Royal Society of Chemistry 2017

Chem. Soc. Rev., 2017, 46, 855–914 | 869
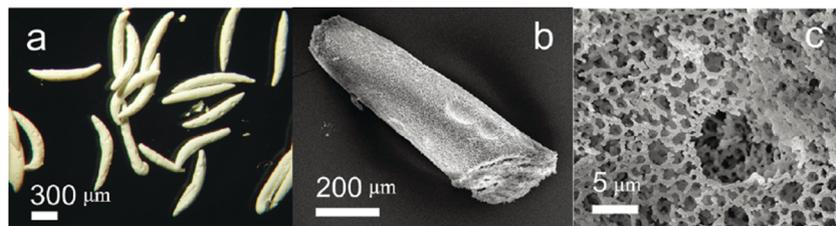
Fig. 28 (a) Optical microscopy of poly(HIPE) rods. SEM images of (b) partial rod and (c) porous surface of a rod. Reproduced with permission from ref. 19. Copyright 2009 American Chemical Society.
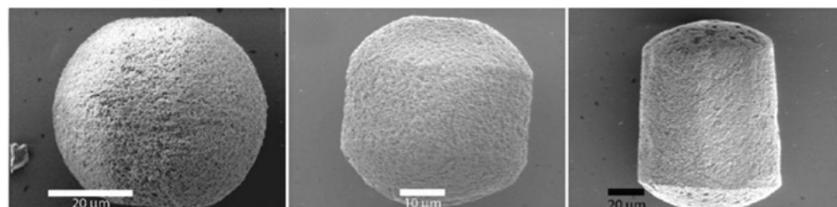
Fig. 29 SEM images of porous rod-like particles. Reproduced with permission from ref. 166. Copyright 2011 American Chemical Society.

porosity,[238–240] albeit with only moderate success. But, Chu and co-workers[183] generated monodisperse pNIPAAm microgels with spherical voids *via* embedding solid polystyrene micro-beads inside and then dissolving them with xylene, giving significantly improved response rates. Huang and his team[241] also successfully fabricated pNIPAAm microgels with a good porous structure and response rate, using polyethylene glycols as porogens. Yue *et al.*[242] improved their response rate as well, but by introducing nanogels into the microgels. Still, these fabrication methods are tedious.

pNIPAAm microcapsules can shrink upon exposure to external stimuli like heating and to certain chemicals, which finally ruptures the hydrogel surface membrane, while the oil cores

inside the microcapsules squeeze out.[243–246] Based on this, Mou *et al.*[171] fabricated environmental stimuli-responsive microgels with a highly interconnected open cellular structure by combining homogeneous emulsification and polymerization by UV-irradiation (Fig. 30). The initial homogeneous O/W emulsions served as the inner phase and soybean oil with 5% w/v PGPR as the outer phase, which were successively injected into a co-flow capillary device to obtain monodisperse (O/W)/O emulsions. Upon exposure to UV-irradiation in an ice-water bath, followed by addition of isopropanol or heating, pNIPAAm microgels with open internal structures were obtained through volume shrinkage of the microgels. They compared them with microgels obtained under identical conditions but with conventional emulsions,
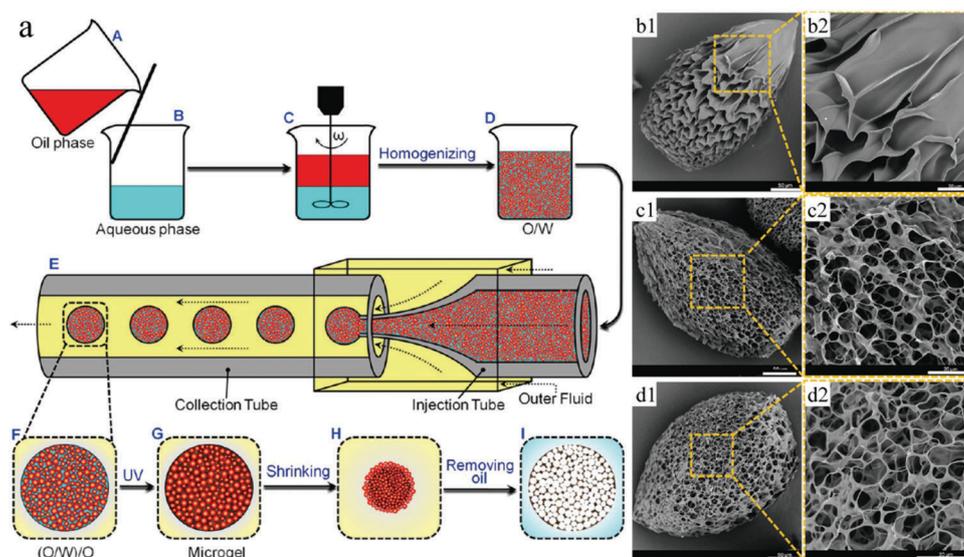
Fig. 30 (a) Illustration of porous pNIPAAM microgel formation. SEM images of pNIPAAm microgels obtained with (b1 and b2) W/O emulsions and (c and d) (O/W)/O emulsions, with molar ratios of MBAAm to NIPAM of (c1 and c2) 2% and (d1 and d2) 4%. Scale bars are 50 μm (b1, c1 and d1) and 20 μm (b2, c2 and d2). Reproduced with permission from ref. 171. Copyright 2014 American Chemical Society.

where the aqueous phase replaced the O/W emulsion. The (O/W)/O directed microgels exhibited a much higher response to environmental stimuli, such as temperature, pH, *etc.*[247–249] These results make them attractive for application in sensors, separations and actuators.[250,251]

Thin membranes can be fabricated in a microfluidic system, by cherry-picking the immiscible solutions and precisely tuning the viscosity to attain laminar flows, followed by polymerization at the liquid–liquid interface. However to date, thin membranes formed using conventional approaches have very small pore size and sometimes even lack pores, which limits their use in biological applications such as cell migration and molecule detection. Based on the study of surface tension and laminar flow behavior,[252–254] an *in situ* fabrication method was reported by Kim and Beebe,[255] relying on the interfacial reaction of a two-phase system to produce a porous nylon membrane with pore dimensions 0.1–1 μm (Fig. 31c–e). This approach made it possible to generate very thin porous membranes, firmly fixed inside the microchannel without any other bonding process. As shown in Fig. 31a, 2 partially separated microchannels existed in the fluidic apparatus.[252–254] After washing one microchannel with hexadecane and the other one with a mixture of hexadecane and octadecyl trichlorosilane, the 2 microchannels turn hydrophilic and hydrophobic, respectively. Then an aqueous solution and organic solution, respectively, were introduced into the microchannels. 1,6-Diaminohexane in water and adipoyl chloride in toluene reacted at the interface resulting in a membrane. After 15 min, the aqueous and organic solutions are replaced with MeOH and toluene, respectively, followed by washing and drying. Most of the PEG (poly(ethylene glycol) was removed with the aqueous phase as it is highly soluble in water.

Fig. 31b shows that different morphologies existed on both sides (asymmetric membrane). The organic side showed a ridge-and-valley structure (2–5 μm), while the aqueous side had a smooth skin surface (about 0.5 μm). Thus, the polymer transport occurred from the aqueous solution side to the organic solution side. This technique was also employed for the formation of chitosan and polycarbonate porous membranes.[256,257]

Materials can also be decorated with a 3D porous "coat", *via* photo-induced radical polymerization in a microfluidic device. Wang *et al.*[172] fabricated a sensitive surface-enhanced Raman scattering (SERS) optrode from GMA, ETPTA and DMPA, densely decorated with silver nanoparticles, covering the tip of an optical fiber (Fig. 32). The porous layer thickness and the pore size increased with irradiation time, ranging from 4 to 149 μm and from 0.4 to 1.0 μm for 1 and 4 min polymerization time, respectively.

More recently, Liu *et al.*[258] unprecedentedly reported a direct and versatile approach that combines a modified electrospinning setup based on a microfluidic nozzle with nonsolvent-induced phase separation to fabricate ultrafine fibers with interconnected macropores (Fig. 33). It exhibited higher specific surface area (48.66 ± 8.30 m^2 g^{-1}), larger pore size (116.73 nm) and pore volume (0.169 ± 0.007 cm^3 g^{-1}) in comparison to conventional electrospun porous fibers. In brief, two immiscible solvents, a polymer solution (20% polystyrene solutions with different THF/DMF ratios) and a mixing solvent (cyclohexane) were, respectively, pumped into the channel and well mixed before simultaneous electrospinning processes under selected operating conditions according to their previous studies.[259,260] More importantly, various immiscible solvents/solutions can be electrospun by *in situ* mixing without solute precipitation. The oil adsorption
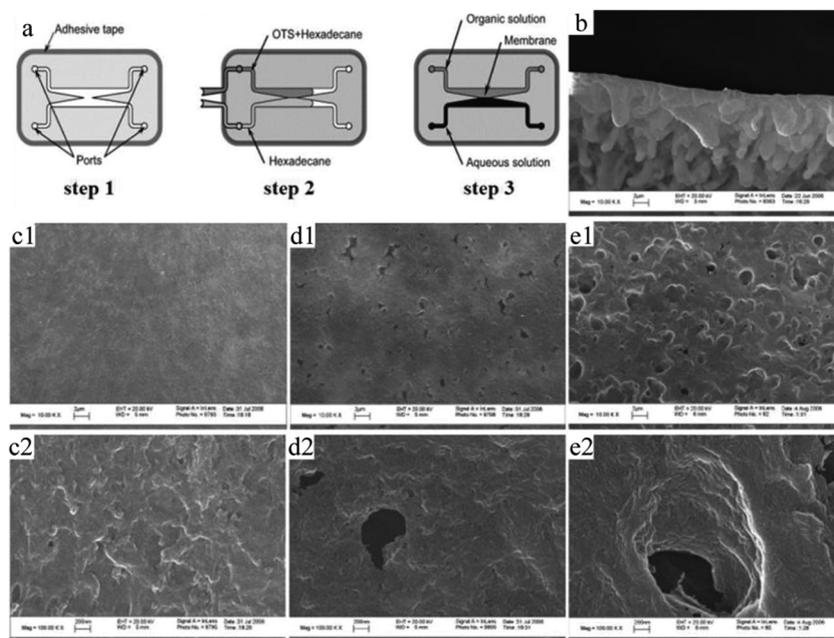
Fig. 31 (a) Illustration of interfacial membrane fabrication and SEM images of (b) a porous membrane formed by interfacial polymerization (angled view) and membranes obtained with (c1 and c2) 0, (d1 and d2) 10 and (e1 and e2) 20 mg PEG in a 60% 1,6-diaminohexane aqueous solution. The magnifications are 10 000 (b, c1, d1 and e1) and 100 000 (c2, d2 and e2). Reproduced with permission from ref. 255. Copyright 2008 Wiley Periodicals, Inc.

This journal is © The Royal Society of Chemistry 2017

Chem. Soc. Rev., 2017, **46**, 855–914 | 871
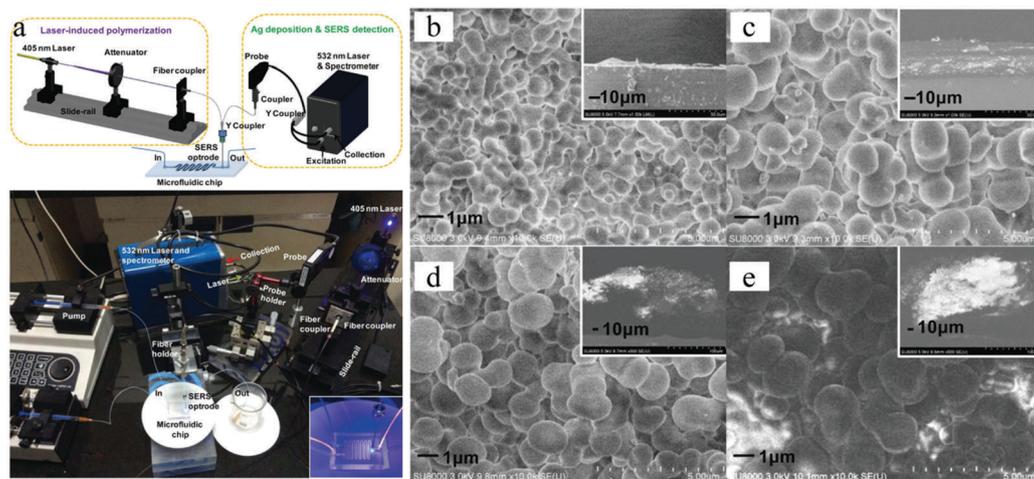
Fig. 32 (a) SERS optrode-integrated microfluidic chip. SEM images of porous polymers covering the tip of optical fibers, prepared with UV-irradiation time (b) 1, (c) 2, (d) 3 and (e) 4 min. The insets are side views. Reproduced with permission from ref. 172. Copyright 2012 American Chemical Society.
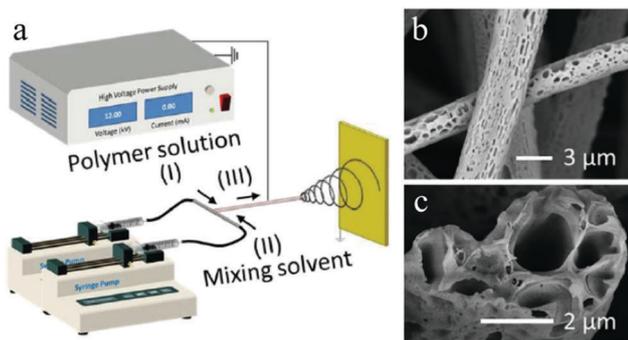
Fig. 33 (a) Schematic illustration of an *in situ* mixing electrospinning process for macroporous fiber fabrication. SEM images of the (b) surface and (c) cross section of macroporous fibers. Reproduced with permission from ref. 258. Copyright 2016 American Chemical Society.

results of macroporous fibers will be attractive to the investigation on and generation of heterogeneous fibers by *in situ* mixing electrospinning for potential applications.

4.2. Ordered macroporous particles

4.2.1. 3D scaffolds. For the engineering of functional tissues to improve biological functions or even replace damaged body parts, porous scaffolds provide a 3D template for the initial cell attachment. The porous architecture of the scaffold can be vital to the tissue morphology, as it depends on metabolic transport between cells. The mechanical properties of the scaffold material are also important. Conventional approaches to fabricate 3D scaffolds include freeze drying, phase separation, gas faming, solvent casting and particulate leaching,[261–265] but may produce disinterconnected irregular pores. Well-ordered and highly uniform structures are preferable.[266] To date, new fabrication techniques such as photolithographic patterning and layering, direct writing, and two-photon stereo lithography have been applied to create high quality 3D ordered scaffolds, each at the expense of costly resources and time.[267–270] The scaffolds should permit precise control of the pore dimension and interconnects

between them.[192,271–273] Microfluidics-based fabrication has some important advantages, *e.g.* biocompatibility, no extra template removal step, as well as finely-controlled pore size and connectivity with acceptable reproducibility, which conventional porous scaffolds generated by replicating from colloidal crystal cannot address.[274]

Chung *et al.*[275] created porous scaffolds for tissue engineering *via* adjusting the flow rate of an alginate solution and the gas pressure to reach steady state monodisperse alginate droplets, which encapsulated nitrogen gas bubbles in a continuous mode generated in a microfluidic FFD. At a low liquid flow rate and high gas pressure, the microbubbles were less stable and more polydisperse. The microbubbles were closely packed in a container with a concentrated $CaCl_2$ solution, where it gelated by vacuum degassing. The alginate scaffold exhibited a periodic interconnected porous structure (Fig. 34). Furthermore, the pore size could be adapted by varying the fluid velocity, gas pressure as well as the viscosity of the solutions. The pores were well-ordered near the surface, whereas deep inside the scaffold, the porous structure became less ordered and the size distribution of the pores became broader but still superior to scaffolds prepared by conventional methods. The feasibility of the microfluidic-generated scaffolds was further explored.[28]

More recently, Wang *et al.*[276] designed a novel microfluidic FFD device for the formation of highly organized honeycomb-like scaffolds. In their setup (Fig. 35a), the liquid phase and gas phase were introduced in the upper and lower inlets in the opposite direction. Gas-in-liquid microbubbles were generated at the liquid–gas interface. The scaffold showed a hexagonal close-packed porous texture, which facilitated cell attachment and physiology.[275,277,278]

In the FFD setup of van der Net *t al.*,[279] 2 different solutions A and B were pumped separately at identical flow rates in a parallel mode to create the continuous phase in the micro-channels (Fig. 36a).

The gas phase is sheared by the continuous phase and deformed to form monodisperse microbubbles. The polymerization did

872 | *Chem. Soc. Rev.*, 2017, **46**, 855–914

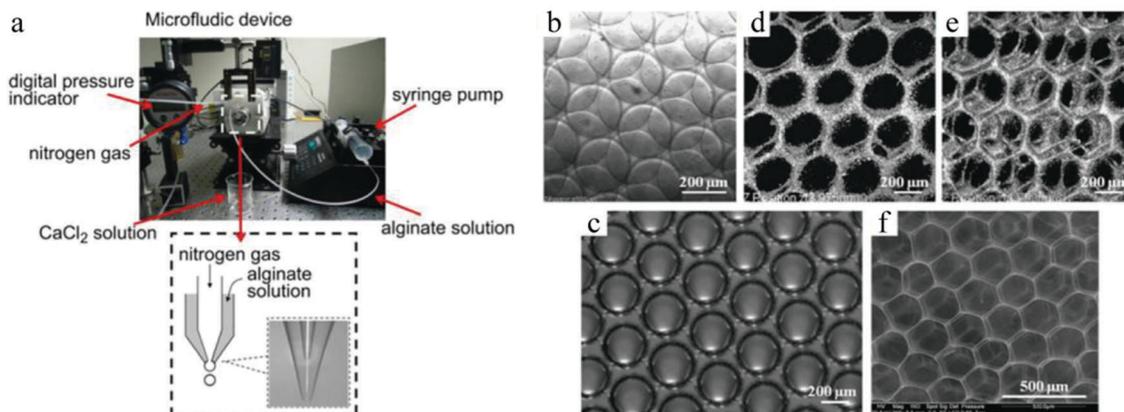This journal is © The Royal Society of Chemistry 2017

Fig. 34   (a) Co-flow microfluidic device for alginate microbubble generation, (b) monodisperse microbubbles, (c) honeycomb structure after gelation, (d and e) confocal microscope images of 3D ordered scaffold after vacuum degassing and (f) SEM image of a sponge-type alginate scaffold. Reproduced with permission from ref. 28. Copyright 2011 Elsevier Ltd.
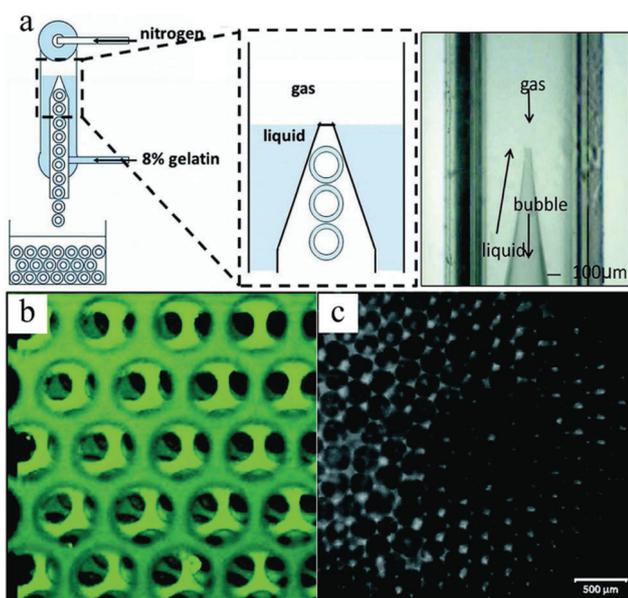
Fig. 35   (a) Counter-flow microfluidic FFC device, (b) confocal microscopy showing the layer assembly of microbubbles and (c) highly organized structure. Reproduced with permission from ref. 276. Copyright 2009 Wiley Periodicals, Inc.

not start until solutions A and B met. Although the obtained hexagonal structures in the foam (Fig. 36b) were compactly arranged, their packing directions vary. One is the (100) direction of the face-centered-cubic (fcc) packing (square arrangement of bubbles at the surface, Fig. 36c), whereas the other one is the (111) direction of fcc packing (triangle arrangement of bubbles at the surface, Fig. 36d). After polymerization, the hexagonally structured foam could be dried and re-swollen reversibly. However, incomplete polymerization was observed in some cases, as some bubbles maintain the initial spherical morphology.

Colosi et al.[280] also obtained ordered and interconnected porous 3D scaffolds using a FFD microfluidic foaming technique, based on the work of Chung et al.[275] But, here the alginate solution and nitrogen gas were replaced by an aqueous

poly(vinyl alcohol) (PVA) solution and argon gas. Immediately after generation, the monodisperse microbubbles were cross-linked with glutaraldehyde (GLU) and freeze-dried by liquid nitrogen to obtain an irreversible scaffold structure. These were compared to the ones formed by a traditional gas foaming technique. The scaffolds generated by the microfluidic foaming technique presented a superior porous structure compared to the ones made by traditional gas foaming, based on the pore size and wall thickness distribution and high-resolution computed micro-tomography (μCT) and SEM images (Fig. 37). However, the microfluidic scaffolds showed rather scarce pore interconnectivity, moderated pore volume and a limited production rate.

3D scaffolds can also be prepared from HIPE monomers. However, polyHIPE scaffolds fabricated by conventional methods show rather poor reproducibility with uneven small pores, which may not satisfy the demand of tissue engineering. On the basis of Gokmen's study,[19] Costantini and co-workers[29] successfully prepared polyHIPE scaffolds from dextran-methacrylate (DEX-MA) using a microfluidic technique (Fig. 38a).[281,282] In the first step, two immiscible phases added with DEX-MA or cyclohexane were introduced into a microfluidic FF chip to generate homogeneous O/W emulsions. In the second step, the O/W emulsions were cross-linked under UV-light (λ 365 nm) and then cured in an oven at 50 °C. In the third step, the product was placed in an organic polar solvent to extract the inner oil phase and create the macroporous structure. After washing with water and freeze-drying, the polyHIPEs presented a more interconnected and ordered architecture, compared to conventional HIPE templated scaffolds. By adjusting the flow rates of the 2 phases, distinct morphologies were obtained. The pore size of the scaffold increased upon using microchannels with larger dimensions (Fig. 38c–e). Three different lattice structures were present, including closed hexagonal packing together with [100] and [111] fcc packing (Fig. 38f–h). The concentration of the surfactant seemed to be vital to the final cellular structure. With higher surfactant concentrations, the closed porous structure evolved to a more open and interconnected one (Fig. 38i–k). However, the low production rate of

This journal is © The Royal Society of Chemistry 2017

Chem. Soc. Rev., 2017, 46, 855–914 | 873
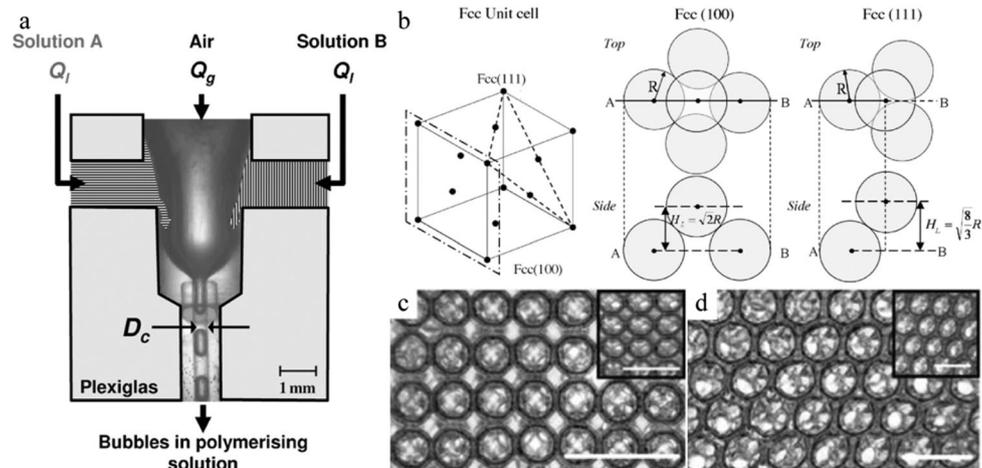
Fig. 36 (a) Parallel microfluidic FFD device and (b) unit cell of the fcc structure. SEM images of 3 ordered foam layers of the (c) (100) direction and (d) (111) direction of fcc packing in the swollen state. Scale bar is 1 mm. The inset images are taken with the foam in the dried state (scale bar is 500 μm). Reproduced with permission from ref. 279. Copyright 2009 Elsevier B.V.
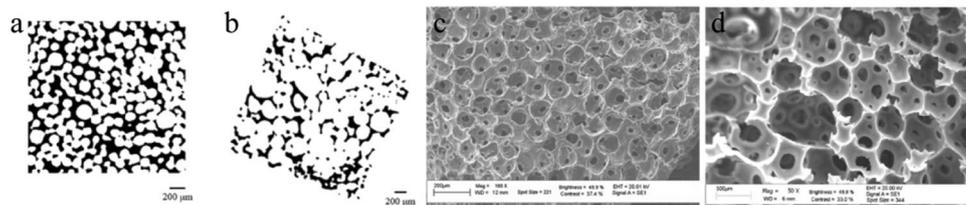
Fig. 37 μCT images of PVA scaffolds generated by (a) microfluidic foam and (b) traditional gas foam. SEM images of (c) microfluidic foam and (d) traditional gas foam. Reproduced with permission from ref. 280. Copyright 2012 American Chemical Society.
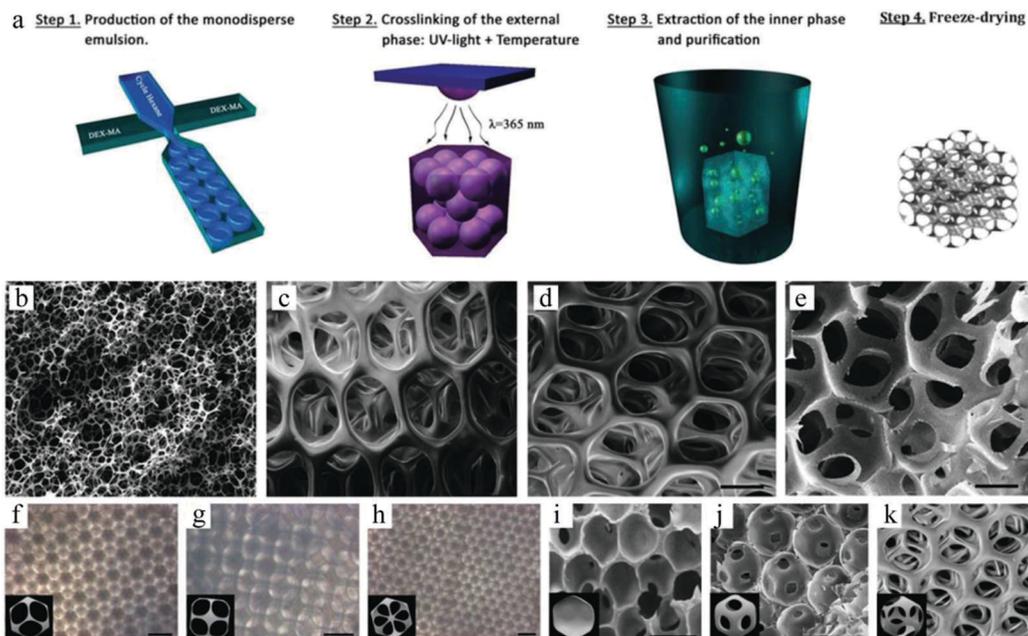
Fig. 38 (a) Illustration of polyHIPE scaffold fabrication. SEM images of (b) conventional HIPE scaffolds and microfluidic HIPE scaffolds within (c) 1-fold, (d) 2-fold and (e) 5-fold volume of microfluidic FFD. Optical micrographs of microfluidic polyHIPEs with (f) hexagonal close packed, (g) fcc [100] and (h) fcc [111] crystal structures. SEM images of microfluidic HIPE scaffolds with (i) 1, (j) 7 and (k) 25% w/v Pluronic F68. Reproduced with permission from ref. 29. Copyright 2014 The Royal Society of Chemistry.

874 | Chem. Soc. Rev., 2017, 46, 855–914

This journal is © The Royal Society of Chemistry 2017
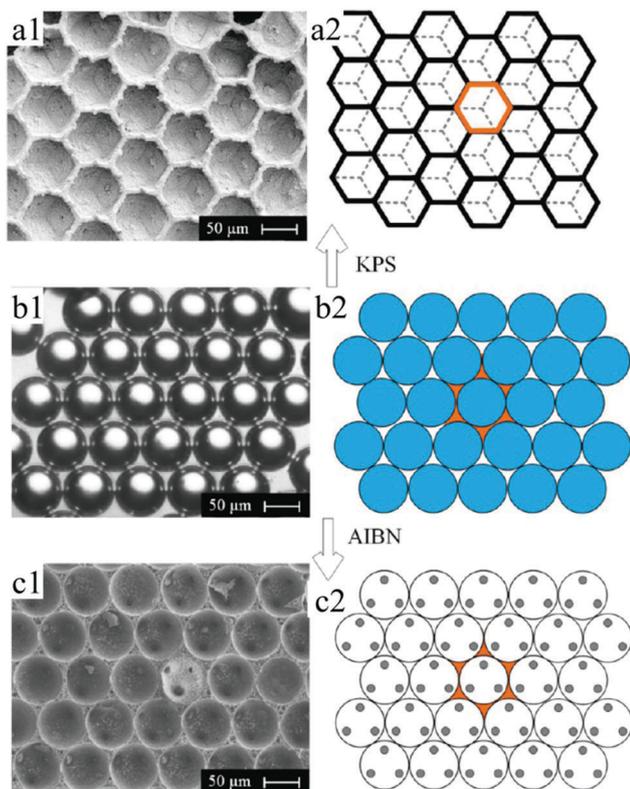
Fig. 39 (left) SEM images and (right) schemes of (a) highly ordered closed-cell polyhedral foam, (b) monodispersed emulsion templates in a continuous monomer matrix in a highly ordered level, and (c) open-cell spherical foam. Reproduced with permission from ref. 285. Copyright 2016 American Chemical Society.

the emulsions was still a limiting factor. To address this, parallelizing chips and junctions on a single chip were introduced.[86,283,284]

Similar to 3D scaffolds, polymer foams are of particular interest for packing and insulation materials because of their low transport and thermal energy consumption. In 2016, Quell et al.[285] used surfactant-stabilized HIPEs to fabricate two different kinds of highly ordered porous polymer foams, that is, closed-cell polyhedral foams (Fig. 39a) and open-cell spherical foams (Fig. 39c). For closed-cell polyhedral foams, monomers containing 1.28 mol% potassium persulfate (KPS) served as a dispersed phase. While for open-cell spherical foams, azobis-(isobutyronitrile) (AIBN) replaced KPS with the same concentration and was added into the monomers. A mixture solution of styrene and divinylbenzene containing 10 wt% of the surfactant Hypermer 2296 was used as a continuous phase. Monodispersed emulsion templates were fabricated in the microfluidic chip, and then closely subsided in a continuous monomer matrix at a highly ordered level. Subsequently, emulsion templates were polymerized in an oil bath at 70 °C for 48 h. Eventually, the as-prepared polymer foams were purified by Soxhlet extraction with excess ethanol for 12 h before drying at room temperature. More importantly, they attributed different porous structures to the locus where the polymerization started. In the case of closed-cell polyhedral foams, initiation starts within the continuous monomer matrix and neighboring droplets are isolated

by thin films. Otherwise, interconnected open-cell spherical foams were obtained.

4.2.2. Inverse-opals. Most of the research focused on the development of inverse-opaline photonic films rather than inverse-opal photonic beads.[286,287] But, Zhao et al.[288,289] fabricated colloidal photonic crystal spheres with an inverse-opal structure serving as suspended carriers in a microfluidic device. Polystyrene spheres (15 wt%, diameter 200–315 nm) were mixed with silica particles (20 wt%, diameter ±5 nm) in an aqueous solution in a volume ratio of 9 : 1, creating a binary colloidal system. The aqueous suspension was sheared to homogeneous droplets by the continuous silicon oil phase in the microfluidic device.[290] The droplets were collected in a container filled with silicon oil. The water was removed from the droplets by evaporation, which produced self-assembled polystyrene spheres with well ordered lattices, while the silica particles filled the void spaces between the spheres. After washing and calcination, the polystyrene spheres were removed resulting in the formation of uniform inverse-opal beads (Fig. 40).

Hexagonal close packed macropores were observed on the surface and in the interconnected internal structure. To obtain this morphology the volume fraction of polystyrene spheres to silica particles was important. More in particular, a volume ratio below 8 or above 10 gave a more disordered crystal structure and reduced the mechanical strength. A ratio of 9 led to greater surface area and more interaction sites, providing easier access for analyses to their recognition site. The inverse-opal photonic beads prepared by Zhao et al.[291,292] were utilized for the label-free detection of biomolecules. This was demonstrated without applying time-consuming immune assay methods.

Zhao et al.[293] also used silica colloidal crystal beads (SCCBs)[290] as sacrificial templates and prepared macroporous hydrogel photonic spheres with a well-ordered inverse-opal structure. First, the SCCBs were fabricated in a home-made microfluidic device[290] and then calcined to 800 °C for 3 h. The pre-gel solution (39% PEG, 1% initiator, 2% acrylic acid and 58% water) was filtered into the voids by capillary force. To ensure full void-filling, the SCCBs were pre-treated with piranha solution (30% H_2O_2 and 70% H_2SO_4) for 6 h, followed by washing and drying in nitrogen. The spheres got their opal architecture by polymerizing the pre-gel solution under UV-irradiation. After dissolving the template SCCBs in HF (1–2%), macroporous hydrogel photonic spheres were obtained. By increasing the PEG concentration, the mechanical strength was improved at the cost of structure order and a stable reflection peak position due to swelling. Fig. 41 shows the hexagonal close-packed SCCB surface and the well-ordered open porous and interconnected texture, before and after etching the templates. Conventional photonic band gap (PGB) crystals, which act selectively on photons like semiconductors do with electrons in electronic devices, can have opaline lattices which results in cooperative light scattering,[294] often resulting in a very limited PBG and only a few narrow stop bands. Compared with conventional PGB crystals, macroporous hydrogel photonic spheres show angle-independent specific color with wider stop band gaps and are promising for advanced optical applications, such as reflection-based displays, barcodes and label-free sensors.

This journal is © The Royal Society of Chemistry 2017

Chem. Soc. Rev., 2017, 46, 855–914 | 875

Fig. 40 (a) Illustration of the generation of inverse-opal spheres. Reproduced with permission from ref. 288. Copyright 2014 American Chemical Society. SEM images of (b) whole inverse-opal 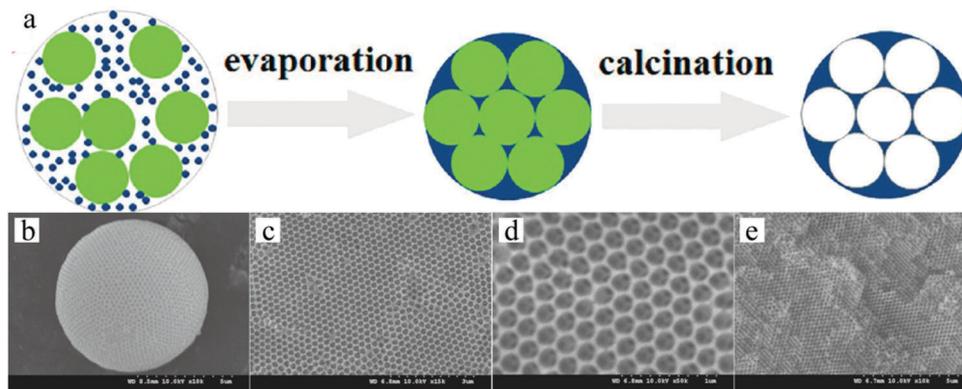spheres, (c) ordered porous surface and (d and e) ordered and interconnected internal cellular structure. Reproduced with permission from ref. 289. Copyright 2009 Wiley-VCH.
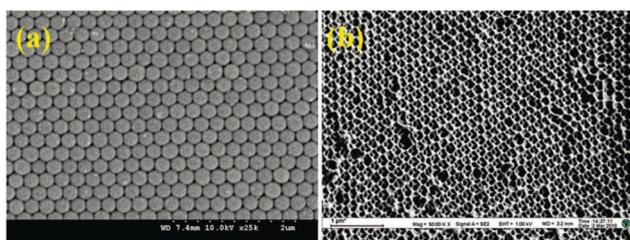
Fig. 41 SEM images of a highly ordered surface of (a) template SCCB and (b) PEG inverse-opaline photonic sphere. Reproduced with permission from ref. 293. Copyright 2010 American Chemical Society.
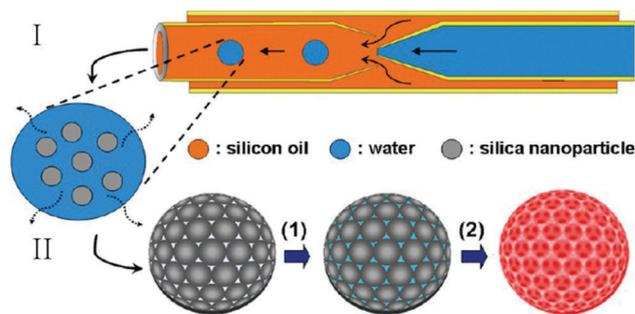
Fig. 42 Inverse-opal HPCM fabrication by combining a microfluidic technique I and a templating technique II. Reproduced with permission from ref. 295. Copyright 2013 American Chemical Society.

Wang *et al.*[295] combined a microfluidic technique and a templating technique, which differed from the traditional top-down and bottom-up methods,[288] to prepare multi-responsive poly(NIPAm-*co*-methacrylic acid (MAA)) photonic crystal microparticles (HPCMs) with an inverse-opal structure (Fig. 42). First, monodisperse emulsion droplets encapsulating silica nanoparticles with a diameter of around 220 nm were generated in a co-flow microfluidic device, followed by water evaporation. After washing with hexane to remove the oil phase and calcination, silica colloidal crystal microparticles (SCCMs) were obtained, which acted as templates for the formation of inverse-opal hydrogel microparticles. This was carried out in 3 steps: (1) immersion of the microparticles in a mixture of precursors and photoinitiators, (2) *in situ* UV-induced polymerization and (3) selective removal of templates by HF etching. Eventually, HPCMs with an inverse-opal structure were obtained. HPCMs bearing desired reactive functional groups (*e.g.* NIPAm as a temperature sensitive group and MAA as a pH sensitive group) showed rapid and sensitive responses to temperature and pH variations. Remarkably, the response rate was less than even 1 min. Other functional behaviors such as magnetic response could be introduced as well in HPCMs without affecting the temperature and pH responses too much.

More recently, Ye *et al.*[296] developed novel microcapsules (Fig. 43a) consisting of densely packed opal photonic crystal (PhC) cores and responsive inverse-opal PhC hydrogel shells using similar SCCB templates.[293]

The microfluidically-generated SCCB templates had high monodispersity and brilliant structural colors due to the ordered arrangement of the spherical silica nanoparticles. After complete polymerization of the pre-gel solution, the hydrogel was disrupted by immersion in a buffer solution. Inverse-opal PhC hydrogel spheres were then fabricated by etching the SCCB templates inducing pore formation (± 5 min). The etching conditions influenced the thickness of the inverse-opaline hydrogel shell, resulting in different relative refractive indices of the shell and core in the PhC microcapsule (Fig. 43b). Their reflection peaks differed only from those of SCCBs and PhC hydrogel spheres, exhibiting only one reflection peak (Fig. 43c and d, respectively). The PhC microcapsules displayed a highly ordered and interconnected macroporous structure (Fig. 43e and f), not only on the surface but also on the inside of the microcapsules, which is beneficial to diffusion imitated processes.

Inverse-opaline microsphere (IOM) crystals possess an isotropic band-gap property, differing from conventional 2D or 3D film-type colloidal ones,[71,297,298] making them attractive for optical applications. Ionic liquids are salts consisting of organic anions and cations and are liquid below 100 °C. They have some advantages, such as negligible vapor pressure, incombustibility, reasonable chemical and thermal stability and high ionic conductivity.[299] Poly-ionic liquid inverse-opaline
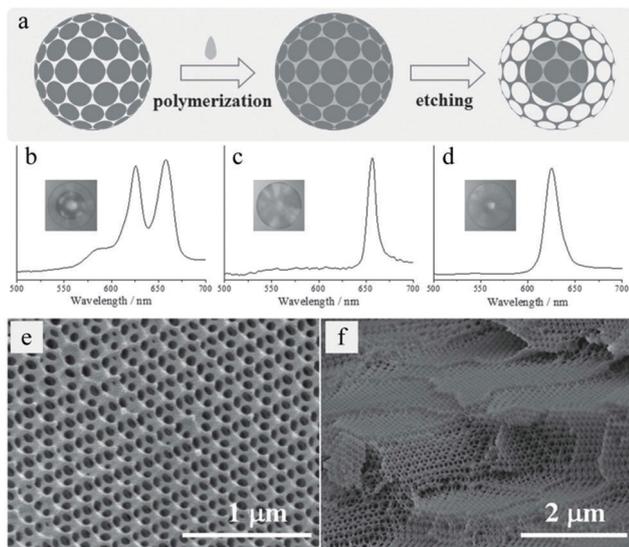
Fig. 43 (a) Inverse-opaline hydrogel sphere formation. Reflection spectra and images (insets) of (b) the inverse-opal sphere, (c) SCCB and (d) PhC hydrogel beads. SEM images of highly ordered and interconnected porous structure of the (e) surface and (f) inner section. Reproduced with permission from ref. 296. Copyright 2014 Wiley-VCH.

microsphere (PIL-IOM) crystals showed unprecedented properties beyond those of their individual constituents. PIL-IOMs were fabricated by Cui et al.[300] using a two-step procedure. Homogeneous silica nanoparticles were assembled into hexagonally packed crystalline lattices by droplet-based microfluidic synthesis,[301,302] concomitantly with infiltration of imidazolium-based PIL monomers in the voids. The PIL-IOMs were isolated after UV-induced polymerization and removal of the silica nanoparticle templates with HF. The crystals exhibited brilliant color due to their uniformity in size and architecture (Fig. 44a). Further observation under SEM (Fig. 44b and c) illustrates the highly ordered interconnected macroporous structure, distributed over the whole particle surface. The relatively wide optical stop-band could be tuned from 400 to 700 nm by introducing different diameters of silica nanoparticles. PIL-IOMs could not only be used as stimuli-responsive photonic microgels, but also as multifunctional particles that mimic conventional molecules in terms of optical properties, molecular recognition, derivation and anisotropy.

4.2.3. Ordered porous films. Based on the previous studies[303] on the influence of different parameters on the bubble bursting process, in 2016, Elsayed et al.[304] introduced a one-step fabrication

approach with a simple microfluidic junction to synthesize ordered porous films. In brief, by adjusting the gas pressure via a digital manometer and the flow rate of the polymeric solution, highly monodispersed bubbles with different sizes were firstly generated in T-junction microfluidic capillaries. And then, as-prepared microbubbles were collected on a glass slide until the bubbles burst, resulting in ordered porous structures (Fig. 45a and b). It is particularly worth mentioning that the control of pore size depends on the polymer concentration (Fig. 45c) and the surfactant type (Fig. 45d). Due to good control over the pore structure of films by employing the microfluidic technique, this strategy overcomes the previous application limitation, such as lack of pore size, shape and surface control in the scalable formation of polymeric films. Moreover, via embedding designed/selected nanoparticles, they offered a possibility to fabricate multifunctional porous films, which greatly expands and enhances their utilization in a wide range of biomedical applications, particularly in drug delivery and tissue engineering.

4.2.4. Gradient porous particles. Gradient surfaces with continuously varying pore sizes along one direction present an interesting morphology.[305–315] Collins et al.[308] utilized electrochemical etching to generate silicon films possessing a pore size gradient in the range from 10 to more than 500 nm. Later, Woodfield et al.[316] exploited the bionics structure to fabricate gradient porous morphology with pore sizes ranging from 200 to 1650 μm. Alternatively, Oh et al.[317] introduced centrifugal forces for the generation of cylindrical scaffolds with pore sizes from 88 to 405 μm. Kreppenhofer et al.[318] reported gradient porous polymethacrylate films, employing a novel microfluidic chip composed of a cascade micromixer[319–323] and a reaction chamber (Fig. 46a). Two different polymerization mixtures 1 (30 wt% EGDMA), 20 wt% BMA, 1 wt% DMPA and 50 wt% cyclohexanol) and 2 (30 wt% EGDMA, 20 wt% BMA, 1 wt% DMPA, 50 wt% 1-decanol and 0.1 wt% Rhodamine B) were injected at the chip inlets at equal flow rates. Cyclohexanol acted as a porogen to form pores with sizes around tens of nm, whereas 1-decanol gave large pores ranging from 1 to 2 μm.[324] After UV-initiated polymerization in the chip chamber (15 min), the PDMS part was removed from the glass side of the chip, leaving a 450 μm thick porous film on the glass substrate with a pore size linear gradient, and then washed with methanol and freeze-dried in a nitrogen steam. The SEM images (Fig. 46b) taken at 8 equidistant measuring points along the linear gradient 10 mm down the reaction chamber illustrate the gradient porous texture
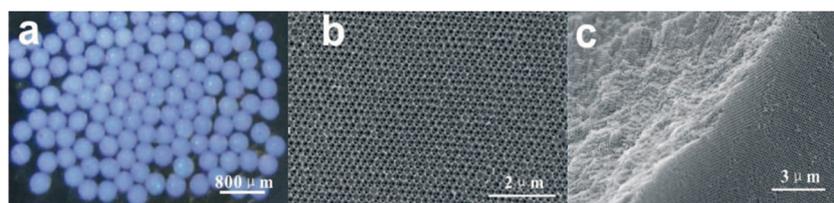
Fig. 44 (a) Optical image of the ordered macroporous PIL-IOMs. SEM images of the (b) surface and (c) cross-section. Reproduced with permission from ref. 300. Copyright 2014 Wiley-VCH.

This journal is © The Royal Society of Chemistry 2017

Chem. Soc. Rev., 2017, 46, 855–914 | 877
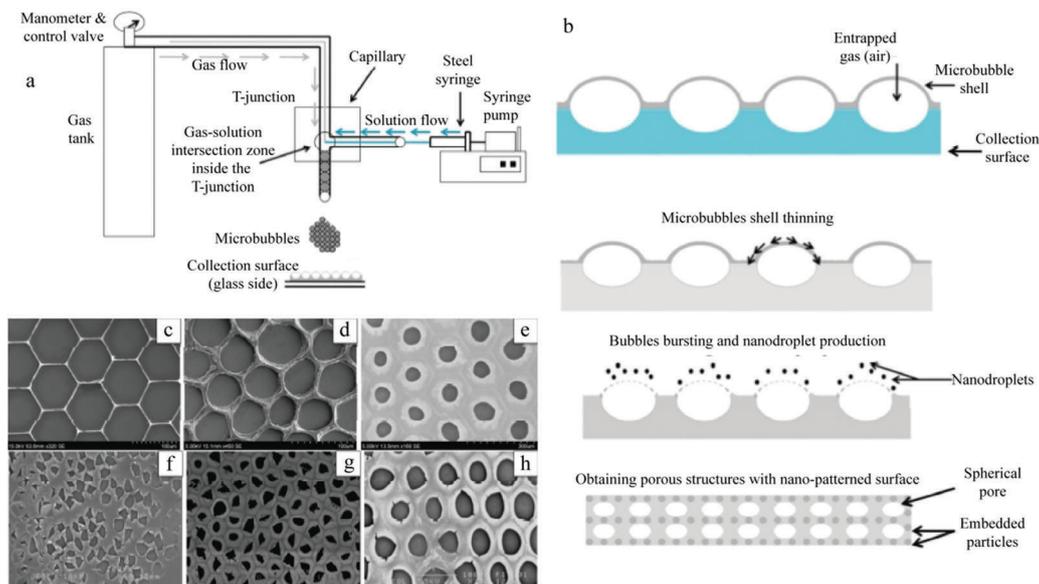
Fig. 45 Schematic illustration of (a) monodispersed microbubble generation and (b) ordered porous film fabrication process. SEM images of the effect of the polymer concentration on the porous structure: (c) 0.1 wt%, (d) 0.3 wt%, and (e) 0.5 wt%. And SEM images of the effect of the surfactant (PEG-40S) concentration on the porous structure: (f) 0.25 wt%, (g) 0.5 wt%, and (h) 0.75 wt%. Reproduced with permission from ref. 304. Copyright 2016 American Chemical Society.

ranging from micro- to macropores, with the gradient depending mostly on the flow rate. Moreover, *via* changing the chip from a horizontal to vertical layout, with mixture 1 at the upper inlet and mixture 2 at the lower inlet, a wedge-like gradient porous polymer film was obtained, caused by the density difference between the 2 mixtures (Fig. 46c and d). More recently, Watanabe *et al.*[139]
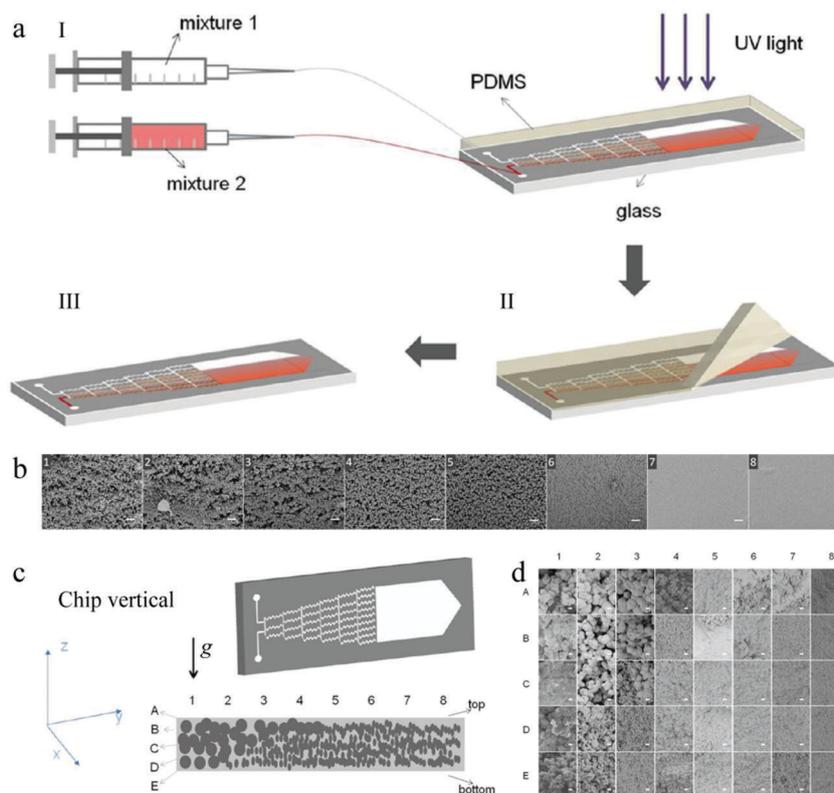
Fig. 46 (a) Fabrication and (b) SEM images of a linear gradient porous film. (c) Fabrication and (d) SEM images of a wedge-like gradient porous film. Scale bars are 20 μm (b) and 1 μm (d). Reproduced with permission from ref. 318. Copyright 2013 American Chemical Society.

fabricated smooth "skin" polyelectrolyte spheres using selective solvent extraction. Beneath the "skin", an internal pore gradient was observed with 10–100 μm pore sizes.

4.3. Radially hierarchical porous particles

Nature brings the inspiration for many hierarchical structured materials, with pores spanning in the range of a few nm to mm.[325–335] Sea sponges are typical examples. Such hierarchical porous structures stand in for their mechanical robustness and efficient biological exchange processes. In general, large size pores provide easier access with low resistance for the macromolecules, while small size pores can offer large functional surface area for molecular interaction with grafted functional groups. Especially in regenerative medicine applications, hierarchical structured materials with macropores (>300–400 μm) are indispensable to vascularise the implanted scaffold,[336] while small pores with the dimension range of 50–100 nm are desired to promote cell migration, proliferation and differentiation to speed up tissue recovery.[337] Thus, being able to control porosities in different size ranges allows us to steer the loading capacity and the mass transfer profile in cell cultures.

Methods to design meso and macroporous materials include phase separation phenomena,[338] removal of templates such as bubbles, particles and droplets[339–345] and conventional emulsification and foaming techniques, often leading to broad pore size distributions.[340,346] Additional physical or chemical gelation reactions are required to fix the structure because the templating bubbles, particles and droplets tend to coalescence and show Ostwald ripening.[210,342,347] In 2009, Lee and Weitz[27] reported the fabrication of hierarchical porous inorganic microparticles via simple evaporation of the middle solvent layer. Moreover, droplet condensation on the surface of polymer solutions is regarded as an elegant physical method to generate pores of a few micrometers.[348] Despite all these, this method was limited to obtain 2D structures with little flexibility to tune the pore size according to different requirements. Choi et al.[175] employed the W–W/W–O emulsion as a modified microfluidic device (Fig. 47a) to prepare radially hierarchical porous microbeads. The dimension and morphology of the droplets were affected by the setup.[211,212] In a dripping mode double emulsions were obtained. To form the hierarchical porous structure, they used fast evaporation of the organic solvent and emulsion templating. In contrast, slow evaporation of the solvent leads to microbeads with a dense structure. Interestingly, the final porous beads presented 2 different types of pore surface (Fig. 47b). The development of the small pores could be attributed to fast solvent evaporation, while the large pores were formed upon introducing a homogenized W/O emulsion.

Later, practical fabrication of bimodal macro/mesopore structures was introduced by Zhai et al.,[349] based on a temperature-induced gelation (rather than a polymerization reaction) integrated with a microfluidic coaxial microdevice. Methylcellulose (MC, showing reversible-thermosensitive behavior) and PEG (featured with auxiliary functional groups) were used for the synthesis of radially hierarchical porous microspheres with diameter around 490 μm. First, monodispersed droplets were generated
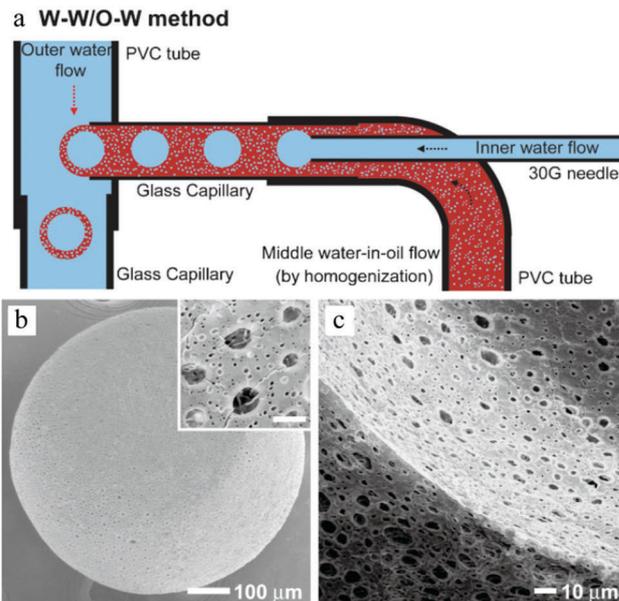
Fig. 47 (a) Scheme of a microfluidic apparatus for double W–W/O–W emulsions. SEM images of a (b) radially hierarchical porous surface and (c) cross-sections of PLGA microbeads. The scale bar of the inset in (b) is 5 μm. Reproduced with permission from ref. 175. Copyright 2009 Wiley-VCH.

and treated in water baths at 90 °C (Fig. 48a). After complete gelation, the solid spheres were washed with acetone, dried at 80 °C and calcined at 550 °C. The spheres produced from sample 1 (containing 0.50 g MC) and sample 2 (0.25 g MC) showed distinct morphologies (Fig. 48b–g). Sample 1 spheres showed a densely porous surface and homogeneous macroporous interior structure (around 1 μm), whereas sample 2 spheres presented dense pores on the surface but smaller more homogeneous macropores (around 0.1 μm) in the interior. Mesopores also widely existed in the spheres with pore sizes of 13.8 nm in sample 1 and 20.5 nm in sample 2, as determined by nitrogen adsorption–desorption measurements.

In addition, Kim et al.[350] introduced a simple one-step double emulsion strategy to prepare multi-cored microcapsules with a porous surface in a dual-continuous coaxial microfluidic apparatus (Fig. 49a). Silica particles (900 nm), pretreated with dichlorodimethylsilane (DCDMS), were added to the ETPTA solution to obtain a silica-ETPTA suspension (middle phase). The emulsion droplets were generated in the capillary device and then polymerized by UV-irradiation for 1 s. By precisely adjusting the flow rates of the 3 phases, the number of cores could also be manipulated (Fig. 49b). The diameter of the silica nanoparticles embedded in the thin ETPTA membrane was slightly greater than the membrane thickness, resulting in partial exposure of the particles on both core and outer sides (Fig. 49c). Ultimately, the wet etching process with 5% HF solution dissolved the embedded silica nanoparticles creating a well-defined porous surface.

Uniform polymeric microparticles with controllable hierarchical interconnected porosity have also been reported using W/O/W emulsions[351] (Fig. 50h). First, monodisperse W/O/W

This journal is © The Royal Society of Chemistry 2017

Chem. Soc. Rev., 2017, **46**, 855–914 | 879
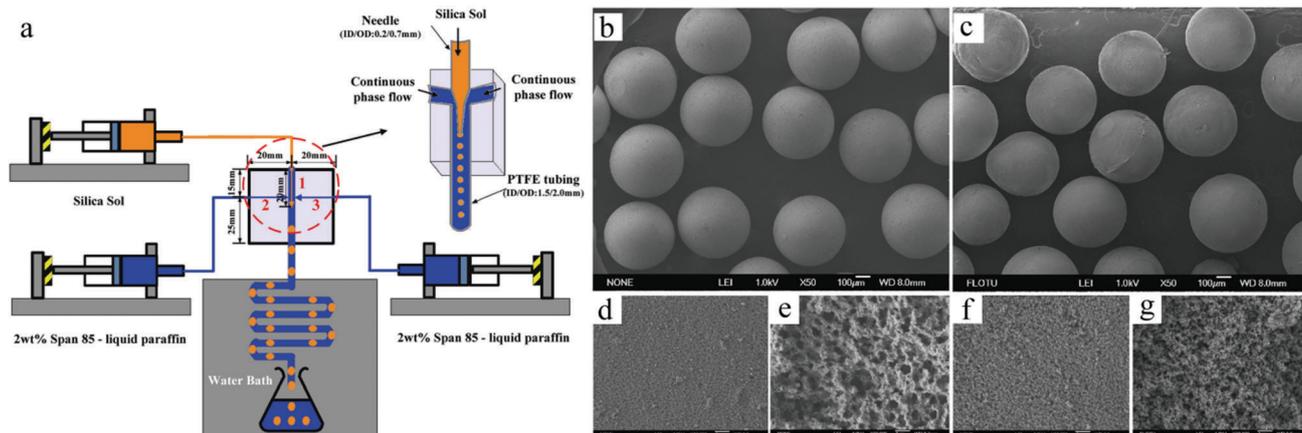
Fig. 48 (a) Schematic diagrams of the coaxial device. SEM images of (b and c) spheres, (d and f) porous surface and (e and g) internal structures of sample 1 and sample 2, respectively. Reproduced with permission from ref. 349. Copyright 2010 American Chemical Society.
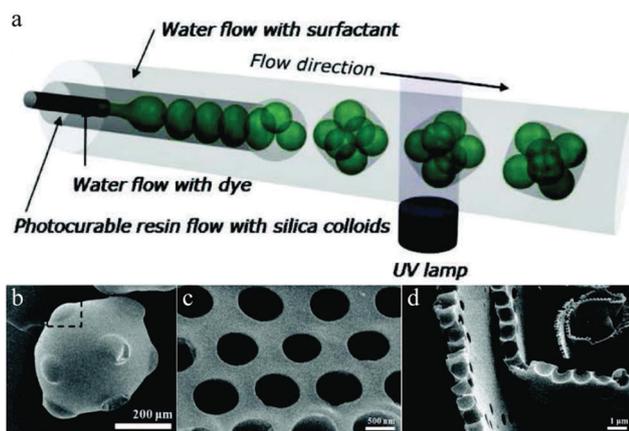
Fig. 49 (a) Schematic illustration of multi-cored microcapsule fabrication. SEM images of a (b) microcapsule with 10 cores in gyro-elongated square dipyramid geometry and porous membrane, (c) surface and (d) cross-section. Reproduced with permission from ref. 350. Copyright 2011 Wiley-VCH.
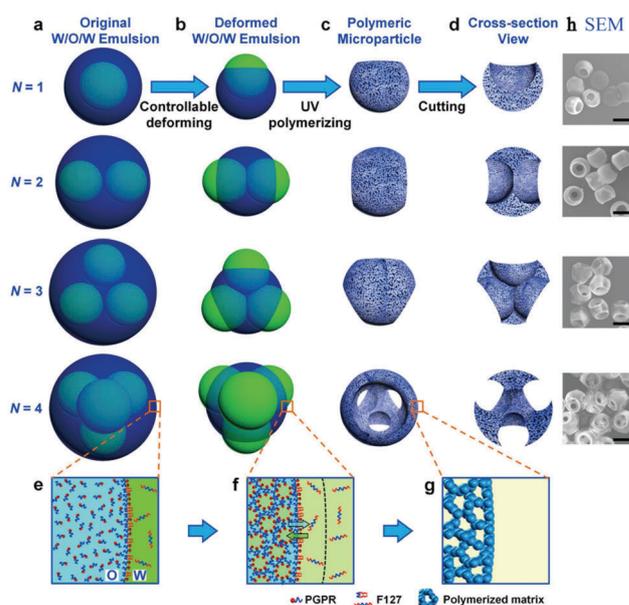
Fig. 50 (a–g) Schematic illustration of the fabrication of microparticles with controllable interconnected hierarchical porosity using W/O/W emulsions and (h) corresponding SEM images (scale bar 200 μm). Reproduced with permission from ref. 351. Copyright 2015 American Chemical Society.

emulsions were generated in the glass-capillary microfluidic device. Herein, the partially water-soluble oil phase contained a surfactant (PGPR). Depending on the numbers of inner microdroplets (N, Fig. 50a), the inner structures were closely packed in distinct ways. Mass exchange between the inner and the outer aqueous phase occurred through the oil phase and was facilitated by the surfactant. The oil phase was partially miscible with the aqueous phases, resulting in the formation of fine aqueous nanodroplets (Fig. 50e and f). After UV-induced polymerization of the monodisperse W/O/W emulsions, hierarchical porous microparticles with well-defined micrometer- and nanometer-sized pores (Fig. 51a) left from the inner microdroplets and the mass transfer-induced aqueous nanodroplets, respectively (Fig. 50c, d and g). The combination of these two size-scaled highly interconnected pore structures was translated into advanced features, such as enhanced mass transfer, increased specific surface area and flexible morphology and functionality. The introduction of magnetic nanoparticles

(Fig. 51b) showed synergy with the porous structure, useful for further application.

Carroll et al.[352] designed a surfactant micelle nano-emulsion mixture and combined it with tinplating silica microparticles to fabricate hierarchical porous spheres. Niño-emulsion droplets evolved into large pores with a diameter of tens of nm, while self-assembled surfactant micelle structures resulted in a subset of small pores with a diameter of several nanometers.[353] First, the silica precursor droplets were formed in the microfluidic device with 2 different geometries, T-junction and flow focusing (Fig. 52a), and collected in a reservoir. The remaining water and the silicate reaction by product ethanol were eliminated *via* evaporation-induced solidification. Then, the solids were
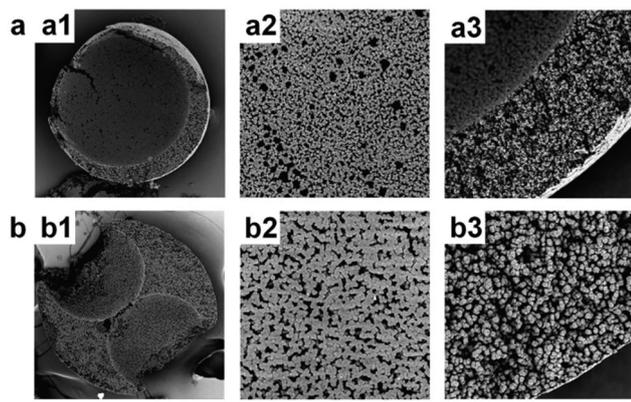
Fig. 51 SEM images of the cross-section of hierarchical microparticles obtained from a W/O/W emulsion with (a1) non-magnetic and (b1) magnetic nanoparticles, with the corresponding magnifications (a2 and a3) and (b2 and b3). Scale bars are 50 μm in (a1 and b1) and 20 μm in the rest. Reproduced with permission from ref. 351. Copyright 2015 American Chemical Society.

immersed in water or toluene to form the interconnected pores followed by washing and drying. Eventually, hierarchical porous spheres with honeycomb-like surface were obtained (Fig. 52b and c). Carroll also demonstrated that these particles can be used as replica electrocatalyst materials[354,355] and high-surface-area scaffolds.[356,357]

More recently, Fan et al.[358] provided a simple and robust in situ microfluidical fabrication of hierarchical porous poly(ε-caprolactone)/silica (PCL/SiO$_2$) hybrid microspheres. The superiority of this new strategy for radially hierarchical porous architecture lies in a synergistic effect between the sol–gel process (hydrolysis and condensation of a silane precursor) and solvent extraction in droplets. More importantly, this process not only avoided the complicated post-treatment by using porogens/sacrificed templates, but also ensures the uniform distribution of silica in the PCL matrix. In brief, the uniform droplets were firstly generated in the microchannel, and then collected in a certain concentration of PVA aqueous solution.
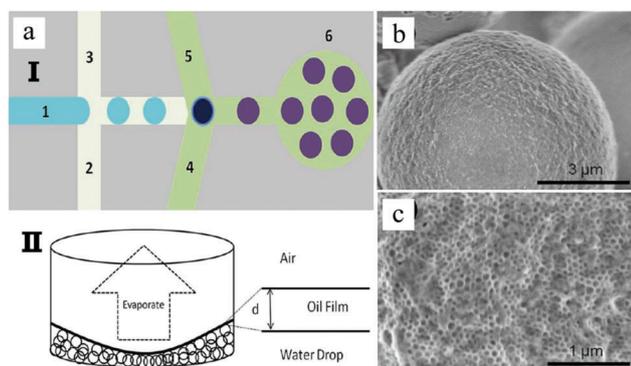
Fig. 52 (a) Illustration of microfluidic-derived hierarchical porous spheres obtained with a micellar nano-emulsion and silica microparticles. SEM images of (b) tha honeycomb-like porous surface and (c) corresponding magnification. Reproduced with permission from ref. 352. Copyright 2013 American Chemical Society.
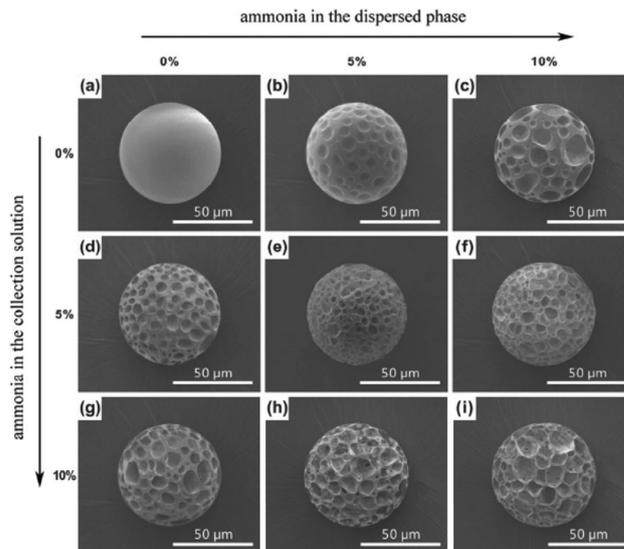
Fig. 53 SEM images of PCL/SiO$_2$ hybrid microspheres fabricated by adjusting the ammonia concentration in the continuous phase and/or collection solution. Reproduced with permission from ref. 358. Copyright 2016 American Chemical Society.

After being solidified at room temperature for 1 day, the microspheres were centrifuged and washed with excess deionized water before the final freeze-dry process. It is found that ammonia, used as a catalyst for silane hydrolysis, played a decisive role in the formation of hierarchical porous structures. At the same time, via adjusting ammonia concentration, the porous structures and the surface morphology can be easily controlled (Fig. 53).

Besides, Sommer et al.[359] used monodisperse PCL particles obtained by microfluidics[360] as sacrificed templates, combining with the 3D printing technique, to fabricate hierarchical silk porous materials with unprecedented structural control shown in Fig. 54. In detail, the microfluidically-synthesized PCL templates with different magnitudes in size were firstly added into silk fibroin-based ink to obtain the original materials by the 3D printing technique. Secondly, the removal of templates led to hierarchical porous silk-based materials. Finally, the PCL particles can be electrostatically coated with latex nanoparticles to build a porous architecture at three hierarchical levels. Due to moderate biodegradability of silk, the resulting structures turned from close to open porosity. Subsequently, these pore templating particles can be further modified with functional nanoparticles for various application fields from structural materials to thermal insulation. Meanwhile, Sommer and coworkers[360] also introduced silk fibroin scaffolds with an inverse opal structure for tissue engineering application.

4.4. Ordered hierarchical porous particles

Several research groups considered the inverse-opal architecture as a good scaffold for tissue engineering, mostly because the 3D structure is highly interconnected.[361–364] But, most of the materials were neither biodegradable nor biocompatible, which limit their potential applications. Chitosan was applied as a biodegradable material by Choi et al.[347] to fabricate

This journal is © The Royal Society of Chemistry 2017

Chem. Soc. Rev., 2017, 46, 855–914 | 881
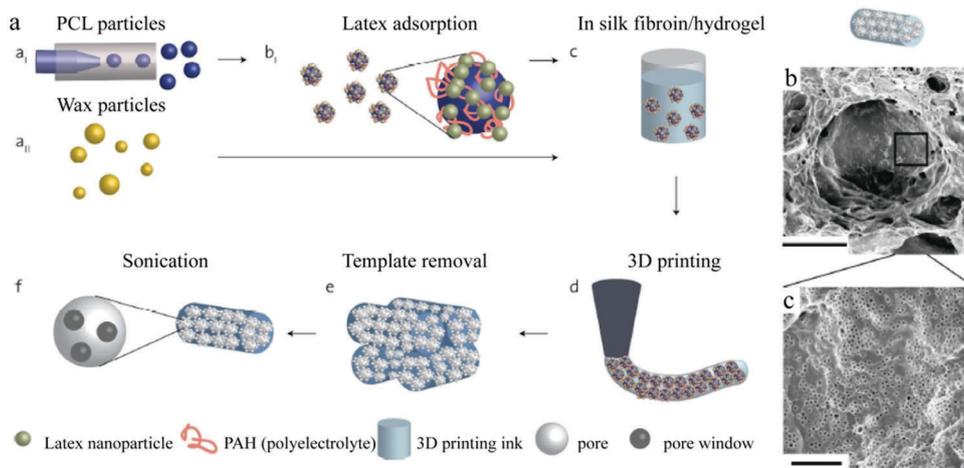
Fig. 54 (a) Schematic illustration of the fabrication of 3D printed silk fibroin with a hierarchical porous structure. (b and c) SEM images of the resulting hierarchical porous silk fibroin structures. Reproduced with permission from ref. 359. Copyright 2016 American Chemical Society.

inverse-opal scaffolds. Moreover, chitosan is not toxic, anti-microbial and biocompatible. Poly(ε-caprolactone) (PCL) microbeads with an average diameter of 147.7 μm were obtained in a simple microfluidic device (Fig. 55a) and then used as cubic close packed (ccp) lattice templates.[210] Unlike the commonly used assembling methods for ccp lattices,[362,363,365,366] here sedimentation–evaporation was employed to assemble the PCL microbeads into ccp lattices. A unique nanofibrous structure could be obtained during the freeze-drying of chitosan. Next to highly ordered macropores formed after the selective dissolution of PCL to remove the templates, randomly distributed smaller pores from a nanofibrous matrix were also present as a result of the phase separation (Fig. 55b–d). Other biocompatible materials such as gelatine, collagen and hyaluronic acid were also tested under similar conditions, but with smaller mechanical performance.

Studart et al.[367] described a versatile and simple approach to fabricate customized porous materials with up to 3 hierarchical levels. Surprisingly, the principle relied solely on the process of drying complex suspensions containing droplets, colloidal particles and surface active molecules dispersed in the absence of any type of gelation. Monodisperse polystyrene particles (400 nm) were prepared by surfactant-free emulsion polymerization. Homogeneous oil droplets were obtained in a dripping mode[212] in 2 kinds of glass microcapillary devices: co-flow and flow-focusing geometry. The flow rates of dispersed and continuous phases were constant in all experiments. The resulting oil droplets were stabilized by adsorbing either in situ hydrophobized colloidal droplets (silica or polystyrene) or surface active molecules at the oil–water interface (Fig. 56).

The stabilized droplets were polymerized and deposited on a glass substrate, followed by self-assembly (buoyancy effect) to highly ordered hexagonal arrays in the case of surfactant-stabilized droplets, whereas particle-stabilized droplets were able to form both compact ordered and random disordered arrays. For the particle-stabilized droplets, a textured coating on the surface of particles was observed (Fig. 56d). In contrast,
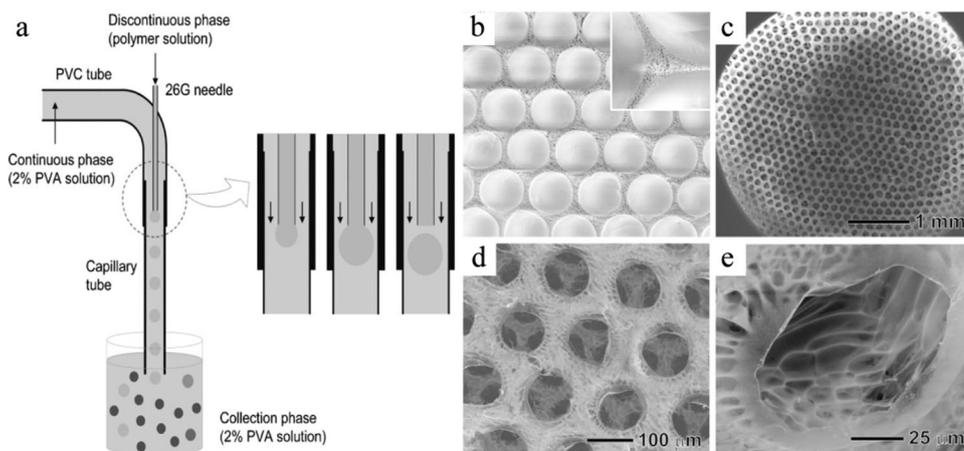
Fig. 55 (a) Illustration of the generation of uniform PCL microbeads. Reproduced with permission from ref. 210. Copyright 2009 Wiley-VCH. SEM images of (b) the freeze-dried ccp lattice, (b) top view of the inverse opal scaffold, (c) magnified view of the top surface and (d) side wall in a macropore with several smaller pores. Reproduced with permission from ref. 347. Copyright 2009 Wiley-VCH.
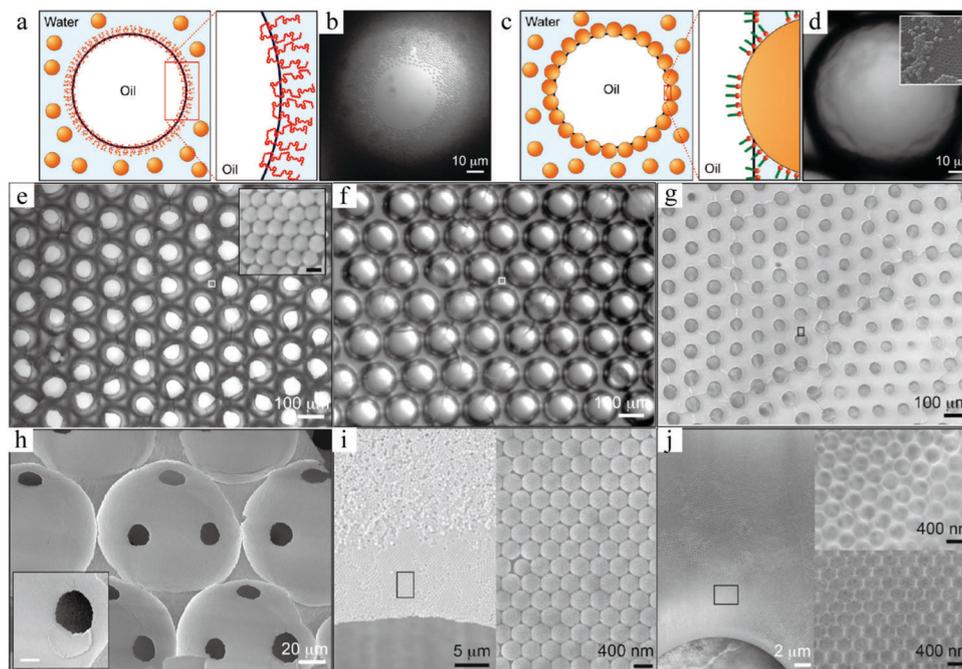
Fig. 56 (a and c) Schematic diagrams and (b and d) top views of surfactant-stabilized and particle-stabilized droplets, respectively. Hierarchical porous structures from (e) PVA-, (f) silica- and (g) CTAB-stabilized droplets. (h) Magnification of (e) illustrating the interstices between the macropores. (i and j) Magnified FESEM images of the region close to a macropore indicated in (g). Scale bars in the insets of (e) and (h) are 100 nm and 10 μm, respectively. Reproduced with permission from ref. 367. Copyright 2010 American Chemical Society.

Table 3 Hierarchical porous structure as a function of conditions for colloidal directed polymerization

Morphology	Structure with closed ordered arrays	Structure with open ordered arrays	
Droplet type	Particle-stabilized	Surfactant-stabilized PVA-stabilized	CTAB-stabilized
Dispersed phase composition	Photosensitive oil mixture containing 1,6-hexanediol diacrylate + trimethylolpropane ethoxylate triacrylate (monomers), 2-hydroxy-2-methyl-L-phenyl-L-propanone (initiator) and toluene (diluent)	Octane	Octane
Continuous phase composition	Aqueous suspension containing CTAB and silica particles	Aqueous suspension containing PVA and silica particles	Aqueous suspension containing CTAB, polystyrene particles and TEOS
Average large pore size (μm)	±140	±125	±140
Average small pore size (nm)	±110	±110	±400

only a thin air–water layer was present on the surface of the surfactant-stabilized droplets (Fig. 56b). Remarkably, the surfactant-stabilized droplets lead to an open ordered cellular structure (Fig. 56e), whereas the particle-stabilized droplets resulted in fully closed ordered arrays (Fig. 56f). Additionally, the nanoparticles compactly packed in the voids between the large pores (inset of Fig. 56e) were removed in the subsequent steps, resulting in a secondary pore hierarchy. The dried structures (Fig. 56i) presented ordered secondary pores in the vicinity of the large primary pores while more disordered pores were observed more distantly. The pore wall thickness could be adjusted by tuning the TEOS concentration in the aqueous feed (Fig. 56j), while the initial droplet diameter determined the ultimate aperture. Moreover, the type of droplet stabilizer (surfactants or particles) had a great influence on the interconnectivity between macropores (Table 3).

4.5. Complex cavity structures

Besides spherical also non-spherical monodisperse morphologies can be created using double emulsion templates. Lee and Weitz[27,79,205,243] demonstrated the synthesis of non-spherical colloidosomes with a multi-compartmentalized structure in a glass capillary microfluidic device, combining a co-flow and a flow-focusing geometry. Colloidosomes are hollow capsules whose shells consist of densely packed colloidal particles.[368–371] These materials are attractive in encapsulation and delivery applications due to their outstanding functional properties such as permeability, biocompatibility and selectivity.[343,372] Non-spherical particles were able to encapsulate multiple materials independently in different subdomains (compartments) without cross-contamination.[128] Some could pack more densely than
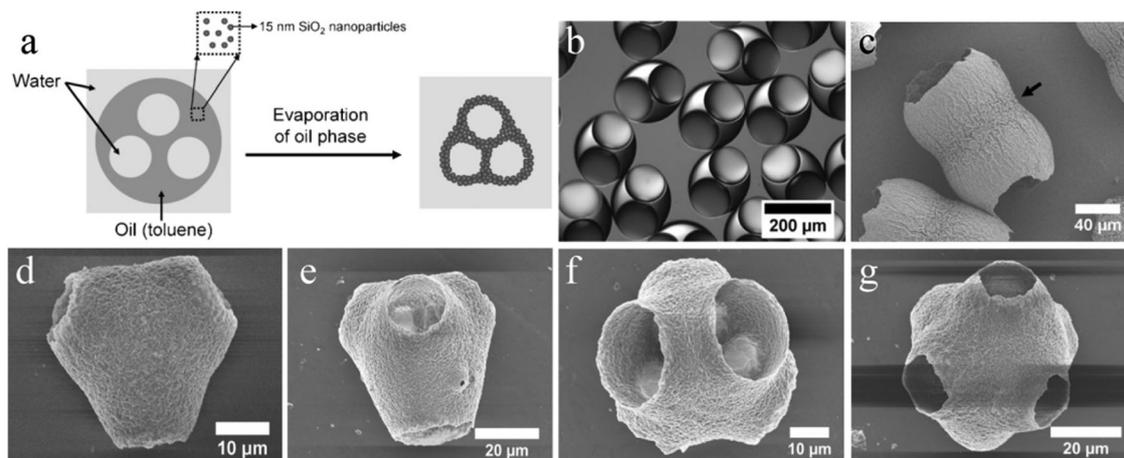
Fig. 57   (a) W/O/W double emulsion template evolving to non-spherical colloidosome with multiple compartments. (b) Optical microscopy images of aqueous droplets encapsulated by W/O/W double emulsions. SEM images of colloidosomes with (c) 2, (d) 3, (e) 4, (f) 5 and (g) 6 compartments (N). Reproduced with permission from ref. 27. Copyright 2009 Wiley-VCH.

Table 4   Generation of non-spherical morphologies directed by the droplet number of double W/O/W emulsions

Phase composition			Internal W/O drop number (n)	Compartment number (N)	Particle morphology
Outer	Middle	Inner			
0.2–2 wt% PVA aqueous solution	Toluene suspension containing 7.5 wt% hydrophobic silica nanoparticles	0–2 wt% PVA aqueous solution	2	2	Peanut-shaped
			3	3	Three links
			4	4	Triangular dipyramid
			5	5	Square pyramid
			6	6	Pentagonal dipyramid

the spherical ones due to their geometry.[373,374] W/O/W double emulsions encapsulated different sets of aqueous droplets by varying the flow rate of 3 phases in the microfluidic device (Fig. 57a). The silica nanospheres surrounded the inner aqueous droplets. Initially, during oil removal, the internal W/O interface maintained spherical morphologies while the geometry of the outer O/W interface evolved to non-spherical. After vacuum drying, non-spherical colloidosomes with various morphologies and multiple compartments were observed (Fig. 57b–g). The number of droplets determined the final morphology (Table 4). Some colloidosomes presented complex (asymmetric) structures, where the inner and outer shell surfaces consisted of different nanoparticles.[375]

Later, Fang et al.[376] described a simple one-step method for the dropwise formation of doughnut-shaped silica microparticles using a novel microfluidic FFD[377] device with a serpentine channel (Fig. 58a), which improved the control over shape and size. Along the serpentine microchannel the deformation became more pronounced and the droplets gradually shrunk during solidification from 75 µm spheres to 25µm doughnut-shapes (Fig. 58b and c), as a result of the buckling instability at the interface. A thin membrane (2–3 µm) connected the 2 (asymmetric) cavities (Fig. 58d).[378] According to the drying hydrodynamics, either pancake-shaped or torus-shaped silica microparticles could also be created by adjusting the experimental conditions, such as the silica content in the dispersed phase (TEOS + triethyl amine), the flow rates of dispersed and continuous phases,[297] etc.
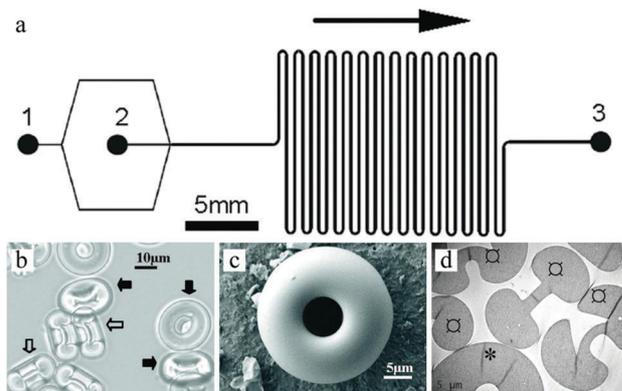
Fig. 58   (a) PDMS device with serpentine channel, (b) optical microscope tilted side view of doughnut-shaped silica particles, (c) SEM image of whole particles and (d) top (*) or side (☐) view TEM image of cross-section of particles. Reproduced with permission from ref. 376. Copyright 2011 American Chemical Society.

4.6.   Customized macroporous particles (flow lithography)

All the particle synthesis methods described above are based on the precise control over the specific emulsion droplets inside microfluidic devices. The particle morphology in these methods is restricted to spheres or some deformed sphere shapes, such as hemispheres or rods. Photolithography offers a much easier route to yield such non-spherical particles, because the method employs versatile photomasks to define the shape.
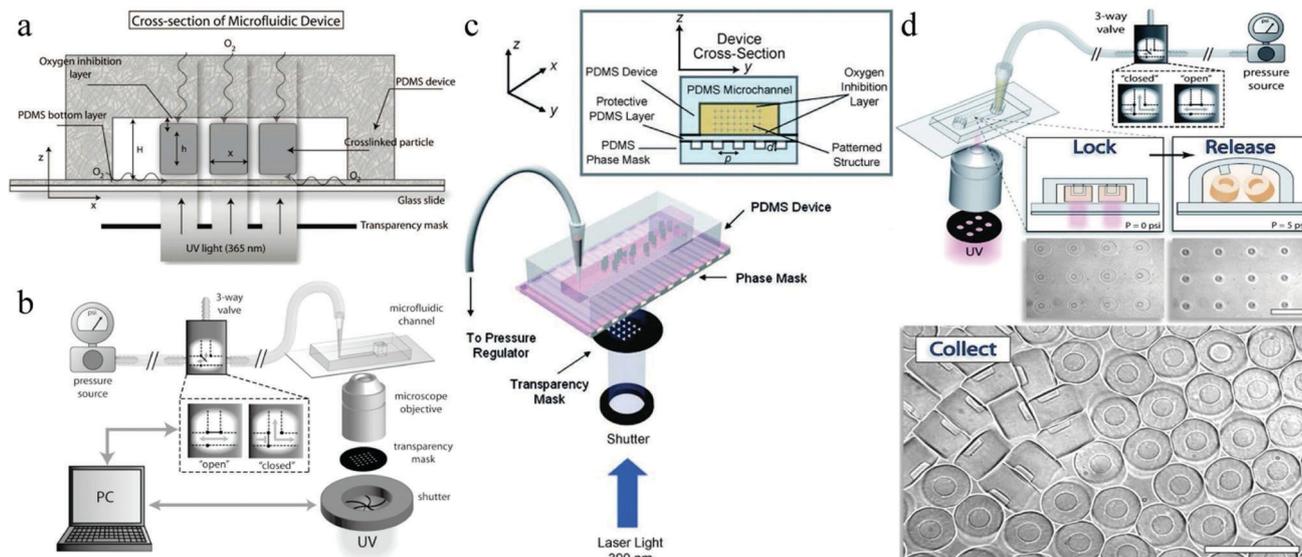
Fig. 59 (a) Cross-section of a PDMS microfluidic flow lithography device. Reproduced with permission from ref. 380. Copyright 2008 American Chemical Society. (b) SFL device using a 3-way solenoid valve for rapid flow start and stop before and after polymerization. Reproduced with permission from ref. 379. Copyright 2007 The Royal Society of Chemistry. (c) SFIL. Reproduced with permission from ref. 382. Copyright 2007 Wiley-VCH. (d) LRL. Reproduced with permission from ref. 383. Copyright 2009 The Royal Society of Chemistry.

On the other hand, it has not been used often in the fabrication of particles due to the discontinuous nature of the process (low throughput). Besides, photoresistant materials are not ideal for applications that require biocompatible particles.

In order to fabricate the non-spherical particles, novel microfluidic methods relying on photolithographic techniques were introduced recently.[54,379] Arrays of mask-defined polymeric particles were formed under UV-light in the PDMS device in an automatized way. Fig. 59a shows a cross-section of the microfluidic device. Mask defined shapes were cross-linked in the centre of the device under a dynamic oxygen atmosphere, which was constantly diffusing through the PDMS wall and forming the inhibition layer above and beneath the particles. The thin oxide layer prevented clogging of particles allowing them to elute smoothly.[380,381] One technique used a continuous flow of monomers passing through the microfluidic device producing arrays of arbitrary masked particles (continuous flow lithography, CFL). Another technique employed masks which were embedded inside the microfluidic device. Eventually, 4 types of flow lithography were developed (Table 5): CFL, stop flow lithography (SFL), stop flow interference lithography (SFIL) and lock and release lithography (LRL). An additional advantage over droplet-based methods is the possibility to fabricate particles with more than 3 different sections. Extending photolithography from photoresistant materials to other more bio-friendly materials could open the range of applications.

4.6.1. Continuous flow lithography (CFL). Dendukuri et al.[54] developed the CFL method. They combined the advantages of microfluidic techniques (continuous processing and laminar co-flow) and projection-photolithography (higher resolution and precise shape control). An oligomer stream continuously flew in the microchannel while a transparent mask (inserted in the field-stop position of the microscope) was used to define the final shape. The exposed parts of the oligomer were cross-linked

Table 5 Characteristics of flow lithography techniques

Technique (year)	Characteristics
CFL (2006)	Automatized fabrication of non-spherical particles with 2D-extruded shapes down to 3 μm Low Pe flows and pattern blurring Structures with poor resolution
SFL (2007)	Automatized fabrication of heterogeneous biocompatible 2D-extruded particles Improved resolution for more detailed structures (1–2 μm) Sharp interfaces between different sections of particles
SFIL (2007)	Predictable internal 3D structures in one shot High surface-area-to-volume ratio Controllable 3D porosity
LRL (2009)	3D multifunctional particles with complex structures Automatized fabrication of composite particles with multiple overlapping sections
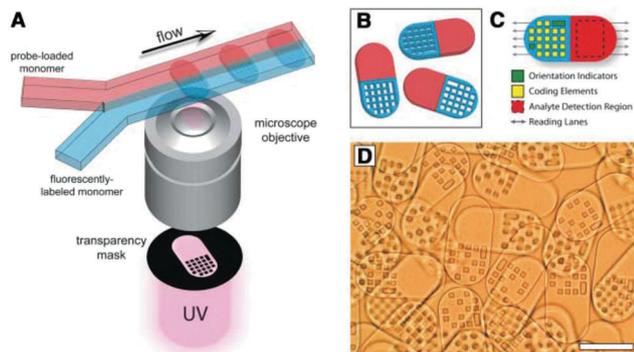
Fig. 60 (A) Fabrication of dot-coded particles, (B) single-probe half-fluorescent particles, (C) particle subdomains for encoding and analyte detection and (D) differential interference contrast (DIC) image of particles (scale bar 100 μm). Reproduced with permission from ref. 384. Copyright 2007 Science.

Fig. 61 (a) Optical image of 5% PEG700DA (M_w 700 Da) macroporous hydrogel with 20% PEG10000 porogen and (b) SEM image of 5% PEG700DA macroporous hydrogel slab with 20% PEG35000 porogen. Reproduced with permission from ref. 165. Copyright 2010 American Chemical Society.

upon exposure to UV-light through the transparent mask to induce solidification. The particles were eluted from the device with the continuous phase.

Most of the traditional approaches to make multifunctional encoded particles used for biomolecule analysis are complicated and time-consuming. Besides, they often generate only a limited number of particles. The processes for encoding, functionalizing or decoding active substrates (particles or surfaces) are expensive. Pregibon et al.[384] presented a flexible and convenient CFL based approach, combining particle fabrication, encoding and probe incorporation into a single process. The obtained multifunctional particles possessed more than a million unique codes. The mix of 2 monomer flows (one loaded with an acrylate-modified probe and the other one with a fluorescent dye) constituted the laminar flow in a microfluidic channel and were then polymerized by UV-light (Fig. 60A). Particles with different regions were created in a single step: a graphically encoded region (fluorescent probe) and a probe-loaded region (modified probe). PEG, known as a bio-inert polymer, was used as the particle anchor point to ''block'' surfaces after the direct incorporation of the probes into the particles. PEG as a transparent material also allowed the fluorescent signal to pass through both sides of the particles. The resulting particles were extruded in 2D shapes (Fig. 60B–D) with macroporous ''block'' holes. Their chemical components were determined by the co-flowing monomer stream composition. Particles were designed to be ''read'' along 5 lanes along their length, with alignment indicators as the identification of the code position.

Later, Lee et al.[165] studied the use of PEG as an effective porogen to create a macroporous hydrogel and a hydrogel slab within microfluidic channels. The inert PEG occupied the space within the polyacrylamide hydrogel without affecting the protein activity.[385] In contrast to other common porogens, PEG is more hydrophilic and can be dissolved in water and therefore it was removed efficiently from the hydrogel.[386] Pre-polymer solutions with 4% (w/v) polyacrylamide were exposed to 320–500 nm UV-light through a transparency mask, placed between the light source and microchannel. Upon addition of PEG porogens at
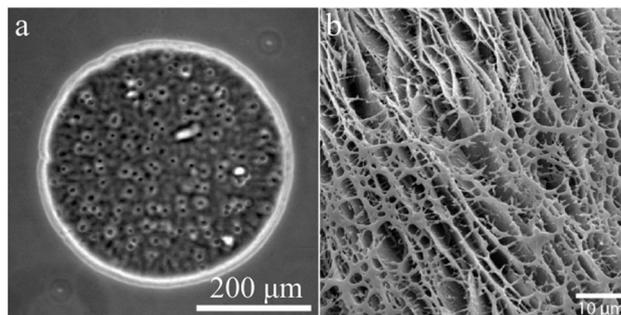
concentrations higher than 5%, the polymerized hydrogel (Fig. 61a and b) became opaque and macroporous as a result of polymerization-induced phase separation. Higher loads of PEG porogens increased the porosity but decreased the structural strength. To increase the fabrication throughput, the flow rates of the different phases needed to be enhanced, but that leads almost inevitably to particle smearing and poor repeatability (unacceptable deformation) due to the limited UV-exposure time.[379]

4.6.2. Stop flow lithography (SFL). SFL was developed to address CFL's inherent limitations[379] (Fig. 59b). The monomer solution (composed of a precursor, a porogen and a photo-initiator) was fed to the PDMS microfluidic device where a laminar co-flow was already established. As the flow suddenly halted, the feed was exposed to UV-light through a defined transparent mask. After that, the flow is restarted again, carrying the polymerized particles from the device into a collector while the laminar co-flow streams re-established again for the next cycle.[381] The frequent switching between stop and flow modes required to respond rapidly to the pressure changes in the device. The SFL production throughput can be up to 1000 higher compared to CFL. SFL also leads to sharper interfaces among the different sections by using high flow rates which are stopped abruptly before subsequent polymerization.

4.6.2.1. Regular macroporous particles. Recently, Li et al.[387] and coworkers synthesized highly macroporous particles via a microfluidic flow lithography approach with low-cost porogens (Fig. 62). The particles' shapes depend on the designed photo-mask. Besides, a UV polymerization-induced phase-separation process results in a highly porous architecture with controllable pore size ranging from 100 nm to 500 nm. Moreover, they also systematically studied the pore-forming process with different operating parameters, such as the porogen type, porogen concentration and UV intensity.

4.6.2.2. Irregular macroporous size square hole particles. The group of Doyle also demonstrated the advantages of SFL.[379] The CFL and SFL methods were compared for the fabrication of a fixed number of particles using the same type of mask,

886 | Chem. Soc. Rev., 2017, 46, 855–914

This journal is © The Royal Society of Chemistry 2017
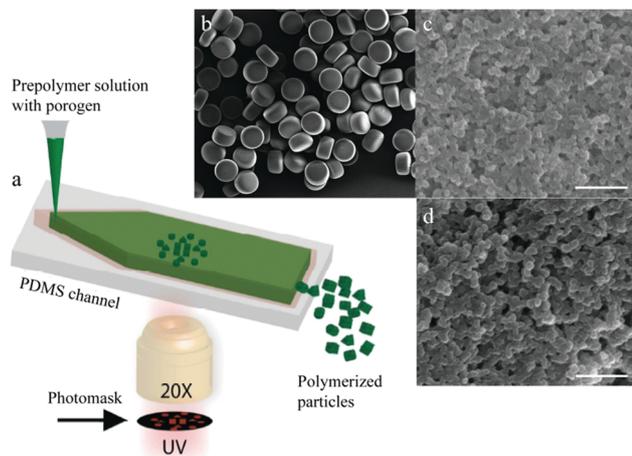
Fig. 62 (a) Schematic illustration of SFL porous particle fabrication. SEM micrographs of (b) a certain number of polymerized porous particles, and (b) surface and (c) cross section of polymerized porous particles, respectively. Scale bars are 2 μm (b and c). Reproduced with permission from ref. 387. Copyright 2016 American Chemical Society.

UV-exposure time (0.05 s) and channel geometry (10 μm in height, 200 μm width and 1 cm length) (Fig. 63a–c). The insets show magnifications of the transparency masks employed. The difference between the inner and outer side dimensions of the concentric squares were 50, 20 and 10 μm, used for the preparation of particles with dimensions around 6, 2.5 and 1.25 μm, respectively (Fig. 63d, f and h). They showed well-defined morphology, the smaller particles however lacked sharp edges (Fig. 63h). The particles prepared using the CFL method are shown in Fig. 63e, g and i, having blurred edges and being less uniform than the ones obtained using the SFL method.

4.6.2.3. Macroporous microgears. SFL was also reported as an effective tool for the generation of particles with more complex geometries, such as microgears, with uniform sizes ranging from 20 to 300 μm.[388] Unlike simple geometries which could be obtained in short time, the complex microgears required much longer time to ensure complete polymerization to avoid their destruction during the ejection process. To enhance their structural integrity, the colloidal microgears were transformed to dense glassy silica ones by sintering for 3–10 h. After 10 h at 1150 °C, smooth transparent surfaces with dense internal structures were produced (Fig. 64a and b), while after only 1 h the microgears became translucent and even opaque, but their surface remained rough on the same size scale of the individual silica microsphere building blocks (Fig. 64c and d). Fully-open structures however have not yet been obtained, but might be created using other polymer types, like those used for photo-resistant materials.

4.6.2.4. Bar-coded particles. Permeable PEG hydrogel particles consist of several spatially segregated regions, each hosting a graphical code in their unpolymerized macroporous holes. Some particles even carry various probe strips for multiplex target quantification. Particle-encoding holes can have different sizes
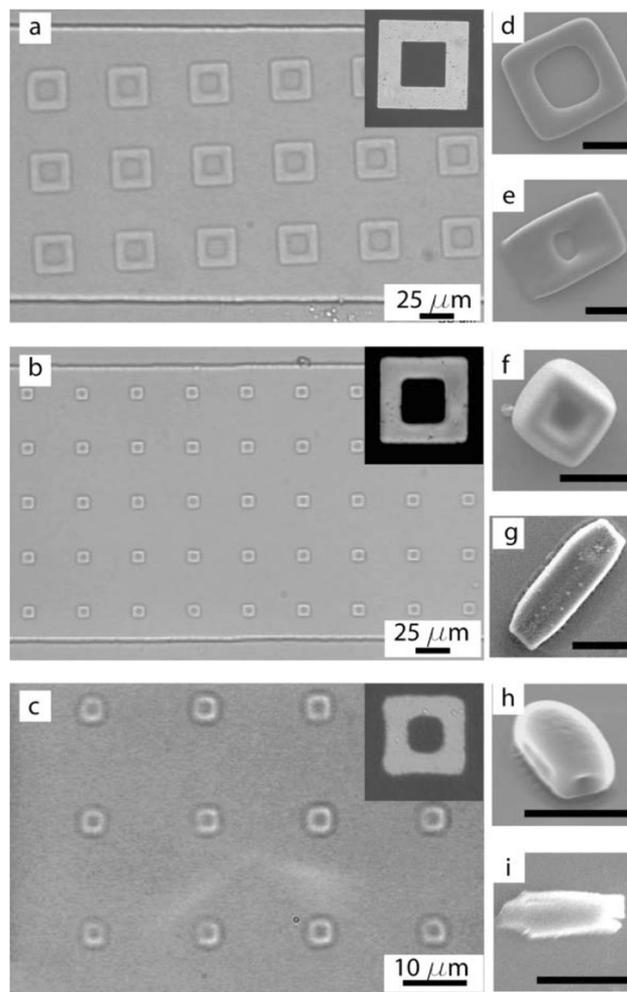
Fig. 63 Concentric square masks, having differences between inner and outer sides of (a) 50, (b) 20 and (c) 10 μm, used for the SFL generation of macroporous square particles. (d, f and h) SEM images of SFL particles and (e, g and i) particles made with the same masks using CFL under the same conditions as SFL. The scale bars are 10 μm (d–i). Reproduced with permission from ref. 379. Copyright 2007 The Royal Society of Chemistry.

representing 4 coding 'bits' (0, 1, 2, and 3). Besides, an extra bit (4) is used to provide the starting signal. These codes help to identify the antibody covalently attached on a separate probe region of the particle. The five bits could be arranged in 192 unique codes,[381] if needed, similar to bar-coded chips.[389] The task of the porous 3D gel matrix was to improve the kinetics of the recognition chain reaction of nucleic acids.[390,391] The pore size could be modulated by varying the load of the cross-linking agent and porogen(s) in the precursor solution.

More complex particles with multidimensional anisotropy could also be fabricated with advanced microfluidic designs.[383,392–394] However, they sometimes lacked technological solutions to rapidly decode particles and quantify target binding in a high-throughput manner, suitable for clinical research applications.[395–397] To expand the application of bar-coded hydrogel particles, Doyle and his group developed a versatile microfluidic flow scanner, which decoded the particles in an accurate way and up to

This journal is © The Royal Society of Chemistry 2017

Chem. Soc. Rev., 2017, **46**, 855–914 | 887
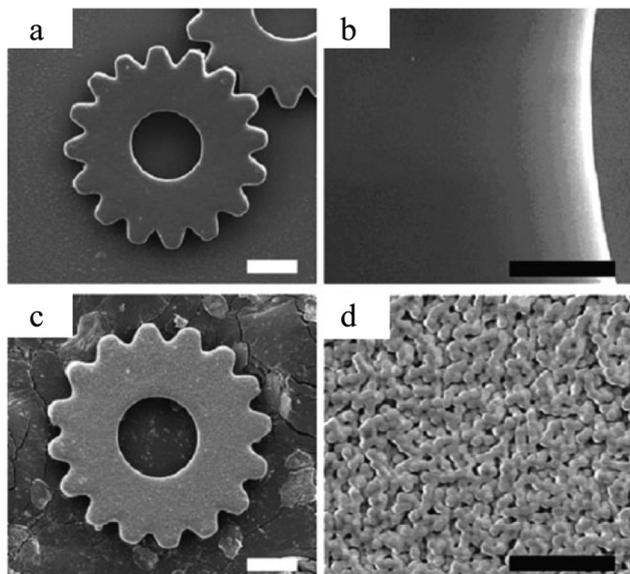
Fig. 64 SEM images of (a) glassy silica microgear sintered at 1150 °C for 10 h, including (b) high magnification and (c) porous silica microgear sintered at 1150 °C for 1 h, including (d) high magnification. Reproduced with permission from ref. 388. Copyright 2008 Wiley-VCH.

25 targets per s, with multiplex detection encoded. The device consisted of 4 major parts: (1) creation of bar-coded micro-particles, (2) protein target labelling, (3) scanning and analyzing the particles and (4) automated target identification. The bar-coded hydrogel particles were produced using a well-designed SFL device (Fig. 65c) described by Dendukuri et al.,[379] a flow control equipment used by Bong et al.[398] and a scan system built on the microscope that was used for particle generation.[399,400] Stop-flow cycles were adjusted by the pressure and synchronized with

UV-light pulses to simultaneously synthesize, encode and functionalize. By high-resolution design of the particle layout, hosting different adjacent chemical functionalities, reliable code readouts could be achieved (Fig. 65a). Earlier, scans occurred on equally spaced probes,[401] whereas Boyle used a 30 μm width blank region inserted in the particle to separate the code and the probe. Another blank region was incorporated at the end of the particle to ensure symmetrical exposure of the probe to the carrier (Fig. 65b). Other studies also explored bar-coded microparticles for protein detection and other applications.[399,402–406]

4.6.2.5. High AR functional layered sheets. The aspect ratio (AR, the ratio of the channel width to height) of microchannels is a critical parameter of PDMS chips. ARs below 20 resulted in weak mechanical strength.[407] Channels with too high ARs resulted in sagging and limited sheet formation. By utilizing a glass support in stop-flow lithography, the generation of functional layered sheet structures with high ARs was realized in one step.[408] Li et al.[409] introduced slit-channel lithographs to prepare single- and even multiple-layer hydrogel sheets with controllable pore shapes and surface morphologies, designed for utilization in tissue engineering. The UV-shutter and the solenoid valve were precisely synchronized using a digital controller (Fig. 66a), which is important for the special morphologies of the sheets. In the single-layer sheet synthesis, a Pacman-arena styled sheet (Fig. 66b) with a pore gradient pattern ranging from 5 to 300 μm (Fig. 66c) was obtained, which can be used in multi-component filtrations.[410] The pore shape was also altered by adjusting the location of the UV-focal plane along the microchannel. When setting the focal plane in the middle of the channel, the light beam reached the photomask in a straight angle resulting in sheets with uniform cylindrical pores (Fig. 66d).
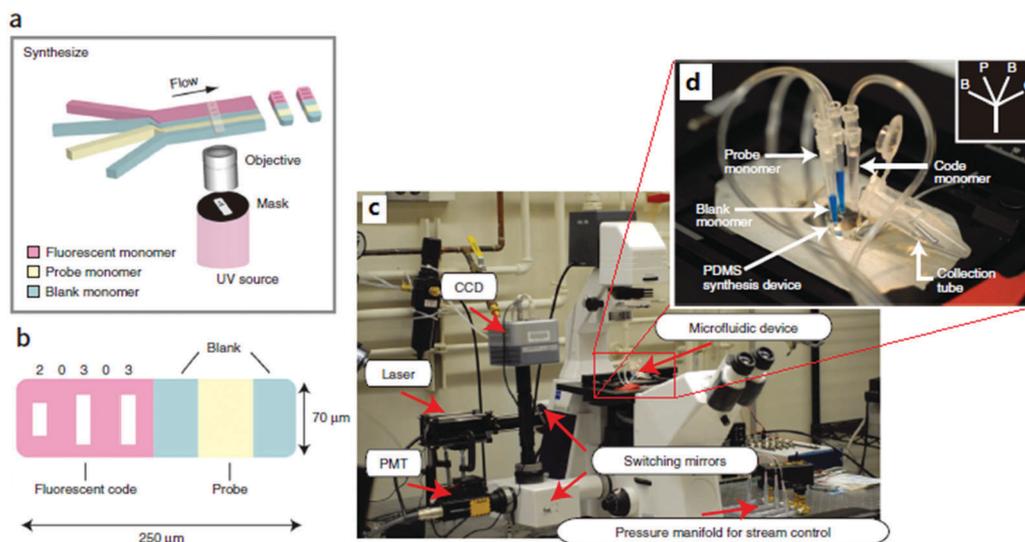
Fig. 65 (a) Illustration of the fabrication of single-probed particles. (b) A bar-coded particle with code 20303, (c) microscope setup for synthesis and scanning: laser and PMT for scanning, UV for polymerization and CCD for synthesis and alignment and (d) blue colored feed to identify and adjust the monomer flow widths easily during the fabrication process: B: blank, P: probe and C: code. Reproduced with permission from ref. 381. Copyright 2011 Nature America.
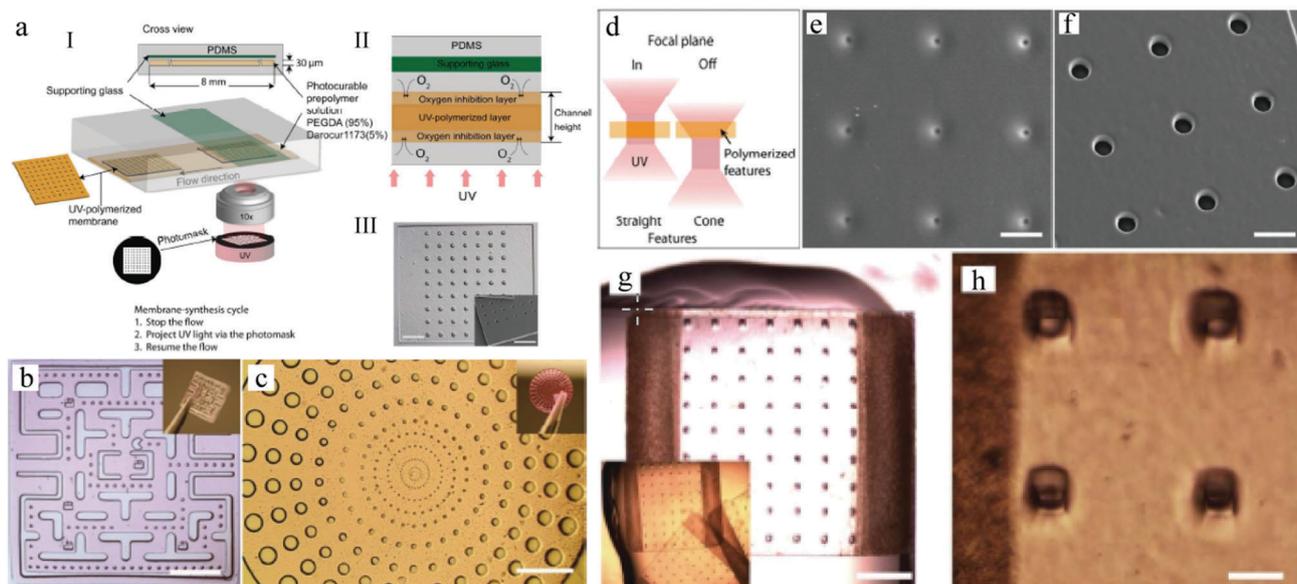
Fig. 66 (a) Illustration of hydrogel sheet production, (b) Pacman-arena styled sheet, (c) gradient pore pattern and (d) cylindrical and conical pore formation. SEM images of the (e) cylindrical and (f) conical pores in the sheets and (g) multi-layered magnetic hydrogel sheets with square macropores and (h) corresponding magnification. Scale bars are 1 mm (b, c and g), 40 μm (e and f) and 100 μm (h). Reproduced with permission from ref. 409. Copyright 2014 American Chemical Society.

When lowering the focal plane location, the sheet showed conical pores caused by the inclination of the light beam (Fig. 66e and f). Both types of sheets were used in cell culture and biochemical analysis.[411–415] Multi-layered sheet structures were obtained by introducing an external magnetic field. Fig. 66h shows 3 magnetic hydrogel sheets self-assembled into a 3D hydrogel structure with 60 μm square pores, good for nutrition supply and waste removal in large tissue growth. Compared to other techniques such as scanning beam lithography,[416,417] photolithography[418,419] and soft/hard mold lithography,[407,420] the slit-channel lithography technique simplified the fabrication process considerably.

4.6.3. Stop flow interference lithography (SFIL). The above lithography methods are restricted to particles with 2D extruded shapes. SFIL was developed by combining phase mask based interference lithography with SFL to form particles with predictable internal 3D structures in one step (Fig. 59c). Poly(ethylene glycol)diacrylate (PEGDA) equilateral triangular prisms (present in an oligomer film) with a side length of 60 μm and a thickness of 25 μm were reported.[382] Via controlling the light intensity and the inhibitor concentration, other structures with various surface morphologies and volume fractions were created (Fig. 67a–c). The obtained particles lacked a fully open 3D porous structure. Further optimization of the hydrogel materials and the phase mask enable them to make high-porosity hydrogel/air bicontinuous structures.

Fig. 67a and b show the cross-sectional views of the 3D structures obtained at a short exposure time/high inhibitor load and long exposure time/low inhibitor load, respectively. The latter 3D structures contained smaller pores and had a higher volume fraction. Upon shrinking in ethanol, flower-shaped structures were formed (Fig. 67c).

4.6.4. Lock and release lithography (LRL). More recently LRL was introduced for the fabrication of a wider range of 3D multi-functional particles containing complex patterns,[383] taking advantage of the CFL/SFL method and the deformation phenomena in PDMS devices upon changing the external pressure. This was important to lock and release the particles from the 3D PDMS ceiling, which contained positive protruding relief structures to facilitate this. First, a UV-sensitive monomer
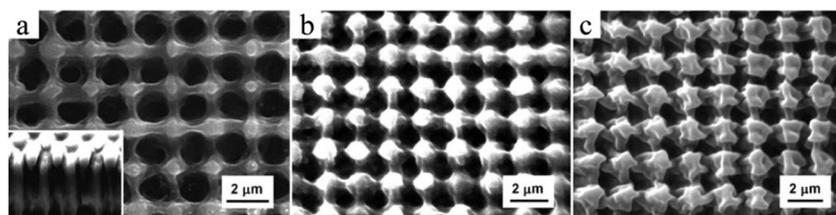
Fig. 67 SEM images of PEGDA structures with different morphologies and volume fractions, fabricated with the same phase mask and (a) 700 ms exposure time with 1.2 wt% hydroquinone (inhibitor), (b) 1000 ms exposure time and 0.3 wt% hydroquinone and (c) special flower shapes fabricated from ethanol suspension and 300 ms exposure time. Reproduced with permission from ref. 382. Copyright 2007 Wiley-VCH.

stream was stationed in the microfluidic channel using a 3-way valve. Then, lithographic printing structures were locked in the deformed PDMS ceiling by changing the external pressure. Finally, the particles were released from the deformed ceiling *via* high pressure and recovered from the eluent. 3D particles with macroporous grooves were fabricated in a semi-continuous manner using an automated valve system (Fig. 59d). In order to obtain fine (macro)porous structures, the transparency masks were combined with well-defined interference masks.[382] Besides the mask-defined shape, the particle morphology was also influenced by the channel geometry because this determined the channel deformation degree to lock, polymerize and release the created structures. The channel width needed to be designed tediously, especially at the inlet where most of the locking occurred and at the outlet to avoid clogging by the particles formed. By using stop-flow, higher resolutions and a higher throughput up to 10^6–10^7 particles perusing a single microscope were attained.[379]

The release time was also important. Particles could be released at a critical pressure as a function of the device deformation. While the low pressure was maintained, the monomer exchange continued and addition of new chemical groups was possible before the release was started. This way, composite particles with multiple chemical regions and complex porous structures were obtained (Fig. 68a). First, the multi-inlet was filled with one type of monomer and precisely locked. Subsequently, by tuning the pressures of the inlet streams (but keeping them below 10 psi), locked structures with chemistry 1 were covalently linked to chemistry 2 through mask overlapping, then polymerized under UV-light and released by high pressure (Fig. 68b–f). The mask was compatible with different chemistries to selectively polymerize through overlapping, resulting in different particle types. Fig. 68g shows a particle obtained by applying 3 chemistries.
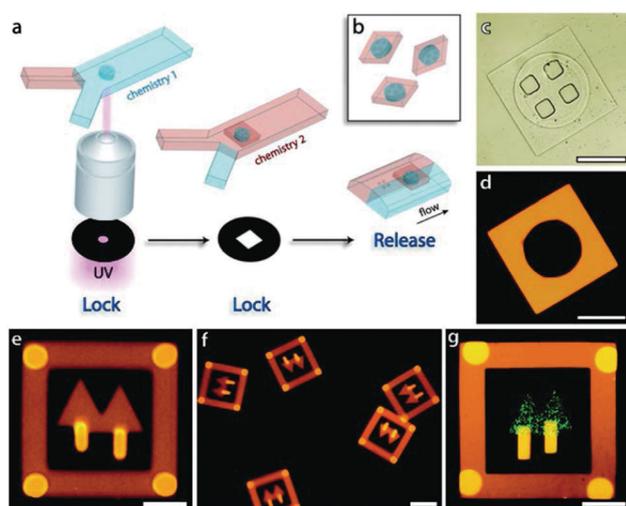
Fig. 68 Composite particle (a) synthesis, (b) structure, (c) DIC image and (d) fluorescence microscopy image. Fluorescence microscopy images of (e and f) composite particles with an "autumn tree" pattern, with 6 thicker locks appearing as brighter regions and (g) composite particle with a "spring tree" pattern. Scale bars are 100 μm (c, d and f) and 50 μm (e and g). Reproduced with permission from ref. 383. Copyright 2009 The Royal Society of Chemistry.

The lag times were critical, as they determined the fluidic exchange and mask alignment. However, the production throughput decreases when multiple chemistries are employed.

5. Applications

5.1. Catalytic applications

The development of different porous materials has opened great opportunities for catalytic applications, mainly as supports for catalysts and as nanoreactors (Fig. 69). They can provide efficient mass and heat transfer and host abundant catalytic active sites. Graphite, a nanostructured porous material, has intriguing structural features with a hexagonal close-packed opened porous structure. Natural and artificial zeolites, with pore sizes less than 1 nm, are widely used as catalytic nanoreactors.[421,422] Here, macromolecules cannot enter and leave the confined space. Metal–organic frameworks (MOFs) exhibit similar structures with sub-nanometer-sized pores.[423] Moreover, MOFs can act both as catalyst supports and as active sites. In general, catalytic active sites are loaded by covalent grafting, heteroatom doping or nanoparticle deposition. Larger-pore-sized mesoporous materials have also been developed.[424,425] Among these materials, MCM-41 and SBA-15 are widely used in various catalytic reactions.[426] Compared with microporous structures, mesoporous ones provide larger pore volumes, which benefits the mass transfer. Unfortunately, the increase of porosity can result in less stable cellular structures[427,428] and further restrict their performance over time. Carbon nanotubes with pore sizes ranging from 1 to 100 nm[429–435] and macroporous materials have also been employed for catalytic reactions.[22,436–439]

Materials with hierarchical porous structures on the nano- and micrometer scales have also been explored to improve conventional micro-/meso-/macroporous materials as catalytic supports and nanoreactors.[440–442] For this reason, the development of microfluidic techniques can play an important role in catalytic applications. Wacker *et al.*[166] created magnetic macroporous spheres in a microfluidic device using silica particles and iron oxide nanoparticles and then functionalized them with horseradish peroxidase (HRP), frequently used as a signal amplifier in immune assays.[443] This way the HRP functionalized particles could be recovered easily.[444,445] Carroll *et al.*[352] designed surfactant micelle/oil nanoemulsions and combined them with silica microtemplates to fabricate hierarchical porous
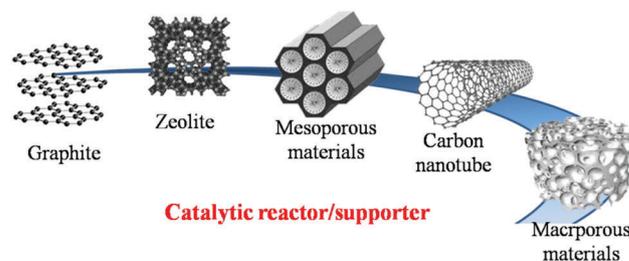
Fig. 69 Common porous materials used as catalytic supports with increasing pore sizes and nanoreactors with gradually increased reaction spaces.

890 | *Chem. Soc. Rev.*, 2017, **46**, 855–914

This journal is © The Royal Society of Chemistry 2017

spheres to improve the mass selective transfer in catalysis, but also for electrocatalysis materials.[354,355] More recently, Kim *et al.*[72] also demonstrated that the porous microparticles can be used as catalyst supports thanks to their intrinsic structural features. However, although microfluidically-generated porous materials possess so many distinct advantages, for future catalytic application, more efforts should be devoted to control their structures and morphologies. With the rapid progress of microfluidics in porous material fabrication, macroporous materials with higher specific surface area, larger pore size and pore volume, as well as better multi-functionalization superior to the current porous materials obtained by a conventional approach will certainly face a bright future in modern catalytic research and applications.

5.2. Optical applications

In recent years suspension-mediated arrays were exploited.[446] Compared with the conventional microarrays on a plate,[447,448] they offer greater flexibility. In particular, self-assembled periodic arrays of colloidal photonic crystals (CPCs), containing photonic band gaps (PBGs) which diffract light in long-wave-ranges, are attractive for application in advanced optical fields such as photonic crystal devices for light manipulation.[449–452] Due to the periodic modulation of the refractive index between the building nanoparticles and the surrounding medium, PBGs allow only certain light wavelengths to be refracted.[288] CPCs can synchronize optical signals by stop band positions originating from the periodic lattice spacing.[295,296] Conventional microcarriers such as fluorescent dyes or quantum dots,[292,384,453–460] which contain physicochemical carriers as the main spectrum-encoding elements, can show some defects: photobleaching during storage, fluorescent interference between encoding and analyte detection and biotoxicity of the quantum dots.[289,291,293] CPCs, as an optical spectrum-encoding carrier, show characteristic reflection peaks originating from the stop-band. They result in a stable and sensitive detection.[289,461] CPCs convert small physicochemical response signals to a well-defined optical change (stop band positions or structural colors).[291,462–464] CPCs were developed for sensing various external stimuli, such as temperature,[465–469] solvent,[470–473] humidity,[282,474–476] mechanical stress,[477,478] pH,[479,480] ions,[481–483] light[484,485] and electric/magnetic field.[486–491]

To date, only a few conventional approaches exist for the controlled creation of crystals from colloids. Crystal structures formed from colloids in a state of suspense often show fragile behavior. The most predominant approaches for this task are:[156] (1) flow- or evaporation-induced colloidal packing[492–495] and (2) non-close packing induced by electrostatic energy, followed by immobilization.[496,497] CPCs with various morphologies, such as thin film or bulk, were fabricated. The Bragg diffraction that occurs upon irradiation of CPCs generates different structural colors when observed from different angles, useful in the construction of some optical materials and devices that require wider viewing angles.[288] Other drawbacks such as a relatively slow response rate for certain stimuli and the lack of high throughput assays limit their application.[498]

Photonic crystal beads (PCBs) were created to address these drawbacks.[297,498,499] Thanks to their structural symmetry, these spherical CPCs were rotation independent when their surface was irradiated at a fixed incident angle of the light beam.[289,500,501] Crystallization to PCBs was induced by evaporation and polymerization of suspensions with droplet template colloidal nanoparticles.[288] To increase the refractive index, the nanoparticles need to be removed selectively to generate inverse-opal structures with broader PBGs and reduced attenuation length. Characteristic to inverse-opaline PCBs, long-range ordering of pores was crucial to the optical performance, resulting in stable specific reflection peak positions.[286,291] Under normal light incidence, the reflection (stop-band) wavelength λ of PCBs can be estimated using Bragg's equation:[289,296,502]

$$\lambda = 1.633 \times d \times n_{average}$$

where d is the centre-to-centre distance between 2 neighboring pores and $n_{average}$ is the average refractive index. Therefore, by changing the diameters of the pores, a series of PCBs that display the same size with different diffraction-peak positions and structural colors were obtained. To optimize the optical performance of a set of PCBs, the fabrication of the complex structure should be well controlled. Interconnected pores in the PCBs facilitate molecular diffusion into their inner structure and provide more binding sites for probe immobilization. For this reason, careful separation of the templating nanoparticles was critical. Evaporation-induced crystallization required time to ensure complete consolidation, causing almost inevitable cracks in some crystals. Recently, the development of PCBs with inverse-opaline structures has progressed significantly by a combination of microfluidic and templating techniques.[156,288–291,293,295,296,300] Nanoparticles serving as a sacrificial template allow creation of interconnected porous structures, while microfluidic techniques provide PCBs with a highly ordered 3D inverse-opaline structure. PCBs can be applied in displays, multiplex responses and label-free detection.

(1) **Displays.** PCBs were used as building units for reflective display materials, addressing the shortcomings of emissive displays that are poorly visible under bright sunlight. PCBs were assembled into films or used as separated display units.[503,504] Unlike spherical CPC-composed films which showed color variation at different angles, the unit-separated PCBs displayed constant colors (fixed reflection spectra) for a fixed light incident angle regardless of the rotation of the PCB sphere itself (Fig. 70a).[71,288,289,297,298,300,500,501] Kim *et al.*[156] prepared homogeneous PCBs using a microfluidic technique. The reflectance spectra of ETPTA colloidal crystals containing abundant silica nanoparticles depended on the particle size and concentration. After selectively removing the templating silica nanoparticles, the optical features of the obtained inverse-opaline PCBs were different (Fig. 70b). Their PBGs became broader due to the shift in reflectance peaks. By changing the pore diameters and their arrangements, a series of inverse-opaline PCBs with different diffraction peak positions (and thus structural colors) were reported by Zhao *et al.* (Fig. 70c).[289] Cui *et al.*[300] fabricated PIL-IOMs with intrinsic photonic properties, whose PBGs could be widely tuned from 400 to 700 nm. Interestingly, by precisely controlling the etching process, Ye *et al.*[296] obtained PCBs with

This journal is © The Royal Society of Chemistry 2017

Chem. Soc. Rev., 2017, **46**, 855–914 | 891
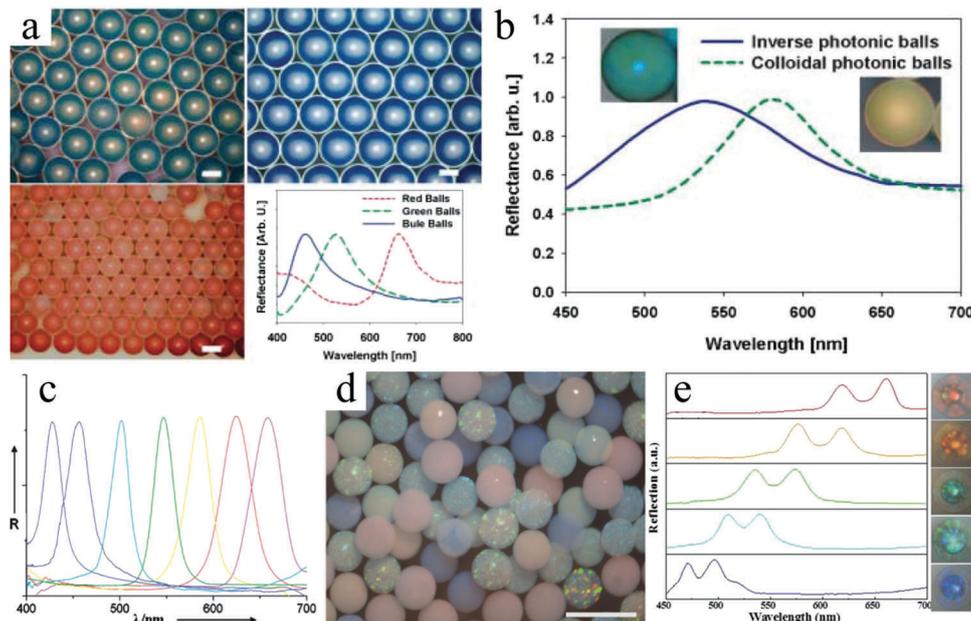
Fig. 70   (a) Reflectance spectra and optical images of red, blue, and green PCBs composed of 190, 152, and 145 nm silica particles. (b) Normalized reflectance spectra and optical images of photonic balls before and after removing the 165 nm silica particles. Reproduced with permission from ref. 156. Copyright 2008 Wiley-VCH. (c) Reflection spectra and (d) 3D image (in water) of 7 inverse-opaline PCBs prepared with polystyrene spheres as sacrificial templates having, from left to right, 200, 215, 238, 262, 280, 298, and 315 nm sizes. Reproduced with permission from ref. 289. Copyright 2009 Wiley-VCH. (e) Reflection spectra of 5 kinds of inverse-opaline PCBs made with silica nanoparticles of, from top to down, 290, 260, 240, 220 and 200 nm sizes. Scale bars are 100 µm (a), 500 µm (d) and 200 µm (e). Reproduced with permission from ref. 296. Copyright 2014 Wiley-VCH.

close-packed opal cores and responsive inverse-opaline hydrogel shells. These exhibited distinct colors as 2 reflection peaks arose due to the different refractive indices of the shell and core (Fig. 70d).

(2) **Multiplex responses.** PCBs were functionalized in different ways to respond to several external stimuli, such as temperature, pH, irradiation, *etc.* However, most of them were limited to sense only one stimulus at once. In contrast, Wang *et al.*[295] generated monodisperse hydrogel photonic crystal microparticles (HPCMs) with 3D porous structures combining a microfluidic and a templating technique, to achieve multi-responsive features. These HPCMs displayed structural color

variation almost covering the entire wavelength of visible light (above 150 nm of the stop band shift) and showed a rapid response (less than 1 min). Thanks to the high sensitivity of PIL in PIL-IOMs,[300] they directly converted these stimuli to readable optical signals, avoiding the quenching and bleaching problems.[505] Fig. 71a displays their exposure to different solvents, showing different stop band shifts. Jeong *et al.*[170] developed novel porous microparticles with reversible membrane permeability, controlled by near-infrared (NIR) irradiation. NIR light can be focused on a small area and penetrate deep into materials without significant damage, thus providing a promising stimulus. Photo- and thermoresponsive switches in the particle surface
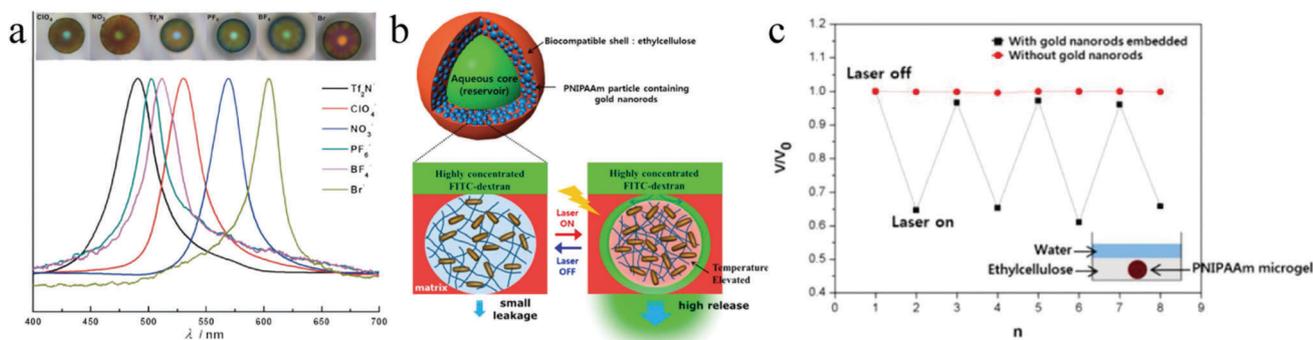
Fig. 71   (a) Optical response and optical images (insets) of PIL-IOMs upon exposure to aqueous solution with 6 different counter ions. Reproduced with permission from ref. 300. Copyright 2014 Wiley-VCH. (b) Illustration of the microparticle structure and the payload release upon irradiation with a NIR laser and (c) normalized volume change of microparticles with (black squares) or without (red dots) gold nanorods according to a cycle laser. Reproduced with permission from ref. 170. Copyright 2014 American Chemical Society.

permeability were observed when gold nanorods were embedded (Fig. 71b). Upon NIR-irradiation the microparticles shrunk and formed macroscopic gaps, permitting large molecules to diffuse inside.[242] After removing the NIR irradiation and cooling of the gold nanorods, the light-triggered permeability disappeared in a reversible manner (Fig. 71c). In contrast, there was no change in the volume of the same microparticles without gold nanorods, regardless of being irradiated or not.

(3) **Label-free multiplex detection.** Detection by labelling targets is still the most popular method, but the labelling process itself is time-consuming, can be expensive and may lead to false negative results.[506–508] Therefore, label-free detection techniques are highly desirable, where target molecules are not labelled but detected in their original forms.[288] More importantly, they also allow for kinetic measurement of interactions between the target and other molecules. PCBs were suggested as promising materials for label-free multiplex detection. They had superior optical properties, which originated from their inverse-opaline structures, such as their change in refractive indices and diffraction plane spacing, detected when shifts in their PBGs or structural colors occurred.[289,291,292,499,509–517] Zhao et al.[291] prepared molecularly imprinted polymer beads (MIPBs) with photonic crystal structures, which not only provided diffraction peaks for encoding, but also converted small physicochemical responses to optical signals.[462–464] Fig. 72a illustrates the change in the MIPBs' diffraction peaks before (dashed lines) and after (solid lines) multiplex detection.

Zhao and co-workers[289] also developed a simple microfluidic device for *in situ* detection (Fig. 72b). When the PCBs passed the detection region, their reflection peaks could be detected using a microscope. More recently, by employing well-controlled wet etching processes, Ye et al.[296] fabricated novel PCBs with close-packed opal cores as their encoding units offering stable diffraction peaks and responsive inverse-opal hydrogel shells. The latter acted as the sensing unit for target recognition, based on the shrinking behavior of the shells. These microparticles showed 2 reflection peaks, whose shifts could be used for the estimation of the target concentration (Fig. 72c).

Currently, the fabrication process of hierarchical porous particles with inverse opal structures is still complicated and apt to have deviation, which further affects their optical applications. One-step microfluidically hierarchical porous particle fabrication has a long way to go.

5.3. Drug release and delivery

Microfluidic methods represent a useful platform for therapeutic agent delivery,[518] as microgels can be fabricated with precise control over particle dimension and its distribution. Over the past few decades, much effort has been devoted to develop μm or nm sized materials for drug-delivery systems (DDSs).[519–523] DDSs aim to deliver the therapeutics in a spatio-temporal controlled manner: loading either hydrophilic or hydrophobic drugs in the desired dose, releasing them at the desired sites and minimizing side effects.[524] Toxic effects can be attributed to premature drug release. Therefore, advanced functional DDSs with remarkable biocompatibility, biodegradability, stability as well as high drug-loading capacity are highly desired. Porous particles have demonstrated their benefits over solid ones as a result of their larger specific surface area for encapsulation and release of substances.[525–531] Further design of their internal structure to create multicompartments made the encapsulation of multiple incompatible components possible, without cross-contamination.[532] The addition of holes on the particle surface allowed the differently sized molecules to migrate through the thin wall in a selective way.[533] DDSs could overcome adverse biopharmaceutical properties of the drugs and improved their bioavailability.[519,522,523]

Recently, porous silicon (PSi) materials were developed as versatile carriers for drug delivery.[523,525,534–538] The degradation rate of PSi materials to non-toxic silicic acid *in vivo* could be controlled by adjusting their porosity and surface chemistry.[531,539–541] Furthermore, a wide variety of therapeutic and imaging agents have been successfully incorporated into PSi particles. However, the existence of free accessible pores imposed the risk of release of drugs from the particles during their transport.[356,541,542] The pores could be sealed by using a matrix to ensure continuous release of the payloads for a prolonged time. In the future, customized ordered and/or hierarchical macroporous particles with regular or irregular shape can be easily obtained by advanced microfluidic technology according to the special requirements. It will accelerate the developments of microfluidically-synthesized macroporous particles in the wider biomedical field.

5.4. Tissue engineering

Tissue engineering was first introduced in the early 1990s[543] to address the shortcomings of traditional tissue repair and
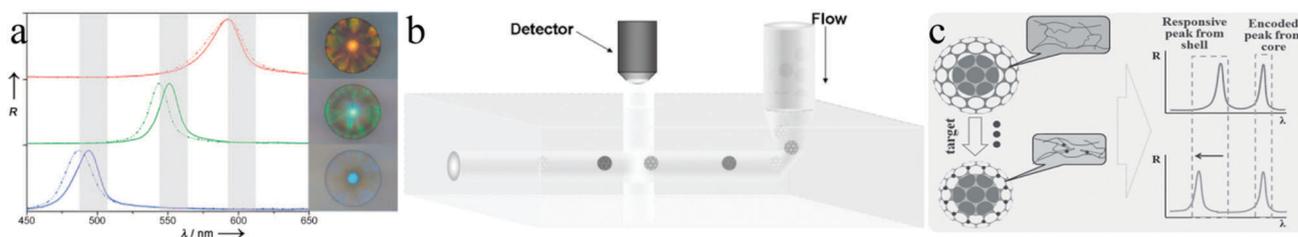
Fig. 72 (a) Reflection spectra and bright field microscopic images of 3 types of MIPBs. The cyan, green and red MIPBs were imprinted bovine haptoglobin (Hb), HRP and serum albumin (BSA), respectively. The dashed and solid lines are spectra of the MIPBs before and after multiplex detection. Reproduced with permission from ref. 291. Copyright 2009 Wiley-VCH. (b) Flow-through microfluidic device used to read reflection spectra of inverse-opaline PCBs. Reproduced with permission from ref. 289. Copyright 2009 Wiley-VCH. (c) Illustration of PCBs for label-free multiplex detection. Reproduced with permission from ref. 296. Copyright 2014 Wiley-VCH.

This journal is © The Royal Society of Chemistry 2017

Chem. Soc. Rev., 2017, **46**, 855–914 | 893

transplantation, as an interdisciplinary approach between biology, materials science, medicine, and engineering. It aims at the successful transplantation of a bio-factor, such as cells, genes and proteins, within porous degradable materials, known as scaffolds.[267,544–546] The use of 3D scaffolds in tissue engineering entailed precise control over the pore size and the interconnects between them, because these in turn determined the void space available for cell seeding.[547,548] The interconnected pores provided proper exchange of nutrients and metabolic waste, and acted as a protective barrier for the cells to the immune system.[175] The mechanical properties were also critical. Macroporous materials with interconnected morphology were suitable for tissue engineering.[273,549–552] PolyHIPEs, a class of porous and permeable materials, were customized to serve as scaffolds.[273] Various macroporous polyHIPE porous materials, based on both synthetic as well as natural polymers, were studied for their application in tissue engineering,[553–559] whereas conventional polyHIPEs based on the action of shearing showed important shortcomings. First, the dimension of pores in these materials is below 100 μm, which is too small for cells to colonize, especially because the seeded cells often proliferated only at the outer surface rather than penetrating inside the materials.[560] Secondly, both pores and interconnects were typically highly polydisperse resulting in lower performance of the material. Cells grown within such scaffolds may lead to undesired phenotypic diversity and inhomogeneous distribution. In contrast, computer-aided microfabrication techniques such as photolithographic patterning and layering, and direct writing and two-photon stereo-lithography, may provide the materials with the desired pore size and 3D interconnectivity, but these approaches are usually costly.[268,269,561] Recently, a microfluidic technique was incorporated into the HIPE technique to overcome the morphological limitations of the conventional approaches.[19] The microfluidic technique generated sets of droplets with equal dimensions in a highly ordered manner without any specific chemical process. This way, both hydrophilic and hydrophobic 3D porous scaffolds could be fabricated for tissue engineering applications. The study and application of microfluidically-synthesized macroporous particles as 3D porous scaffolds for tissue engineering are still insufficient. But, with the fast improvement of microfluidic-based fabrication, we believe microfluidically-synthesized macroporous particles will usher a better future in tissue engineering.

5.5. Water treatment

Common wastewater treatments of streams from improper operation or accidental leakage during production, storage, transportation and usage of chemical products harmful to the environment are often based on chemical, physical and/or biological methods.[562–564] However, operations such as emulsification, solidification and photocatalytic degradation require special conditions and can generate toxic by-products.[565] Bioremediation methods may cause unnecessary secondary pollution from residual nutrients and microbial pollution.[566] Most of the treatments of oil contaminated wastewater are merely

physical methods. Adsorption is more suitable for rather small amounts of organic pollutants. Adsorption not only removes the pollutants, but also makes the recycling of materials possible. The most common adsorbing materials include polymers, carbon materials, natural minerals and biomaterials.[567–570] The ideal oil–water separation adsorption materials should be: (1) enriched with alkyl groups, which selectively adsorb and efficiently separate the oily substances from the water and form strong molecular interatomic forces, (2) present a rich porous structure, high specific surface area and pore volume contributing to a high uptake capacity and (3) have excellent recyclability.[571,572]

Removal of organic pollutants from surface or sub-surface aquifer water to reduce the ecological damage in the environment is a difficult task. The innovation of materials, especially porous particles, plays an important role in this area.[563,573,574] To date, silica aerogels and activated carbons have been among the most common materials used for this task. However, with time these particles become unstable in such aqueous environments due to their inherent hydrophobic surface nature and eventually they need to be replaced.[575–577] To achieve good water dispersion of hydrophobic particles, their surface morphology characteristics should be changed. Particles can absorb organic contaminants and remain well dispersed in aqueous environments by constructing a porous hydrophobic absorbing core and a hydrophilic surface. By combining mixing-induced phase separation and precipitation polymerization in a microfluidic device, particles with a hydrophobic porous core and a hydrophilic porous surface were designed to ensure excellent dispersion of particles in the aqueous phase with good adsorption capacity[578] (Fig. 73a). Multilayered porous particles were obtained after removal of the porogen, assisted with a color change from dark to light (Fig. 73b), ultimately becoming transparent. The particles were effective for the uptake of organic oil directly from oil drops as for the uptake of organic molecules dissolved in an aqueous solution. The recyclability of these particles was also demonstrated.

In addition to porous materials with only one pore dimension, recently Zhang et al.[351] introduced highly interconnected hierarchical porous microparticles for the adsorption of oil droplets in water. Magnetic Fe_3O_4 nanoparticles (diameter 12 nm) were prepared and then dispersed by ultrasonic treatment in the middle phase to generate the magnetic hierarchical porous poly(MMA-co-EGDMA) microparticles. Similar to their previous work,[533] first EGDMA dyed with red color was added into water (Fig. 74a) and then dispersed into microdroplets by shaking (Fig. 74b), serving as an oil contaminated sample. For the removal of the oil, the poly(MMA-co-EGDMA) porous microparticles were added and adequately mixed (Fig. 74c). Remarkably, the dyed oil droplets could be separated from the microparticles by directed guiding with a magnet (Fig. 74d). The microparticles were recovered by washing the absorbed oil with ethanol and recycled up to 20 times without structural deformation (Fig. 74e). The results were compared with those obtained with poly(MMA-co-EGDMA-co-GMA) to study the effect of nanopores and different hierarchical porous structures (Table 6).

The ever-increasing requirement for wastewater treatment and reuse gradually pushes conventional porous adsorbents to their

894 | Chem. Soc. Rev., 2017, **46**, 855–914

This journal is © The Royal Society of Chemistry 2017

Fig. 73 (a) Schematic illustration of the porous particle fabrication. (b) The optical images describing the process absorption of oil by particles and consequent increase of inner layer brightness during 48 h time period. Reproduced with permission from ref. 578. Copyright 2013 Wiley-VCH.

Table 6 The effect of different hierarchical porous structures of poly(MMA-co-EGDMA-co-GMA) microparticles on the oil adsorption capacity

Structure type	Average pore size (μm)	Porosity (%)	Oil adsorption capacity (μL)
1 pore type (μm)	±120	44	<10
1 pore type (nm)	±0.58	48	±20
2 pore types (μm)	—	—	±30
3 pore types (μm)	—	—	±40

this research field, especially because they are simple to handle, are operated under mild conditions and have high efficiency.[579,580] In a continuous flow, magnetic particles were deflected from the previous flow direction by applying an external magnetic field. Thus, they could be separated from each other and from non-magnetic materials. However, the separation performance relied on their magnetic susceptibility and size, the strength of the applied magnetic field and the applied flow rate. To simplify bio-separations, magnetic properties could be added to porous particles by embedding superparamagnetic iron oxide nano-particles with the aid of microfluidic techniques.[106,224,225] Moreover, by synchronization with other reaction or analysis devices, this separation method can be used to form an integrated micro-analysis system.

5.7. Particle sensors – encoded particles

One of the most attractive applications of the complex particles fabricated by flow lithography within microfluidic devices is high-throughput particle diagnostics and sensing.[581–584] The major challenge in multiplexing is to provide particles with unique and easily readable codes in a large amount. SFL was used to fabricate such particles, having one part with a unique square macroporous pattern, while the other part contained a probe molecule with unique signature.[384,585] These particles served as probes to detect molecular targets present in an aqueous solution of unknown composition, similar to DNA base-pairing. By conducting the particles with their unique barcode through a detector they could be decoded and reveal (quantitative) target information (Fig. 75).[586]

The advantage over other systems is that the probes were effectively printed directly into the encoded particles and only one fluorescent molecule was needed for both target identification and quantification. The technique succeeded in detecting DNA oligomer targets down to the picomolar level. Recently, other researchers designed special shaped particles obtained by CFL for the detection of some proteins. They were also used for

limits. The solutions to the existing and future water challenges will depend on advanced adsorbents with unprecedented performances, such as higher specific surface area, distinguished hierarchical porous morphology, outstanding selective adsorption capacity, as well as less toxicity and acceptable mechanical properties. However, the current shortcomings of the microfluidic technique, for example, low yield and high cost, become another obstacle in the application of microfluidically-synthesized porous materials in water purification. Design and use of microfluidically-synthesized porous materials to solve these challenges become some of the most urgent problems in the future.

5.6. Bio-separation

In the field of biology, to study the interactions such as those between antibodies and antigens, or between receptors and cells, a series of sequential post-processing, such as separation, washing and purification, is required. The development of bio-magnetic porous particles has been shown to be successful in

Fig. 74 Magnetic hierarchical porous poly(MMA-co-EGDMA) microparticles for magnetic-guided removal of dyed EGDMA microdroplets from water. Reproduced with permission from ref. 351. Copyright 2015 American Chemical Society.

This journal is © The Royal Society of Chemistry 2017

Chem. Soc. Rev., 2017, 46, 855–914 | 895
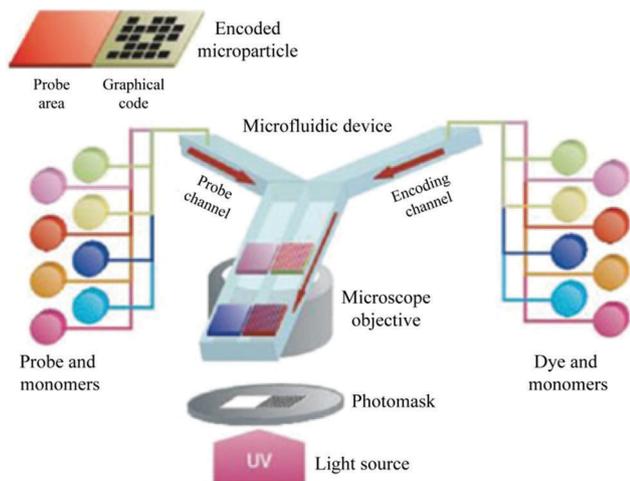
Fig. 75 Encoded particles used for high throughput multiplex nucleotide diagnostics. Reproduced with permission from ref. 586. Copyright 2006 Macmillan Publishers.

the specific spatial sensing of ligands through development of polymeric substrates that contain a specific templating ligand: molecularly imprinted polymers emerging as a novel research area. With the help of microfluidic techniques the template was selectively removed from residual cavities and then the mono-disperse MIP microbeads were used to detect the specific ligand molecule target,[587] even in mixtures of various molecule analogs.[588] With the rapid development and lasting improvement of encoded particles, we will witness the widespread use of microfluidically-synthesized encoded particles with faster response and improved accuracy in the future.

5.8. Multiplex protein measurement

Two main methods exist for measuring protein panels in a single assay: planar arrays and particle-based arrays.[589] Planar arrays, also denominated micro-arrays, employ fixed panels of 100–1000 unique probes spatially segregated on a slide for a single assay. Although this method can measure multiplexed proteins on large scale, it provides limited flexibility for probe-set modification, due to the requirement of large quantities of reagents and because the detection can be expensive and time consuming.[590,591] In contrast, particle-based arrays have some advantages over conventional planar arrays, such as improved scalability, shorter analysis time, and flexible probe set reconstruction (important to 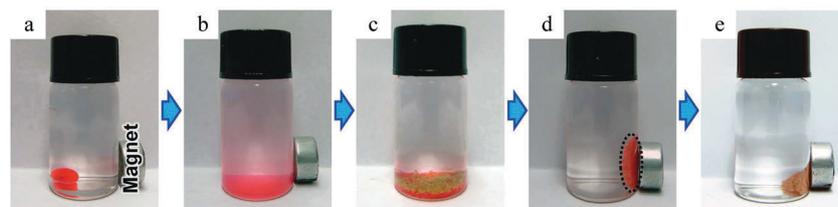respond to evolving assay demands). Moreover, it requires less sample and reagents to analyze 100–1000 targets and it can combine different encoded particles, each identifying a single target, as a custom chip for tailored assays. They are particularly suitable for high throughput analysis of focused panels of biomolecules.[381] However, recently, the low accuracy and high cost of microfluidic-synthesized particles for multiplex protein measurement have attracted more and more attention. We believe that customized particles obtained by an advanced microfluidic flow photolithography method will overcome these drawbacks, exhibit huge potential and make better accomplishment in future multiplex protein measurement.

6. Conclusion and outlook

This review is intended to introduce microfluidics in an ordered comprehensive way and to inspire the researchers for the fabrication of functional macroporous particles. In addition, a section for current and future application fields is foreseen, with the focus on particle morphology design as a function of the application requirements. Currently exciting developments are published in the field of fabrication, functionalization and application of macroporous materials. In particular, micro-manufacturing and micro-machining contribute more and more to the creation of hierarchical porous materials, made from various compounds and composites. Hierarchical ordered structures inherently differ from monomodal ones by the co-existence of multiple pore scales. The embedded micropores and mesopores offer a higher surface area and pore volume, resulting in numerous reactive sites, size-selectivity for different kinds of molecules and a substantial higher interfacial area. When larger macropores can be incorporated, without collapsing the micro- and mesoporous structures, the resultant hierarchical porous materials can offset the diffusion limitations and improve the mass and energy exchange.[592]

The fabrication of porous materials using microfluidic techniques addresses the drawbacks of traditional synthesis approaches. It provides accurate control of the particles' morphology in a highly reproductive manner. Microfluidic techniques also allow the space for further development with more complex configurations: from radially porous particles to ordered ones, from opened porous structures to closed ones, from regular porous spheres to irregular ones, from interconnected structures to multi-compartmentalized structures, from monomodal porous structures to hierarchical ones, *etc.* They have opened the way to the production of advanced materials such as inverse-opals, scaffolds and hierarchical porous materials, which would be difficult to generate otherwise. Flow lithography, as the result of simultaneous development of microfluidics and photolithography techniques, unlocks new possibilities for the synthesis of customized porous materials with a relatively wide range of morphologies and thus application fields. Microfluidic techniques allow particles to be fabricated with unprecedented control over their pore size with narrow distributions. They possess great potential for encapsulating a wide range of active materials, even living cells in biomedical applications. Nevertheless some drawbacks still exist, such as low throughput and tedious device preparation, limiting their wider range of applications. But this can be stated in many novel techniques and the research field is still developing. In this regard, multiple parallel microfluidic devices are currently considered as a practical but less efficient solution.[593,594] Blocking phenomena occurring during fabrication still remain a challenge for microfluidic techniques. The existing methods for the minimization of blocking phenomena, such as surface modification, flow modulation and external force control, are rather sophisticated. A facile approach for minimizing this effect is still required.[70] To date, one-step fabrication of macroporous particles has only rendered radially porous structures, whereas a combination of polymerization with sacrificial templates and wet etching processes results in various well ordered porous structures. Hierarchical porous structures are obtained by introducing sacrificial templating

896 | Chem. Soc. Rev., 2017, 46, 855–914

This journal is © The Royal Society of Chemistry 2017

nanoparticles on different scales. However, modern microfluidics still looks for improvements. The main quest still remains how to simultaneously achieve accurate and independent control of the ordered hierarchical porous structures in one step.

In conclusion, future research will focus on the improvement of the device simplicity on one hand and on the particle morphology functional complexity on the other hand. This change undoubtedly conforms to the development of science from simple to complicated as well as from the shallower to the deeper. While initial inroads have been made, more work in the area of scale-up must still be done.

List of abbreviations

2D	Two-dimensional
3D	Three-dimensional
AAm	Acrylamide
AIBN	Azobis(isobutyronitrile)
AR	Aspect ratio
BDK	2,2-Dimethoxy-2-phenylacetophenone
BMA	Butyl methacrylate
BuAc	n-Butyl acetate
ccp	Cubic close packed
CFL	Continuous flow lithography
CPC	Colloidal photonic crystal
CTAB	Cetyltrimethylammonium
DAP	Diallyl phthalate
Darocur 1173	2-Hydroxy-2-methyl-1-phenyl-1-propanone
DBP	Diisobutyl phthalate
DCDMS	Dichlorodimethylsilane
DCM	Dichloromethane
DDP	Diisodecyl phthalate
DDS	Drug-delivery system
DEAP	2,2-Diethoxyacetophenone
DEP	Diethyl phthalate
DMF	N,N-Dimethylformamide
DMPA	2,2-Dimethoxy-2-phenylacetophenone
DOP	Dioctyl phthalate
DPPD	2,2-Di(pro-2-ynyl)-propane-1,3-diol
DEX-MA	Dextran-methacrylate
EA	Ethyl acetate
EGDMA	Ethylene glycol dimethacrylate
EPTBC	Ethyleneoxide propyleneoxide tri-block copolymer
ETPTA	Ethoxylated trimethylolpropane triacrylate
FFD	Flow-focusing device
FFT	T-junction device
FITC-dextran	Fluorescein isothiocyanate-dextran
GLU	Glutaraldehyde
GMA	Glycidyl methacrylate
GMBS	N-Gamma-maleimido-butyryloxy-succinimide
HEM	Hydroxyethyl methacrylate
HF	Hydrofluoric acid
HIPE	High-internal-phase emulsion
HMPP	2-Hydroxy-2-methyl-1-phenyl-1-propanone

HPCM	Hydrogel photonic crystal microparticles
HRP	Horseradish peroxidase
KPS	Potassium persulfate
LRL	Lock and release lithography
MAA	Methacrylic acid
MBAAm	N,N'-Methylene-bis-acrylamide
MEK	Methyl ethyl ketone
MIPB	Molecularly imprinted polymer bead
MMA	Methyl methacrylate
NIR	Near-infrared
NOA 61	Mixture of trimethylolpropane diallyl ether, isophorone diisocyanate ester, trimethylolpropane tristhiol and a benzophenone photo-initiator
OY	1,7-Octadiyne
NIPAm	N-Isopropylacrylamide
PBG	Photonic band gap
PCB	Photonic crystal bead
PCL	Poly(ε-caprolactone)
PCM	Phase change material
PDLA	Poly(D,L-lactide)
PDMS	Poly(dimethyl siloxane)
PEG	Poly(ethylene glycol)
PEG-40S	Poly(ethylene glycol)-40-stearate
PEGDA	Poly(ethylene glycol)diacrylate
PEO	Poly(ethylene oxide)
PGPR	Polyglycerol polyricinoleate
PhC	Photonic crystal
PIL	Polyionic liquid
PIL-IOM	Polyionic liquid inverse opaline microspheres
PLGA	Poly(D,L-lactide-co-glycolide)
PLLA	Poly(L-lactide)
Pluronic F108	Ethylene oxide–propylene oxide–ethylene oxide tri-block copolymer
PMMA	Poly(methyl methacrylate)
pNIPAAm	Poly(N-isopropylacrylamide)
PPO	Poly(propylene oxide)
PSf	Polysulfone
PTE	Pentaerythritol triallyl ether
PVA	Poly(vinyl alcohol)
SCCB	Silica colloidal crystal bead
SDS	Sodium dodecyl sulfate
SERS	Surface-enhanced Raman scattering
SFIL	Stop flow interference lithography
SFL	Stop flow lithography
Span80	Sorbitan mono-oleate
SPIONs	Superparamagnetic iron oxide nanoparticles
SPS	Sodium peroxodisulfate
SR454	Ethoxylated-trimethylolpropane-triacrylate
TEMED	N,N,N',N'-Tetramethylethylenediamine
TEOS	Tetraethyl orthosilicate
THF	Tetrahydrofuran
TPGDA	Tripropylene glycol diacrylate
TT	Pentaerythritol tetrakis-(3-mercaptopropionate)
TTT	Triallyl-135 triazine trione

Appendix

| Morphology | | Sb/group ref. | Method | Phase composition | | $Q_d:Q_c$ or $Q_i:Q_M:Q_O$ | Porogen | Average particle diameter/μm | Average pore size/μm | | Porosity | Specific surface area (SSA)/m² g⁻¹ | CV (%) |
Surface	Internal			Inner (dispersed)	Outer (continuous)				Surface	Internal			
Smooth skin	Macropores	S. Dubinsky et al.	UV-induced polymerization with porogen	A mixture of GMA and porogen	Aqueous solution of PVA and surfactant or THF	1:200	DBP/DOP 1:1 (v/v)	About 58^a	0	—	—	—	—
							DOP (0.5 wt% Triton X-100)	About 63.5^a	0	—	—	—	—
	Gradient porous structures	T. Watanabe et al.	Selective solvent extraction	Sodium poly(styrenesulfonate)	Hexadecane and Span80	1:15–1:35	—	About 79^a	0	10–100	10–50%	—	<5
	Macropores	J. Y. Sim et al.	Microfluidic molding	—	—	—	—	—	0	0.166–0.2	—	—	—
	Micro- to macropores	C. E. Udoh et al.	Selective solvent extraction	Polymer solution	Hexadecane with Span80	Q_d = 10 μL min⁻¹; Q_c = 50–90 μL min⁻¹	—	50–200	0	1–100	—	—	—
Golf-ball-like dimples	Macropores	S.-H. Kim et al.	UV-induced polymerization with wet etching process	Silica–ETPTA and Darocur 1173	Aqueous solution with Pluronic F108	1:100	—	About 110^a About 197^a	0.14–0.21^a 0.59–1.18^a	—	—	—	—
	Macropores	K.-H. Hwangbo et al.	Selective solvent extraction	A mixture of DCM, polymer, and PCM	PVA aqueous solution	<1:500	—	185–280	5–20^a	4.4–9.5^a	—	—	—
	Macropores	J. H. Lee et al.	Solvent evaporation and phase separation	A mixture of PLGA, PCM, dichloromethane solution	PVA aqueous solution	—	—	About 235 ± 5	4.2–33.2^a	Smaller than surface dimples	—	—	—

898 | Chem. Soc. Rev., 2017, 46, 855–914

This journal is © The Royal Society of Chemistry 2017

Morphology	Sb/group ref.	Method	Phase composition			$Q_d:Q_c$ or $Q_1:Q_M:Q_O$	Porogen	Average particle diameter/ μm	Average pore size/ μm	Porosity	Specific surface area (SSA)/ m² g⁻¹	CV (%)
			Inner (dispersed)	Middle (dispersed)	Outer (continuous)							
Opened macroporous spheres	J. X. Yun et al.	Cryo-polymerization	A mixture of MBAAm, TEMED, AAm, APS	—	Ethyl enanthate and Span 80	1:12–1:2	—	800–1500	3–50	86.2%	—	—
	S. Dubinsky et al.	UV-induced polymerization with porogen	A mixture of GMA, DMPA, EGDMA, porogen	—	PVA aqueous solution	2:105 2:105 1:15 1:12	DEP DBP DOP DDP	75 74 110 131	0.033ᵃ 0.107ᵃ 0.179ᵃ 0.250ᵃ	—	28.7 13.9 6.6 3.4	1.0 2.9 0.8 2.7
	S.-H. Kim et al.	UV-induced polymerization with wet etching process	Silica-ETPTA and Darocur 1173	—	Aqueous solution with Pluronic F108, BASF, EPTBC	1:100	—	About 247.4ᵃ	About 0.15ᵃ	—	—	—
	W. J. Duncanson et al.	One step polymerization with porogen	DCM and PLA	—	PVA aqueous solution	—	Self-assembling perfluorinated-dendrimer-dye complex	About 45–60ᵃ	About 0.9–1.25ᵃ	—	—	<6
	K. Jiang et al.	UV-induced polymerization with porogen	A mixture of GMA, SR454, DA, DMPA	—	PVA aqueous solution with Triton X-100	1:15	DA	About 77 ± 2	1.6 ± 0.6	44–50%	—	—
	H. Zhang et al.	Single emulsion template with porogen	A mixture of HEMA, MMA, BDK, PVP K30, PGPR, EGPDA	—	PVA aqueous solution with glycerol	3:20	PVP K30	47.6–57.5	About 1.1–2.5ᵃ	—	—	3.5
	M. T. Gokmen et al.	UV-induced polymerization of HIPE emulsion template	A mixture of EGDMA, GMA, PEO–PPO–PEO 2800, CaCl₂·2H₂O (HIPE)	—	PVA aqueous solution	1:6	—	About 400	About 15	78–87%	16	—
	J. B. Wacker et al.	Evaporation-induced consolidation and self-assembly	Silica colloid aqueous solution	—	Oleic acid	1:100–1:5	—	About 13–130ᵃ	About 0.8ᵃ	—	—	—
	J. Wan et al.	UV-induced polymerization of three phase emulsion template	Pure nitrogen gas	Deionized water with SDS, DEAP, MBAAm, acylamide	Mineral oil with DEAP	$Q_w:Q_o = 1$; P = 18 psi	—	<210ᵃ	About 28ᵃ	—	—	—
	R. A. Prasath et al.	UV-induced polymerization and flow reaction	Thiol-ene monomers with π-bond, DMPA, porogen Thiol-yne monomers with π-bond, DMPA, porogen	—	SDS aqueous solution	1:900– 1:200	DOP, Xy, BuAc, a mixture of Xy and BuAc	240–325 240–300	0.05–3 0.2–1	—	0–4.9 2.2–35.6	— —

This journal is © The Royal Society of Chemistry 2017

Chem. Soc. Rev., 2017, 46, 855–914 | 899

Table (continued)

Morphology	Sb/group ref.	Method	Phase composition			$Q_d:Q_c$ or $Q_i:Q_M:Q_o$	Porogen	Average particle diameter/ μm	Average pore size/ μm	Porosity	Specific surface area (SSA)/ m² g⁻¹	CV (%)
			Inner (dispersed)	Middle (dispersed)	Outer (continuous)							
Macroporous core–shell spheres	W.-C. Jeong et al.	Double emulsion template	PVA aqueous solution with FITC-dextran	pNIPAAm particle-dispersed mixture of DCM, hexane and ethyl cellulose	PVA aqueous solution	3:7:60	—	About 455ᵃ	Sub- to a few micrometers	—	—	—
	X. Gong et al.	UV-induced polymerization and flow reaction	H₂O₂ solution with PVA	NOA 61 / TPGDA / EGDMA	Liquid paraffin / Silicon oil / Silicon oil	3:6:4- 1:2:4	—	About 50–200	Several micrometers to tens of micrometers	70% (max)	—	—
	S.-W. Choi et al.	Double emulsion template and fast solvent evaporation	PVA aqueous solution	A mixture of PLGA and DCM	PVA aqueous solution	3:30:200	—	About 709.1	About 1.5	—	—	1.7
Dense spheres with thin surface pores / Opened macroporous spheres / Dense porous spheres / More dense channel-like structure	C. Paquet et al.	Self-assembling of materials	Chloroform solvent with SPIONs and copolymer / Toluene solvent with SPIONs and copolymer / A mixture of THF and toluene with SPIONs and copolymer / Hexane solvent with SPIONs and copolymer		PVA aqueous solution with glycerol	1:400	—	About 113–131	<1	—	About 5.2	2–8
Macroporous rods	M. T. Gokmen et al.	UV-induced polymerization of HIPE emulsion template	A mixture of EGDMA, GMA, PEO–PPO–PEO 4400, CaCl₂;2H₂O (HIPE)		PVA aqueous solution	4:75	—	About 200	About 1.25ᵃ	—	—	—
	J. B. Wacker et al.	Evaporation-induced consolidation and self-assembly	Silica colloid aqueous solution		Oleic acid	1:100- 1:5	—	About 45—100ᵃ	About 0.8ᵃ	—	—	—
Sponge-like open-celled porous microgels (inter-connected pores)	C.-L. Mou et al.	UV-induced polymerization and homo-geneous emulsification	O/W emulsions with benzyl benzoate, soybean oil, PGPR, LR300, V-50, NIPAM, MBAAm, F-127, and glycerol		Soybean oil with PGPR	1:12-1:1	Fine oil droplets (adding isopropanol or heat up)	—	About 8ᵃ	—	—	1.6
Pinecone-like structure at one end and a tip-shaped tail structure at another end (disconnected pores)			Deionized water with NIPAM, MBAAm, V-50, F-127 and glycerol				(Adding isopropanol)	—	—	—	—	1.8

900 | Chem. Soc. Rev., 2017, 46, 855–914

This journal is © The Royal Society of Chemistry 2017

Morphology	Sb/group ref.	Method	Phase composition		$Q_d:Q_c$ or $Q_i:Q_M:Q_O$	Porogen	Average swelling ratio	Average pore size/μm	Porosity	Specific surface area (SSA)/m² g⁻¹	CV (%)
			Inner (dispersed)	Outer (continuous)							
Highly interconnected and uniform macroporous scaffold	K. Chung et al.	Single emulsion templates	Nitrogen gas	Alginate solution with Pluronic F127	$P = 6$ psi; $Q_c = 18$ mL h⁻¹	—	91.83 ± 6.02%	About 250	86.90 ± 5.09%	—	—
	C.-C. Wang et al.	Single emulsion templates	Nitrogen gas	Alginate solution with acetic acid and Pluronic F127	$P = 5$ psi; $Q_c = 12$ mL h⁻¹	—	2607.41 ± 340.10%	About 225ᵃ	97.25 ± 0.84%	—	—
	A. van der Net et al.	Microfluidic foaming technique	Air	Solution A (AAm aqueous solution with MBAAm, TEMED, Lutesol® AT18) + solution B (an aqueous solution with Lutesol® AT18 and SPS)	1:1 ($Q_A = Q_B$)	—	—	About 207–353ᵃ	—	—	—
	C. Colosi et al.	Microfluidic foaming technique	Argon gas	An aqueous solution of PVA and CTABr	$P = 67$ kPa, $Q_c = 0.135$ mL h⁻¹	—	—	140 ± 17	63%	—	—
	M. Constantini et al.	Microfluidic polyHIPEs emulsions	A cyclohexane solution	An aqueous solution of DEX-MA with Irgacure 2959, APS, Pluronic F-68	About 4:1	—	—	About 136–241	About 80%	—	—
Highly order closed-cell polyhedral foam and closed-cell polyhedral foam	A. Quell et al.	Microfluidic polyHIPE emulsions	PolyHIPE monomers with KPS or AIBN	A mixture solution of styrene and divinylbenzene containing the surfactant Hypermer 2296	—	—	—	59–71 (KPS) or 57–75 (AIBN)	—	—	—

Morphology	Sb/group ref.	Method	Phase composition		$Q_d:Q_c$ or $Q_i:Q_M:Q_O$	Porogen	Average particle diameter/μm	Average pore size/μm	Porosity	Specific surface area (SSA)/m² g⁻¹	CV (%)
			Inner (dispersed)	Outer (continuous)							
Highly ordered inverse opal structure	Y. Zhao et al.	Sacrificial template self-assembly, evaporation-induced consolidation and calcination	An aqueous suspension containing monodisperse polystyrene spheres and ultrafine silica particles	Silicon oil	—	—	About 270ᵃ	About 0.2ᵃ	—	—	—
	J. Wang et al.	Sacrificial template self-assembly, evaporation-induced consolidation and wet etching process	An aqueous suspension containing monodisperse silica NPs	Silicon oil	1:6	—	—	About 0.22ᵇ	—	—	—
	J. Cui et al.	Sacrificial template self-assembly, UV-induced polymerization and wet etching process	—	—	—	—	0.3	About 0.2ᵃ	—	—	—
Densely packed opal cores and inverse-opal shells	B. Ye et al.	Sacrificial template self-assembly, UV-induced polymerization and selected etching process	—	—	—	—	—	About 0.2ᵃ	—	—	—
Highly ordered macroporous film	M. Elsayed et al.	Sacrificial template (efficient burst of templated bubbles)	Polymeric solution containing sodium alginate, PEG-40S and phospholipids	Gas	$P = 95–165$ kPa, $Q_c = 200$ μL min⁻¹	—	—	70 ± 30 μm to 122 ± 15 μm	—	—	—

This journal is © The Royal Society of Chemistry 2017

Chem. Soc. Rev., 2017, 46, 855–914 | 901

Morphology	Sb/group ref.	Method	Phase composition			$Q_d:Q_c$ or $Q_i:Q_M:Q_O$	Porogen	Average particle size/μm	Average pore size/μm		Porosity	Specific surface area (SSA)/m² g⁻¹	CV (%)
			Inner (dispersed)	Middle (dispersed)	Outer (continuous)				Large	Small			
Microspheres with hollow interior and radially hierarchical porous shell	S.-W. Choi et al.	Double emulsions template and fast solvent evaporation	PVA aqueous solution	A homogenized W/O emulsion containing PVA and PLGA	PVA aqueous solution	0.7:6:50	—	About 446	About 4	<1	—	—	—
Microspheres with bimodal macropore-mesopore structure (radially hierarchical)	Z. Zhai et al.	Temperature-induced gelation	A silica sol aqueous solution containing MC, PEG, HCL and TEOS	—	A liquid paraffin solution containing Span 85	1:40	—	About 490	About 0.1–1	About 0.0138–0.0205	—	About 309–390	2.1–2.5
Multi-cored microcapsules with porous surface (radially hierarchical)	S.-H. Kim	Double emulsion template, UV-induced polymerization and wet etching process	An aqueous solution of food coloring pigments or FITC-labeled dextran	A ETPTA suspension containing silica particles treated with DCDMS	An aqueous solution of ethyleneoxide–propylene oxide–ethylene oxide tri-block copolymer, BASF and Pluronic F2109	$Q_M:Q_I$ < 0.5	—	About 200–300[a]	About 100[b]	About 0.7[a]	—	—	—
Radially hierarchical interconnected porous spheres	N. J. Carroll et al.	Microfluidic templating and evaporation-induced consolidation	An aqueous solution with CTAB, TEOS, and HCl	Pure hexadecane oil	Hexadecane solution with ABIL EM 90	$Q_M:Q_I$ = 1:10	—	7.7 ± 1	Tens of nanometers	Single nanometer	—	About 650–1250	—
Radially hierarchical porous microspheres	Y. Fan et al.	The synergistic effect between the sol–gel process and solvent extraction in droplets	Dichloromethane solution with PCL and TEOS	—	Mixture of PVA and ammonia solution	—	—	About 65	7.5[a]	—	—	333.698	—
Chitosan inverse opal scaffold with ordered hierarchical pores	S.-W. Choi et al.	Sacrificial template, heat treatment and sedimentation-evaporation method	A PCL solution in MC	—	PVA aqueous solution	—	—	4.5 mm in diameter and 1.5 mm in thickness	About 110[a]	About 5[a]	—	—	<5
Uniform microparticles with controllable highly interconnected hierarchical porous structures	M.-J. Zhang et al.	Double emulsion template and mass transfer	An aqueous solution containing glycerin and Pluronic F127	MMA containing EGDMA, PGPR, and HMPP	An aqueous solution containing glycerin and Pluronic F127	—	—	About 217[a]	About 130–167[a]	About 2[a]	0–50%	—	—
Hierarchical porous silk-based materials	M. R. Sommer et al.	Sacrificial template and 3D printing technology	DCM solution with PCL	—	PVA aqueous solution	Q_d = 1–5 mL h⁻¹; Q_c = 5–30 mL h⁻¹	—	—	<335[b]	—	—	—	—

[a] Measure (obtained by analyzing/measuring optical microscopy images/SEM). [b] Speculation.

Acknowledgements

References

1 H. P. Hentze and M. Antonietti, *Rev. Mol. Biotechnol.*, 2002, **90**, 27–53.

2 S. Xie, R. W. Allington, J. M. J. Fréchet and F. Svec, in *Modern Advances in Chromatography*, ed. R. Freitag, Springer, Berlin, Heidelberg, 2002, pp. 87–125.

3 Y. Lumelsky, J. Zoldan, S. Levenberg and M. S. Silverstein, *Macromolecules*, 2008, **41**, 1469–1474.

4 F. S. Macintyre and D. C. Sherrington, *Macromolecules*, 2004, **37**, 7628–7636.

5 M. Slater, M. Snauko, F. Svec and J. M. J. Fréchet, *Anal. Chem.*, 2006, **78**, 4969–4975.

6 N. Fontanals, R. M. Marcé, P. A. G. Cormack, D. C. Sherrington and F. Borrull, *J. Chromatogr. A*, 2008, **1191**, 118–124.

7 D. Hudson, *J. Comb. Chem.*, 1999, **1**, 333–360.

8 T. P. Rao, R. S. Praveen and S. Daniel, *Crit. Rev. Anal. Chem.*, 2004, **34**, 177–193.

9 L. Leeb, P. Gmeiner and S. Löber, *QSAR Comb. Sci.*, 2007, **26**, 1145–1150.

10 N. Miletić, Z. Vuković, A. Nastasović and K. Loos, *J. Mol. Catal. B: Enzym.*, 2009, **56**, 196–201.

11 R. Haag and S. Roller, in *Immobilized Catalysts: Solid Phases, Immobilization and Applications*, ed. A. Kirschning, Springer, Berlin, Heidelberg, 2004, pp. 1–42.

12 F. Švec, J. Hradil, J. Čoupek and J. Kálal, *Angew. Makromol. Chem.*, 1975, **48**, 135–143.

13 Z. Pelzbauer, J. Lukáš, F. Švec and J. Kálal, *J. Chromatogr. A*, 1979, **171**, 101–107.

14 D. Horák, Z. Pelzbauer, M. Bleha, M. Ilavský, F. Švec and J. Kálal, *J. Appl. Polym. Sci.*, 1981, **26**, 411–421.

15 W. T. Ford, J. Lee and M. Tomoi, *Macromolecules*, 1982, **15**, 1246–1251.

16 P. Reinholdsson, T. Hargitai, R. Isaksson and B. Törnell, *Angew. Makromol. Chem.*, 1991, **192**, 113–132.

17 S. Dubinsky, J. I. Park, I. Gourevich, C. Chan, M. Deetz and E. Kumacheva, *Macromolecules*, 2009, **42**, 1990–1994.

18 H. Zhang, X.-J. Ju, R. Xie, C.-J. Cheng, P.-W. Ren and L.-Y. Chu, *J. Colloid Interface Sci.*, 2009, **336**, 235–243.

19 M. T. Gokmen, W. Van Camp, P. J. Colver, S. A. F. Bon and F. E. Du Prez, *Macromolecules*, 2009, **42**, 9289–9294.

20 W.-Q. Zhou, T.-Y. Gu, Z.-G. Su and G.-H. Ma, *Eur. Polym. J.*, 2007, **43**, 4493–4502.

21 D. Horák, Z. Pelzbauer, F. Švec and J. Kálal, *J. Appl. Polym. Sci.*, 1981, **26**, 3205–3211.

22 J.-S. Yu, S. Kang, S. B. Yoon and G. Chai, *J. Am. Chem. Soc.*, 2002, **124**, 9382–9383.

23 H. Strohm and P. Lobmann, *J. Mater. Chem.*, 2004, **14**, 2667–2673.

24 A. M. Todea, A. Merca, H. Bögge, T. Glaser, J. M. Pigga, M. L. K. Langston, T. Liu, R. Prozorov, M. Luban, C. Schröder, W. H. Casey and A. Müller, *Angew. Chem., Int. Ed.*, 2010, **49**, 514–519.

25 F. Li, J. He, W. L. Zhou and J. B. Wiley, *J. Am. Chem. Soc.*, 2003, **125**, 16166–16167.

26 J. Li and Y. Zhang, *Chem. Mater.*, 2007, **19**, 2581–2584.

27 D. Lee and D. A. Weitz, *Small*, 2009, **5**, 1932–1935.

28 C.-C. Wang, K.-C. Yang, K.-H. Lin, H.-C. Liu and F.-H. Lin, *Biomaterials*, 2011, **32**, 7118–7126.

29 M. Costantini, C. Colosi, J. Guzowski, A. Barbetta, J. Jaroszewicz, W. Święszkowski, M. Dentini and P. Garstecki, *J. Mater. Chem. B*, 2014, **2**, 2290–2300.

30 D. Eisenberg, P. Prinsen, N. J. Geels, W. Stroek, N. Yan, B. Hua, J.-L. Luo and G. Rothenberg, *RSC Adv.*, 2016, **6**, 80398–80407.

31 W. C. Yoo and A. Stein, *Chem. Mater.*, 2011, **23**, 1761–1767.

32 V. Polshettiwar, D. Cha, X. Zhang and J. M. Basset, *Angew. Chem., Int. Ed.*, 2010, **49**, 9652–9656.

33 X. Du and J. He, *Langmuir*, 2010, **26**, 10057–10062.

34 X. Du and J. He, *Langmuir*, 2011, **27**, 2972–2979.

35 X. Du and J. He, *J. Colloid Interface Sci.*, 2010, **345**, 269–277.

36 J. Wu, Y.-J. Zhu, S.-W. Cao and F. Chen, *Adv. Mater.*, 2010, **22**, 749–753.

37 X. Guo, Y. Deng, B. Tu and D. Zhao, *Langmuir*, 2010, **26**, 702–708.

38 F. Iskandar, Mikrajuddin and K. Okuyama, *Nano Lett.*, 2001, **1**, 231–234.

39 F. Iskandar, Mikrajuddin and K. Okuyama, *Nano Lett.*, 2002, **2**, 389–392.

40 M. Abdullah, F. Iskandar, S. Shibamoto, T. Ogi and K. Okuyama, *Acta Mater.*, 2004, **52**, 5151–5156.

41 A. B. D. Nandiyanto, F. Iskandar and K. Okuyama, *Chem. Lett.*, 2008, **37**, 1040–1041.

42 C. Zhang, T. Hou, J. Chen and L. Wen, *Particuology*, 2010, **8**, 447–452.

43 H. Zhang, G. C. Hardy, M. J. Rosseinsky and A. I. Cooper, *Adv. Mater.*, 2003, **15**, 78–81.

44 J.-G. Wang, H.-J. Zhou, P.-C. Sun, D.-T. Ding and T.-H. Chen, *Chem. Mater.*, 2010, **22**, 3829–3831.

45 L. Chen, G. Zhu, D. Zhang, H. Zhao, M. Guo, W. Shi and S. Qiu, *J. Mater. Chem.*, 2009, **19**, 2013–2017.

46 M. U. Martines, E. Yeong, M. Persin, A. Larbot, W. F. Voorhout, C. K. U. Kübel, P. Kooyman and E. Prouzet, *C. R. Chim.*, 2005, **8**, 627–634.

47 X. Du and J. He, *Nanoscale*, 2011, **3**, 3984–4002.

48 F. Svec and J. M. J. Fréchet, *Science*, 1996, **273**, 205–211.

49 A. J. Jose, S. Ogawa and M. Bradley, *Polymer*, 2005, **46**, 2880–2888.

50 S. Durie, K. Jerabek, C. Mason and D. C. Sherrington, *Macromolecules*, 2002, **35**, 9665–9672.

This journal is © The Royal Society of Chemistry 2017

Chem. Soc. Rev., 2017, **46**, 855–914 | 903

51 V. P. Shastri, I. Martin and R. Langer, *Proc. Natl. Acad. Sci. U. S. A.*, 2000, **97**, 1970–1975.

52 K. Ogino, H. Sato, K. Tsuchiya, H. Suzuki and S. Moriguchi, *J. Chromatogr. A*, 1995, **699**, 59–66.

53 D. C. Sherrington, *Chem. Commun.*, 1998, 2275–2286.

54 D. Dendukuri, D. C. Pregibon, J. Collins, T. A. Hatton and P. S. Doyle, *Nat. Mater.*, 2006, **5**, 365–369.

55 O. Okay, *Prog. Polym. Sci.*, 2000, **25**, 711–779.

56 D. Mark, S. Haeberle, G. Roth, F. von Stetten and R. Zengerle, *Chem. Soc. Rev.*, 2010, **39**, 1153–1182.

57 P. N. Nge, C. I. Rogers and A. T. Woolley, *Chem. Rev.*, 2013, **113**, 2550–2583.

58 M. T. Gokmen and F. E. Du Prez, *Prog. Polym. Sci.*, 2012, **37**, 365–405.

59 D. Wu, F. Xu, B. Sun, R. Fu, H. He and K. Matyjaszewski, *Chem. Rev.*, 2012, **112**, 3959–4015.

60 J. H. Moon and S. Yang, *Chem. Rev.*, 2010, **110**, 547–574.

61 J. Hu, M. Chen, X. Fang and L. Wu, *Chem. Soc. Rev.*, 2011, **40**, 5472–5491.

62 A. Stein, B. E. Wilson and S. G. Rudisill, *Chem. Soc. Rev.*, 2013, **42**, 2763–2803.

63 Y. Liu, J. Goebl and Y. Yin, *Chem. Soc. Rev.*, 2013, **42**, 2610–2653.

64 N. D. Petkovich and A. Stein, *Chem. Soc. Rev.*, 2013, **42**, 3721–3739.

65 A. D. Roberts, X. Li and H. Zhang, *Chem. Soc. Rev.*, 2014, **43**, 4341–4356.

66 C. M. A. Parlett, K. Wilson and A. F. Lee, *Chem. Soc. Rev.*, 2013, **42**, 3876–3893.

67 C. Triantafillidis, M. S. Elsaesser and N. Husing, *Chem. Soc. Rev.*, 2013, **42**, 3833–3846.

68 A. Walther and A. H. E. Müller, *Chem. Rev.*, 2013, **113**, 5194–5261.

69 E. Tumarkin and E. Kumacheva, *Chem. Soc. Rev.*, 2009, **38**, 2161–2168.

70 S. Marre and K. F. Jensen, *Chem. Soc. Rev.*, 2010, **39**, 1183–1202.

71 S.-H. Kim, J.-M. Lim, S.-K. Lee, C.-J. Heo and S.-M. Yang, *Soft Matter*, 2010, **6**, 1092–1110.

72 J. H. Kim, T. Y. Jeon, T. M. Choi, T. S. Shim, S.-H. Kim and S.-M. Yang, *Langmuir*, 2013, **30**, 1473–1488.

73 W. Engl, R. Backov and P. Panizza, *Curr. Opin. Colloid Interface Sci.*, 2008, **13**, 206–216.

74 W. Drenckhan and D. Langevin, *Curr. Opin. Colloid Interface Sci.*, 2010, **15**, 341–358.

75 A. Testouri, L. Arriaga, C. Honorez, M. Ranft, J. Rodrigues, A. van der Net, A. Lecchi, A. Salonen, E. Rio and R.-M. Guillermic, *Colloids Surf., A*, 2012, **413**, 17–24.

76 C. A. Serra and Z. Chang, *Chem. Eng. Technol.*, 2008, **31**, 1099–1115.

77 Y. Xia and G. M. Whitesides, *Angew. Chem., Int. Ed.*, 1998, **37**, 550–575.

78 D. C. Duffy, J. C. McDonald, O. J. A. Schueller and G. M. Whitesides, *Anal. Chem.*, 1998, **70**, 4974–4984.

79 A. S. Utada, E. Lorenceau, D. R. Link, P. D. Kaplan, H. A. Stone and D. A. Weitz, *Science*, 2005, **308**, 537–541.

80 E. Lorenceau, A. S. Utada, D. R. Link, G. Cristobal, M. Joanicot and D. A. Weitz, *Langmuir*, 2005, **21**, 9183–9186.

81 A. Utada, L.-Y. Chu, A. Fernandez-Nieves, D. Link, C. Holtze and D. Weitz, *MRS Bull.*, 2007, **32**, 702–708.

82 P. K. Yuen, *Lab Chip*, 2008, **8**, 1374–1378.

83 P. K. Yuen, J. T. Bliss, C. C. Thompson and R. C. Peterson, *Lab Chip*, 2009, **9**, 3303–3305.

84 P. K. Yuen and V. N. Goral, *Lab Chip*, 2010, **10**, 384–387.

85 A. R. Abate, D. Lee, T. Do, C. Holtze and D. A. Weitz, *Lab Chip*, 2008, **8**, 516–518.

86 T. Nisisako and T. Torii, *Lab Chip*, 2008, **8**, 287–293.

87 H. Keng-Shiang, L. Ming-Kai, W. Chun-Han, Y. Yu-Tang and L. Yu-Cheng, *J. Micromech. Microeng.*, 2007, **17**, 1428–1434.

88 M. Miyazaki, T. Honda, H. Nakamura and H. Maeda, *Chem. Eng. Technol.*, 2007, **30**, 300–304.

89 H. Becker and C. Gärtner, *Anal. Bioanal. Chem.*, 2008, **390**, 89–111.

90 M. Bouquey, C. Serra, N. Berton, L. Prat and G. Hadziioannou, *Chem. Eng. J.*, 2008, **135**, S93–S98.

91 C. Serra, N. Berton, M. Bouquey, L. Prat and G. Hadziioannou, *Langmuir*, 2007, **23**, 7745–7750.

92 Z. Chang, C. A. Serra, M. Bouquey, L. Prat and G. Hadziioannou, *Lab Chip*, 2009, **9**, 3007–3011.

93 C. Ohm, C. Serra and R. Zentel, *Adv. Mater.*, 2009, **21**, 4859–4862.

94 C. Zhenqi, A. S. Christophe, B. Michel, K. Isabelle, L. Shuning and J. M. Köhler, *Nanotechnology*, 2010, **21**, 015605.

95 A. Terray and S. J. Hart, *Lab Chip*, 2010, **10**, 1729–1731.

96 J. Seidl, J. Malinský, K. Dušek and W. Heitz, *Fortschritte der Hochpolymeren-Forschung*, Springer, Berlin, Heidelberg, 1967, pp. 113–213.

97 M. J. Beneš, D. Horák and F. Svec, *J. Sep. Sci.*, 2005, **28**, 1855–1875.

98 E. C. Peters, M. Petro, F. Svec and J. M. J. Fréchet, *Anal. Chem.*, 1997, **69**, 3646–3649.

99 E. C. Peters, F. Svec and J. M. J. Fréchet, *Adv. Mater.*, 1999, **11**, 1169–1181.

100 C. Yu, M. Xu, F. Svec and J. M. J. Fréchet, *J. Polym. Sci., Part A: Polym. Chem.*, 2002, **40**, 755–769.

101 C. Yu, M. H. Davey, F. Svec and J. M. J. Fréchet, *Anal. Chem.*, 2001, **73**, 5088–5096.

102 J. Fréchet, *Electrophoresis*, 2001, **22**, 3959–3967.

103 Á. Sáfrány, B. Beiler, K. László and F. Svec, *Polymer*, 2005, **46**, 2862–2871.

104 J. Ugelstad, K. H. Kaggerud, F. K. Hansen and A. Berge, *Makromol. Chem.*, 1979, **180**, 737–744.

105 J. Ugelstad, L. Soderberg, A. Berge and J. Bergstrom, *Nature*, 1983, **303**, 95–96.

106 C. M. Cheng, F. J. Micale, J. W. Vanderhoff and M. S. El-Aasser, *J. Polym. Sci., Part A: Polym. Chem.*, 1992, **30**, 235–244.

107 C. M. Cheng, J. W. Vanderhoff and M. S. El-Aasser, *J. Polym. Sci., Part A: Polym. Chem.*, 1992, **30**, 245–256.

108 W. H. Li and H. D. Stöver, *J. Polym. Sci., Part A: Polym. Chem.*, 1998, **36**, 1543–1551.

109 E. Vivaldo-Lima, P. E. Wood, A. E. Hamielec and A. Penlidis, *Ind. Eng. Chem. Res.*, 1997, **36**, 939–965.

904 | *Chem. Soc. Rev.*, 2017, **46**, 855–914

This journal is © The Royal Society of Chemistry 2017

110 J. Haginaka, *J. Chromatogr. B: Anal. Technol. Biomed. Life Sci.*, 2008, **866**, 3–13.

111 H. Kawaguchi, *Prog. Polym. Sci.*, 2000, **25**, 1171–1210.

112 P. J. Dowding and B. Vincent, *Colloids Surf., A*, 2000, **161**, 259–269.

113 K. N. N. Jayachandran and P. R. Chatterji, *J. Macromol. Sci., Part C*, 2001, **41**, 79–94.

114 S. Kawaguchi and K. Ito, in *Polymer Particles*, ed. M. Okubo, Springer, Berlin, Heidelberg, 2005, pp. 299–328.

115 L. Barner, *Adv. Mater.*, 2009, **21**, 2547–2553.

116 A. Pich and W. Richtering, in *Chemical Design of Responsive Microgels*, ed. A. Pich and W. Richtering, Springer, Berlin, Heidelberg, 2011, pp. 1–37.

117 G. T. Vladisavljević and R. A. Williams, *Adv. Colloid Interface Sci.*, 2005, **113**, 1–20.

118 S. van der Graaf, C. Schroën and R. Boom, *J. Membr. Sci.*, 2005, **251**, 7–15.

119 J. L. Steinbacher and D. T. McQuade, *J. Polym. Sci., Part A: Polym. Chem.*, 2006, **44**, 6505–6533.

120 J. K. Oh, R. Drumright, D. J. Siegwart and K. Matyjaszewski, *Prog. Polym. Sci.*, 2008, **33**, 448–477.

121 F. Svec and J. M. J. Frechet, *Anal. Chem.*, 1992, **64**, 820–822.

122 F. Svec and J. M. J. Frechet, *Chem. Mater.*, 1995, **7**, 707–715.

123 M. Jancǒ, S. Xie, D. S. Peterson, R. W. Allington, F. Svec and J. M. J. Fréchet, *J. Sep. Sci.*, 2002, **25**, 909–916.

124 G. Guiochon, *J. Chromatogr. A*, 2007, **1168**, 101–168.

125 B. Paredes, S. González, M. Rendueles and J. M. Díaz, *Sep. Purif. Technol.*, 2004, **40**, 243–250.

126 S. Xu, Z. Nie, M. Seo, P. Lewis, E. Kumacheva, H. A. Stone, P. Garstecki, D. B. Weibel, I. Gitlin and G. M. Whitesides, *Angew. Chem., Int. Ed.*, 2005, **44**, 724–728.

127 M. Seo, Z. Nie, S. Xu, M. Mok, P. C. Lewis, R. Graham and E. Kumacheva, *Langmuir*, 2005, **21**, 11614–11622.

128 Z. Nie, S. Xu, M. Seo, P. C. Lewis and E. Kumacheva, *J. Am. Chem. Soc.*, 2005, **127**, 8058–8063.

129 P. C. Lewis, R. R. Graham, Z. Nie, S. Xu, M. Seo and E. Kumacheva, *Macromolecules*, 2005, **38**, 4536–4538.

130 T. Nisisako, T. Torii and T. Higuchi, *Chem. Eng. J.*, 2004, **101**, 23–29.

131 W. J. Jeong, J. Y. Kim, J. Choo, E. K. Lee, C. S. Han, D. J. Beebe, G. H. Seong and S. H. Lee, *Langmuir*, 2005, **21**, 3738–3741.

132 D. Horák, F. Švec, M. Bleha and J. Kálal, *Angew. Makromol. Chem.*, 1981, **95**, 109–115.

133 S. Dubinsky, H. Zhang, Z. Nie, I. Gourevich, D. Voicu, M. Deetz and E. Kumacheva, *Macromolecules*, 2008, **41**, 3555–3561.

134 J. Wan, A. Bick, M. Sullivan and H. A. Stone, *Adv. Mater.*, 2008, **20**, 3314–3318.

135 W. H. Tan and S. Takeuchi, *Adv. Mater.*, 2007, **19**, 2696–2701.

136 D. Štefanec and P. Krajnc, *React. Funct. Polym.*, 2005, **65**, 37–45.

137 D. Horák, F. Švec, M. Ilavský, M. Bleha, J. Baldrián and J. Kálal, *Angew. Makromol. Chem.*, 1981, **95**, 117–127.

138 A. G. Mikos, G. Sarakinos, S. M. Leite, J. P. Vacant and R. Langer, *Biomaterials*, 1993, **14**, 323–330.

139 T. Watanabe, C. G. Lopez, J. F. Douglas, T. Ono and J. O. T. Cabral, *Langmuir*, 2014, **30**, 2470–2479.

140 J. Y. Sim, J. H. Choi, J. M. Lim, S. Cho, S. H. Kim and S. M. Yang, *Small*, 2014, **10**, 3979–3985.

141 C. E. Udoh, V. Garbin and J. T. Cabral, *Langmuir*, 2016, **32**, 8131–8140.

142 M. Okubo, Y. Murakami and T. Fujiwara, *Colloid Polym. Sci.*, 1996, **274**, 520–524.

143 M. Okubo, A. Yamaguchi and T. Fujiwara, *Colloid Polym. Sci.*, 1999, **277**, 1005–1008.

144 T. Fujibayashi, Y. Komatsu, N. Konishi, H. Yamori and M. Okubo, *Ind. Eng. Chem. Res.*, 2008, **47**, 6445–6449.

145 S.-H. Kim, J. Y. Sim, J.-M. Lim and S.-M. Yang, *Angew. Chem., Int. Ed.*, 2010, **49**, 3786–3790.

146 J. Choi, W.-P. Jeon and H. Choi, *Phys. Fluids*, 2006, **18**, 041702.

147 D. Falconnet, G. Csucs, H. Michelle Grandin and M. Textor, *Biomaterials*, 2006, **27**, 3044–3063.

148 U. H. F. Bunz, *Adv. Mater.*, 2006, **18**, 973–989.

149 M. R. Kim, S. Lee, J.-K. Park and K. Y. Cho, *Chem. Commun.*, 2010, **46**, 7433–7435.

150 M. Okubo, T. Fujiwara and A. Yamaguchi, *Colloid Polym. Sci.*, 1998, **276**, 186–189.

151 N. Konishi, T. Fujibayashi, T. Tanaka, H. Minami and M. Okubo, *Polym. J.*, 2010, **42**, 66–71.

152 Y. K. Takahara, S. Ikeda, S. Ishino, K. Tachi, K. Ikeue, T. Sakata, T. Hasegawa, H. Mori, M. Matsumura and B. Ohtani, *J. Am. Chem. Soc.*, 2005, **127**, 6271–6275.

153 Y. K. Takahara, S. Ikeda, K. Tachi, T. Sakata, T. Hasegawa, H. Mori, M. Matsumura and B. Ohtani, *Chem. Commun.*, 2005, 4205–4207.

154 S.-H. Kim, C.-J. Heo, S. Y. Lee, G.-R. Yi and S.-M. Yang, *Chem. Mater.*, 2007, **19**, 4751–4760.

155 S.-H. Kim, J. Shim, J.-M. Lim, S. Lee and S.-M. Yang, *New J. Phys.*, 2009, **11**, 075014.

156 S. H. Kim, S. J. Jeon, G. R. Yi, C. J. Heo, J. H. Choi and S. M. Yang, *Adv. Mater.*, 2008, **20**, 1649–1655.

157 S.-H. Kim, G.-R. Yi, K. H. Kim and S.-M. Yang, *Langmuir*, 2008, **24**, 2365–2371.

158 S.-H. Kim, S.-H. Kim and S.-M. Yang, *Adv. Mater.*, 2009, **21**, 3771–3775.

159 S.-H. Kim, J.-M. Lim, W. C. Jeong, D.-G. Choi and S.-M. Yang, *Adv. Mater.*, 2008, **20**, 3211–3217.

160 S.-H. Kim, S. Y. Lee and S.-M. Yang, *Angew. Chem., Int. Ed.*, 2010, **49**, 2535–2538.

161 K.-H. Hwangbo, M. R. Kim, C.-S. Lee and K. Y. Cho, *Soft Matter*, 2011, **7**, 10874–10878.

162 J. H. Lee, C.-S. Lee and K. Y. Cho, *ACS Appl. Mater. Interfaces*, 2014, **6**, 16493–16497.

163 X. Gong, W. Wen and P. Sheng, *Langmuir*, 2009, **25**, 7072–7077.

164 R. A. Prasath, M. T. Gokmen, P. Espeel and F. E. Du Prez, *Polym. Chem.*, 2010, **1**, 685–692.

165 A. G. Lee, C. P. Arena, D. J. Beebe and S. P. Palecek, *Biomacromolecules*, 2010, **11**, 3316–3324.

166 J. B. Wacker, V. K. Parashar and M. A. M. Gijs, *Langmuir*, 2011, **27**, 4380–4385.

This journal is © The Royal Society of Chemistry 2017

Chem. Soc. Rev., 2017, **46**, 855–914 | 905

167 C. Paquet, Z. J. Jakubek and B. Simard, *ACS Appl. Mater. Interfaces*, 2012, **4**, 4934–4941.

168 J. Yun, C. Tu, D.-Q. Lin, L. Xu, Y. Guo, S. Shen, S. Zhang, K. Yao, Y.-X. Guan and S.-J. Yao, *J. Chromatogr. A*, 2012, **1247**, 81–88.

169 W. J. Duncanson, M. Zieringer, O. Wagner, J. N. Wilking, A. Abbaspourrad, R. Haag and D. A. Weitz, *Soft Matter*, 2012, **8**, 10636–10640.

170 W.-C. Jeong, S.-H. Kim and S.-M. Yang, *ACS Appl. Mater. Interfaces*, 2014, **6**, 826–832.

171 C.-L. Mou, X.-J. Ju, L. Zhang, R. Xie, W. Wang, N.-N. Deng, J. Wei, Q. Chen and L.-Y. Chu, *Langmuir*, 2014, **30**, 1455–1464.

172 S. Wang, C. Liu, H. Wang, G. Chen, M. Cong, W. Song, Q. Jia, S. Xu and W. Xu, *ACS Appl. Mater. Interfaces*, 2014, **6**, 11706–11713.

173 Y. Yang, N. Bajaj, P. Xu, K. Ohn, M. D. Tsifansky and Y. Yeo, *Biomaterials*, 2009, **30**, 1947–1953.

174 H.-R. Lin, C.-J. Kuo, C. Y. Yang, S.-Y. Shaw and Y.-J. Wu, *J. Biomed. Mater. Res.*, 2002, **63**, 271–279.

175 S.-W. Choi, Y. Zhang and Y. Xia, *Adv. Funct. Mater.*, 2009, **19**, 2943–2949.

176 S. E. Bae, J. S. Son, K. Park and D. K. Han, *J. Controlled Release*, 2009, **133**, 37–43.

177 K. Naidoo, H. Rolfes, K. Easton, S. Moolman, A. Chetty, W. Richter and R. Nilen, *Mater. Lett.*, 2008, **62**, 252–254.

178 K. Jiang, A. Sposito, J. Liu, S. R. Raghavan and D. L. DeVoe, *Polymer*, 2012, **53**, 5469–5475.

179 R. K. Shah, H. C. Shum, A. C. Rowat, D. Lee, J. J. Agresti, A. S. Utada, L.-Y. Chu, J.-W. Kim, A. Fernandez-Nieves, C. J. Martinez and D. A. Weitz, *Mater. Today*, 2008, **11**, 18–27.

180 H. Becker and C. Gärtner, *Electrophoresis*, 2000, **21**, 12–26.

181 J. Liu, C.-F. Chen, C.-W. Chang and D. L. DeVoe, *Biosens. Bioelectron.*, 2010, **26**, 182–188.

182 R. Mallik and D. S. Hage, *Journal of separation science*, 2006, **29**, 1686–1704.

183 L. Y. Chu, J. W. Kim, R. K. Shah and D. A. Weitz, *Adv. Funct. Mater.*, 2007, **17**, 3499–3504.

184 M. V. Sefton, L. Kharlip, V. Horvath and T. Roberts, *J. Controlled Release*, 1992, **19**, 289–297.

185 N. R. Cameron and D. C. Sherrington, *Biopolymers Liquid Crystalline Polymers Phase Emulsion*, Springer, Berlin, Heidelberg, 1996, pp. 163–214.

186 A. Barbetta and N. R. Cameron, *Macromolecules*, 2004, **37**, 3188–3201.

187 P. Krajnc, N. Leber, J. F. Brown and N. R. Cameron, *React. Funct. Polym.*, 2006, **66**, 81–91.

188 E. Ruckenstein, *Polymer Synthesis/Polymer Catalysis*, Springer, Berlin, Heidelberg, 1997, pp. 1–58.

189 S. J. Pierre, J. C. Thies, A. Dureault, N. R. Cameron, J. C. M. van Hest, N. Carette, T. Michon and R. Weberskirch, *Adv. Mater.*, 2006, **18**, 1822–1826.

190 N. R. Cameron, *Polymer*, 2005, **46**, 1439–1449.

191 O. Kulygin and M. S. Silverstein, *Soft Matter*, 2007, **3**, 1525–1529.

192 H. Zhang and A. I. Cooper, *Soft Matter*, 2005, **1**, 107–113.

193 H. Zhang, J. Long and A. I. Cooper, *J. Am. Chem. Soc.*, 2005, **127**, 13482–13483.

194 R. Butler, C. M. Davies and A. I. Cooper, *Adv. Mater.*, 2001, **13**, 1459–1463.

195 M. T. Gokmen, B. G. De Geest, W. E. Hennink and F. E. Du Prez, *ACS Appl. Mater. Interfaces*, 2009, **1**, 1196–1202.

196 E. Quevedo, J. Steinbacher and D. T. McQuade, *J. Am. Chem. Soc.*, 2005, **127**, 10498–10499.

197 M.-H. Lee, S.-G. Oh, S.-K. Moon and S.-Y. Bae, *J. Colloid Interface Sci.*, 2001, **240**, 83–89.

198 L. A. M. Ferreira, M. Seiller, J. L. Grossiord, J. P. Marty and J. Wepierre, *Int. J. Pharm.*, 1994, **109**, 251–259.

199 M. Nakano, *Adv. Drug Delivery Rev.*, 2000, **45**, 1–4.

200 D. Vasiljevic, J. Parojcic, M. Primorac and G. Vuleta, *Int. J. Pharm.*, 2006, **309**, 171–177.

201 S. Koster, F. E. Angile, H. Duan, J. J. Agresti, A. Wintner, C. Schmitz, A. C. Rowat, C. A. Merten, D. Pisignano, A. D. Griffiths and D. A. Weitz, *Lab Chip*, 2008, **8**, 1110–1115.

202 C. Lobato-Calleros, E. Rodriguez, O. Sandoval-Castilla, E. J. Vernon-Carter and J. Alvarez-Ramirez, *Food Res. Int.*, 2006, **39**, 678–685.

203 J. Weiss, I. Scherze and G. Muschiolik, *Food Hydrocolloids*, 2005, **19**, 605–615.

204 M. Seo, C. Paquet, Z. Nie, S. Xu and E. Kumacheva, *Soft Matter*, 2007, **3**, 986–992.

205 S. Okushima, T. Nisisako, T. Torii and T. Higuchi, *Langmuir*, 2004, **20**, 9905–9908.

206 R. Bocanegra, J. Luis Sampedro, A. Gañán-Calvo and M. Marquez, *J. Microencapsulation*, 2005, **22**, 745–759.

207 H. Shih-Hao, T. Wei-Heong, T. Fan-Gang and T. Shoji, *J. Micromech. Microeng.*, 2006, **16**, 2336–2344.

208 D. Lee and D. A. Weitz, *Adv. Mater.*, 2008, **20**, 3498–3503.

209 S. Takeuchi, P. Garstecki, D. B. Weibel and G. M. Whitesides, *Adv. Mater.*, 2005, **17**, 1067–1072.

210 S. W. Choi, I. W. Cheong, J. H. Kim and Y. Xia, *Small*, 2009, **5**, 454–459.

211 A. Barrero and I. G. Loscertales, *Annu. Rev. Fluid Mech.*, 2007, **39**, 89–106.

212 A. S. Utada, A. Fernandez-Nieves, H. A. Stone and D. A. Weitz, *Phys. Rev. Lett.*, 2007, **99**, 094502.

213 A. I. Cooper, *Adv. Mater.*, 2003, **15**, 1049–1059.

214 F. Fernández-Trillo, J. C. M. van Hest, J. C. Thies, T. Michon, R. Weberskirch and N. R. Cameron, *Adv. Mater.*, 2009, **21**, 55–59.

215 S. Partap, I. Rehman, J. R. Jones and J. A. Darr, *Adv. Mater.*, 2006, **18**, 501–504.

216 N. B. Cramer, S. K. Reddy, A. K. O'Brien and C. N. Bowman, *Macromolecules*, 2003, **36**, 7964–7969.

217 B. D. Fairbanks, T. F. Scott, C. J. Kloxin, K. S. Anseth and C. N. Bowman, *Macromolecules*, 2009, **42**, 211–217.

218 W. Li, H. H. Pham, Z. Nie, B. MacDonald, A. Güenther and E. Kumacheva, *J. Am. Chem. Soc.*, 2008, **130**, 9935–9941.

219 B.-S. Chiou, R. J. English and S. A. Khan, *Macromolecules*, 1996, **29**, 5368–5374.

220 B.-S. Chiou and S. A. Khan, *Macromolecules*, 1997, **30**, 7322–7328.

906 | *Chem. Soc. Rev.*, 2017, **46**, 855–914

This journal is © The Royal Society of Chemistry 2017

221 R. Bhargava, S.-Q. Wang and J. L. Koenig, *Macromolecules*, 1999, **32**, 2748–2760.

222 M. Natali, S. Begolo, T. Carofiglio and G. Mistura, *Lab Chip*, 2008, **8**, 492–494.

223 F.-C. Chang and Y.-C. Su, *J. Micromech. Microeng.*, 2008, **18**, 065018.

224 M. A. M. Gijs, F. Lacharme and U. Lehmann, *Chem. Rev.*, 2010, **110**, 1518–1563.

225 X. Wang, X. Ding, Z. Zheng, X. Hu, X. Cheng and Y. Peng, *Macromol. Rapid Commun.*, 2006, **27**, 1180–1184.

226 C. H. Chen, A. R. Abate, D. Lee, E. M. Terentjev and D. A. Weitz, *Adv. Mater.*, 2009, **21**, 3201–3204.

227 N. Pamme, J. C. Eijkel and A. Manz, *J. Magn. Magn. Mater.*, 2006, **307**, 237–244.

228 C. Ye, A. Chen, P. Colombo and C. Martinez, *J. R. Soc., Interface*, 2010, **7**, S461–S473.

229 P. Krajnc, N. Leber, D. Štefanec, S. Kontrec and A. Podgornik, *J. Chromatogr. A*, 2005, **1065**, 69–73.

230 R. Yoshida, K. Uchida, Y. Kaneko, K. Sakai, A. Kikuchi, Y. Sakurai and T. Okano, *Nature*, 1995, **374**, 240–242.

231 L.-W. Xia, R. Xie, X.-J. Ju, W. Wang, Q. Chen and L.-Y. Chu, *Nat. Commun.*, 2013, **4**, 2226–2230.

232 T. Okajima, I. Harada, K. Nishio and S. Hirotsu, *J. Chem. Phys.*, 2002, **116**, 9068–9077.

233 X.-Z. Zhang, Y.-Y. Yang and T.-S. Chung, *Langmuir*, 2002, **18**, 2538–2542.

234 J. Xiao-Jie, C. Liang-Yin, Z. Xiao-Li, H. Lin, S. Hang and C. Wen-Mei, *Smart Mater. Struct.*, 2006, **15**, 1767–1774.

235 L.-W. Xia, X.-J. Ju, J.-J. Liu, R. Xie and L.-Y. Chu, *J. Colloid Interface Sci.*, 2010, **349**, 106–113.

236 Y. Kaneko, S. Nakamura, K. Sakai, T. Aoyagi, A. Kikuchi, Y. Sakurai and T. Okano, *Macromolecules*, 1998, **31**, 6099–6105.

237 J. Zhang, L.-Y. Chu, C.-J. Cheng, D.-F. Mi, M.-Y. Zhou and X.-J. Ju, *Polymer*, 2008, **49**, 2595–2603.

238 X.-Z. Zhang, Y.-Y. Yang, T.-S. Chung and K.-X. Ma, *Langmuir*, 2001, **17**, 6094–6099.

239 T. Serizawa, K. Wakita and M. Akashi, *Macromolecules*, 2002, **35**, 10–12.

240 H. Tokuyama and A. Kanehara, *Langmuir*, 2007, **23**, 11246–11251.

241 S. Q. Huang, B. C. Lin and J. H. Qin, *Electrophoresis*, 2011, **32**, 3364–3370.

242 L. L. Yue, R. Xie, J. Wei, X. J. Ju, W. Wang and L. Y. Chu, *J. Colloid Interface Sci.*, 2012, **377**, 137–144.

243 L.-Y. Chu, A. S. Utada, R. K. Shah, J.-W. Kim and D. A. Weitz, *Angew. Chem., Int. Ed.*, 2007, **46**, 8970–8974.

244 L. Liu, W. Wang, X.-J. Ju, R. Xie and L.-Y. Chu, *Soft Matter*, 2010, **6**, 3759–3763.

245 C.-L. Mou, X.-H. He, X.-J. Ju, R. Xie, Z. Liu, L. Liu, Z. Zhang and L.-Y. Chu, *Chem. Eng. J.*, 2012, **210**, 212–219.

246 L. Liu, X.-L. Song, X.-J. Ju, R. Xie, Z. Liu and L.-Y. Chu, *J. Phys. Chem. B*, 2012, **116**, 974–979.

247 S. Fujii, S. P. Armes, T. Araki and H. Ade, *J. Am. Chem. Soc.*, 2005, **127**, 16808–16809.

248 B. R. Saunders, N. Laajam, E. Daly, S. Teow, X. Hu and R. Stepto, *Adv. Colloid Interface Sci.*, 2009, **147–148**, 251–262.

249 L.-Y. Chu, R. Xie, X.-J. Ju and W. Wang, *Smart Hydrogel Functional Materials*, Springer, Berlin, Heidelberg, 2013, pp. 135–152.

250 S.-W. Pi, X.-J. Ju, H.-G. Wu, R. Xie and L.-Y. Chu, *J. Colloid Interface Sci.*, 2010, **349**, 512–518.

251 Y. Li and S. Zhou, *Sens. Actuators, B*, 2013, **177**, 792–799.

252 B. Zhao, J. S. Moore and D. J. Beebe, *Science*, 2001, **291**, 1023–1026.

253 B. Zhao, J. S. Moore and D. J. Beebe, *Anal. Chem.*, 2002, **74**, 4259–4268.

254 B. Zhao, N. O. L. Viernes, J. S. Moore and D. J. Beebe, *J. Am. Chem. Soc.*, 2002, **124**, 5284–5285.

255 D. Kim and D. J. Beebe, *J. Appl. Polym. Sci.*, 2008, **110**, 1581–1589.

256 M.-S. Kim and S.-J. Lee, *J. Supercrit. Fluids*, 2004, **31**, 217–225.

257 M. Zeng and Z. Fang, *J. Membr. Sci.*, 2004, **245**, 95–102.

258 W. Liu, L. Zhu, C. Huang and X. Jin, *ACS Appl. Mater. Interfaces*, 2016, **8**, 34870–34878.

259 D. Li, T. Wu, N. He, J. Wang, W. Chen, L. He, C. Huang, H. A. Ei-Hamshary, S. S. Al-Deyab, Q. Ke and X. Mo, *Colloids Surf., B*, 2014, **121**, 432–443.

260 J. Y. Park, S. W. Han and I. H. Lee, *J. Ind. Eng. Chem.*, 2007, **13**, 1002–1008.

261 X. Wu, Y. Liu, X. Li, P. Wen, Y. Zhang, Y. Long, X. Wang, Y. Guo, F. Xing and J. Gao, *Acta Biomater.*, 2010, **6**, 1167–1177.

262 N. Bhardwaj and S. C. Kundu, *Biotechnol. Adv.*, 2010, **28**, 325–347.

263 J. S. Temenoff and A. G. Mikos, *Biomaterials*, 2000, **21**, 431–440.

264 P. A. George, K. Quinn and J. J. Cooper-White, *Biomaterials*, 2010, **31**, 641–647.

265 A. Salerno, M. Oliviero, E. Di Maio, S. Iannace and P. A. Netti, *J. Mater. Sci.: Mater. Med.*, 2009, **20**, 2043–2051.

266 W. Dai, N. Kawazoe, X. Lin, J. Dong and G. Chen, *Biomaterials*, 2010, **31**, 2141–2152.

267 S. J. Hollister, *Nat. Mater.*, 2005, **4**, 518–524.

268 D. Gallego, N. Ferrell, Y. Sun and D. J. Hansford, *Mater. Sci. Eng., C*, 2008, **28**, 353–358.

269 J. L. Simon, S. Michna, J. A. Lewis, E. D. Rekow, V. P. Thompson, J. E. Smay, A. Yampolsky, J. R. Parsons and J. L. Ricci, *J. Biomed. Mater. Res., Part A*, 2007, **83A**, 747–758.

270 M. S. Hahn, J. S. Miller and J. L. West, *Adv. Mater.*, 2006, **18**, 2679–2684.

271 A. Barbetta, R. J. Carnachan, K. H. Smith, C.-T. Zhao, N. R. Cameron, R. Kataky, M. Hayman, S. A. Przyborski and M. Swan, *Macromol. Symp.*, 2005, **226**, 203–212.

272 I. Pulko and P. Krajnc, *Macromol. Rapid Commun.*, 2012, **33**, 1731–1746.

273 S. D. Kimmins and N. R. Cameron, *Adv. Funct. Mater.*, 2011, **21**, 211–225.

274 R.-C. Luo and C.-H. Chen, *Sci. Res.*, 2012, **1**, 1–23.

275 K.-Y. Chung, N. C. Mishra, C.-C. Wang, F.-H. Lin and K.-H. Lin, *Biomicrofluidics*, 2009, **3**, 022403.

This journal is © The Royal Society of Chemistry 2017

Chem. Soc. Rev., 2017, **46**, 855–914 | 907

276 C.-C. Wang, K.-C. Yang, K.-H. Lin, C.-C. Wu, Y.-L. Liu, F.-H. Lin and I.-H. Chen, *Biotechnol. Bioeng.*, 2014, **111**, 2338–2348.

277 L. Moroni, J. R. de Wijn and C. A. van Blitterswijk, *Biomaterials*, 2006, **27**, 974–985.

278 T. B. F. Woodfield, J. Malda, J. de Wijn, F. Péters, J. Riesle and C. A. van Blitterswijk, *Biomaterials*, 2004, **25**, 4149–4161.

279 A. van der Net, A. Gryson, M. Ranft, F. Elias, C. Stubenrauch and W. Drenckhan, *Colloids Surf., A*, 2009, **346**, 5–10.

280 C. Colosi, M. Costantini, A. Barbetta, R. Pecci, R. Bedini and M. Dentini, *Langmuir*, 2013, **29**, 82–91.

281 P. Jankowski, D. Ogończyk, L. Derzsi, W. Lisowski and P. Garstecki, *Microfluid. Nanofluid.*, 2013, **14**, 597–604.

282 R. A. Barry and P. Wiltzius, *Langmuir*, 2006, **22**, 1369–1374.

283 W. Li, J. Greener, D. Voicu and E. Kumacheva, *Lab Chip*, 2009, **9**, 2715–2721.

284 J. Guzowski, P. M. Korczyk, S. Jakiela and P. Garstecki, *Lab Chip*, 2011, **11**, 3593–3595.

285 A. Quell, B. de Bergolis, W. Drenckhan and C. Stubenrauch, *Macromolecules*, 2016, **49**, 5059–5067.

286 G.-R. Yi, J. H. Moon and S.-M. Yang, *Chem. Mater.*, 2001, **13**, 2613–2618.

287 J. H. Moon, G. R. Yi, S. M. Yang, D. J. Pine and S. B. Park, *Adv. Mater.*, 2004, **16**, 605–609.

288 Y. Zhao, L. Shang, Y. Cheng and Z. Gu, *Acc. Chem. Res.*, 2014, **47**, 3632–3642.

289 Y. Zhao, X. Zhao, J. Hu, M. Xu, W. Zhao, L. Sun, C. Zhu, H. Xu and Z. Gu, *Adv. Mater.*, 2009, **21**, 569–572.

290 Y. Zhao, X. Zhao, C. Sun, J. Li, R. Zhu and Z. Gu, *Anal. Chem.*, 2008, **80**, 1598–1605.

291 Y.-J. Zhao, X.-W. Zhao, J. Hu, J. Li, W.-Y. Xu and Z.-Z. Gu, *Angew. Chem., Int. Ed.*, 2009, **48**, 7350–7352.

292 Y. Zhao, X. Zhao, B. Tang, W. Xu, J. Li, J. Hu and Z. Gu, *Adv. Funct. Mater.*, 2010, **20**, 976–982.

293 Y. Zhao, X. Zhao, B. Tang, W. Xu and Z. Gu, *Langmuir*, 2010, **26**, 6111–6114.

294 S. G. Johnson and J. D. Joannopoulos, *Photonic crystals: the road from theory to practice*, Springer Science & Business Media, 2001.

295 J. Wang, Y. Hu, R. Deng, R. Liang, W. Li, S. Liu and J. Zhu, *Langmuir*, 2013, **29**, 8825–8834.

296 B. Ye, H. Ding, Y. Cheng, H. Gu, Y. Zhao, Z. Xie and Z. Gu, *Adv. Mater.*, 2014, **26**, 3270–3274.

297 O. D. Velev, A. M. Lenhoff and E. W. Kaler, *Science*, 2000, **287**, 2240–2243.

298 Y. Zhao, X. Zhao and Z. Gu, *Adv. Funct. Mater.*, 2010, **20**, 2970–2988.

299 N. V. Plechkova and K. R. Seddon, *Chem. Soc. Rev.*, 2008, **37**, 123–150.

300 J. Cui, W. Zhu, N. Gao, J. Li, H. Yang, Y. Jiang, P. Seidel, B. J. Ravoo and G. Li, *Angew. Chem., Int. Ed.*, 2014, **53**, 3844–3848.

301 H. C. Shum, Y.-J. Zhao, S.-H. Kim and D. A. Weitz, *Angew. Chem.*, 2011, **123**, 1686–1689.

302 H. C. Shum, Y.-J. Zhao, S.-H. Kim and D. A. Weitz, *Angew. Chem., Int. Ed.*, 2011, **50**, 1648–1651.

303 M. Elsayed, J. Huang and M. Edirisinghe, *Mater. Sci. Eng., C*, 2015, **46**, 132–139.

304 M. Elsayed, A. Kothandaraman, M. Edirisinghe and J. Huang, *Langmuir*, 2016, **32**, 13377–13385.

305 S. Morgenthaler, C. Zink and N. D. Spencer, *Soft Matter*, 2008, **4**, 419–434.

306 R. B. Rajendra, G. Jan, N. C. Bryce, W. S. Harry and L.-V. Andrea, *Nanotechnology*, 2003, **14**, 1145–1152.

307 H. Cao, J. O. Tegenfeldt, R. H. Austin and S. Y. Chou, *Appl. Phys. Lett.*, 2002, **81**, 3058–3060.

308 B. E. Collins, K. P. S. Dancil, G. Abbi and M. J. Sailor, *Adv. Funct. Mater.*, 2002, **12**, 187–191.

309 C. Huwiler, T. P. Kunzler, M. Textor, J. Vörös and N. D. Spencer, *Langmuir*, 2007, **23**, 5929–5935.

310 L. M. Karlsson, P. Tengvall, I. Lundström and H. Arwin, *J. Electrochem. Soc.*, 2002, **149**, C648–C652.

311 T. P. Kunzler, T. Drobek, M. Schuler and N. D. Spencer, *Biomaterials*, 2007, **28**, 2175–2182.

312 T. P. Kunzler, T. Drobek, C. M. Sprecher, M. Schuler and N. D. Spencer, *Appl. Surf. Sci.*, 2006, **253**, 2148–2153.

313 J. C. Meredith, J.-L. Sormana, B. G. Keselowsky, A. J. García, A. Tona, A. Karim and E. J. Amis, *J. Biomed. Mater. Res., Part A*, 2003, **66A**, 483–490.

314 S. V. Roth, M. Burghammer, C. Riekel, P. Müller-Buschbaum, A. Diethert, P. Panagiotou and H. Walter, *Appl. Phys. Lett.*, 2003, **82**, 1935–1937.

315 N. R. Washburn, K. M. Yamada, C. G. Simon Jr, S. B. Kennedy and E. J. Amis, *Biomaterials*, 2004, **25**, 1215–1224.

316 T. Woodfield, C. V. Blitterswijk, J. D. Wijn, T. Sims, A. Hollander and J. Riesle, *Tissue Eng.*, 2005, **11**, 1297–1311.

317 S. H. Oh, I. K. Park, J. M. Kim and J. H. Lee, *Biomaterials*, 2007, **28**, 1664–1671.

318 K. Kreppenhofer, J. Li, R. Segura, L. Popp, M. Rossi, P. Tzvetkova, B. Luy, C. J. Kähler, A. E. Guber and P. A. Levkin, *Langmuir*, 2013, **29**, 3797–3804.

319 S. K. W. Dertinger, D. T. Chiu, N. L. Jeon and G. M. Whitesides, *Anal. Chem.*, 2001, **73**, 1240–1246.

320 N. Li Jeon, H. Baskaran, S. K. W. Dertinger, G. M. Whitesides, L. Van De Water and M. Toner, *Nat. Biotechnol.*, 2002, **20**, 826–830.

321 N. L. Jeon, S. K. W. Dertinger, D. T. Chiu, I. S. Choi, A. D. Stroock and G. M. Whitesides, *Langmuir*, 2000, **16**, 8311–8316.

322 S. K. Sia and G. M. Whitesides, *Electrophoresis*, 2003, **24**, 3563–3576.

323 S.-J. Wang, W. Saadi, F. Lin, C. Minh-Canh Nguyen and N. Li Jeon, *Exp. Cell Res.*, 2004, **300**, 180–189.

324 J. S. Li, E. Ueda, A. Nallapaneni, L. X. Li and P. A. Levkin, *Langmuir*, 2012, **28**, 8286–8291.

325 P. Colombo, C. Vakifahmetoglu and S. Costacurta, *J. Mater. Sci.*, 2010, **45**, 5425–5455.

326 P. Yang, T. Deng, D. Zhao, P. Feng, D. Pine, B. F. Chmelka, G. M. Whitesides and G. D. Stucky, *Science*, 1998, **282**, 2244–2246.

327 K. H. Rhodes, S. A. Davis, F. Caruso, B. Zhang and S. Mann, *Chem. Mater.*, 2000, **12**, 2832–2834.

328 T. Sen, G. J. T. Tiddy, J. L. Casci and M. W. Anderson, *Angew. Chem., Int. Ed.*, 2003, **42**, 4649–4653.

329 D. Kuang, T. Brezesinski and B. Smarsly, *J. Am. Chem. Soc.*, 2004, **126**, 10534–10535.

330 E. S. Toberer and R. Seshadri, *Adv. Mater.*, 2005, **17**, 2244–2246.

331 P. O. Vasiliev, Z. Shen, R. P. Hodgkins and L. Bergström, *Chem. Mater.*, 2006, **18**, 4933–4938.

332 O. Sel, S. Sallard, T. Brezesinski, J. Rathouský, D. R. Dunphy, A. Collord and B. M. Smarsly, *Adv. Funct. Mater.*, 2007, **17**, 3241–3250.

333 Y. Sakatani, C. Boissière, D. Grosso, L. Nicole, G. J. A. A. Soler-Illia and C. Sanchez, *Chem. Mater.*, 2008, **20**, 1049–1056.

334 G. Kaune, M. Memesa, R. Meier, M. A. Ruderer, A. Diethert, S. V. Roth, M. D'Acunzi, J. S. Gutmann and P. Müller-Buschbaum, *ACS Appl. Mater. Interfaces*, 2009, **1**, 2862–2869.

335 Q. Liu and F. Chen, *Mater. Res. Bull.*, 2009, **44**, 2056–2061.

336 V. Karageorgiou and D. Kaplan, *Biomaterials*, 2005, **26**, 5474–5491.

337 F. Vetrone, F. Variola, P. Tambasco de Oliveira, S. F. Zalzal, J.-H. Yi, J. Sam, K. F. Bombonato-Prado, A. Sarkissian, D. F. Perepichka, J. D. Wuest, F. Rosei and A. Nanci, *Nano Lett.*, 2009, **9**, 659–665.

338 K. Nakanishi and N. Tanaka, *Acc. Chem. Res.*, 2007, **40**, 863–873.

339 D. Zhao, J. Feng, Q. Huo, N. Melosh, G. H. Fredrickson, B. F. Chmelka and G. D. Stucky, *Science*, 1998, **279**, 548–552.

340 A. R. Studart, U. T. Gonzenbach, E. Tervoort and L. J. Gauckler, *J. Am. Ceram. Soc.*, 2006, **89**, 1771–1789.

341 J. S. Beck, J. C. Vartuli, W. J. Roth, M. E. Leonowicz, C. T. Kresge, K. D. Schmitt, C. T. W. Chu, D. H. Olson, E. W. Sheppard, S. B. McCullen, J. B. Higgins and J. L. Schlenker, *J. Am. Chem. Soc.*, 1992, **114**, 10834–10843.

342 A. Imhof and D. J. Pine, *Nature*, 1997, **389**, 948–951.

343 B. P. Binks, *Adv. Mater.*, 2002, **14**, 1824–1827.

344 I. Akartuna, A. R. Studart, E. Tervoort and L. J. Gauckler, *Adv. Mater.*, 2008, **20**, 4714–4718.

345 U. T. Gonzenbach, A. R. Studart, E. Tervoort and L. J. Gauckler, *Angew. Chem., Int. Ed.*, 2006, **45**, 3526–3530.

346 T. Sen, G. J. T. Tiddy, J. L. Casci and M. W. Anderson, *Chem. Commun.*, 2003, 2182–2183.

347 S.-W. Choi, J. Xie and Y. Xia, *Adv. Mater.*, 2009, **21**, 2997–3001.

348 A. Boker, Y. Lin, K. Chiapperini, R. Horowitz, M. Thompson, V. Carreon, T. Xu, C. Abetz, H. Skaff, A. D. Dinsmore, T. Emrick and T. P. Russell, *Nat. Mater.*, 2004, **3**, 302–306.

349 Z. Zhai, Y. Wang, Y. Lu and G. Luo, *Ind. Eng. Chem. Res.*, 2010, **49**, 4162–4168.

350 S.-H. Kim, H. Hwang, C. H. Lim, J. W. Shim and S.-M. Yang, *Adv. Funct. Mater.*, 2011, **21**, 1608–1615.

351 M.-J. Zhang, W. Wang, X.-L. Yang, B. Ma, Y.-M. Liu, R. Xie, X.-J. Ju, Z. Liu and L.-Y. Chu, *ACS Appl. Mater. Interfaces*, 2015, **7**, 13758–13767.

352 N. J. Carroll, P. F. Crowder, S. Pylypenko, W. Patterson, D. R. Ratnaweera, D. Perahia, P. Atanassov and D. N. Petsev, *ACS Appl. Mater. Interfaces*, 2013, **5**, 3524–3529.

353 B. H. Jones and T. P. Lodge, *Polym. J.*, 2012, **44**, 131–146.

354 N. J. Carroll, S. Pylypenko, P. B. Atanassov and D. N. Petsev, *Langmuir*, 2009, **25**, 13540–13544.

355 S. Pylypenko, T. S. Olson, N. J. Carroll, D. N. Petsev and P. Atanassov, *J. Phys. Chem. C*, 2010, **114**, 4200–4207.

356 C. E. Ashley, E. C. Carnes, G. K. Phillips, D. Padilla, P. N. Durfee, P. A. Brown, T. N. Hanna, J. Liu, B. Phillips, M. B. Carter, N. J. Carroll, X. Jiang, D. R. Dunphy, C. L. Willman, D. N. Petsev, D. G. Evans, A. N. Parikh, B. Chackerian, W. Wharton, D. S. Peabody and C. J. Brinker, *Nat. Mater.*, 2011, **10**, 389–397.

357 C. E. Ashley, E. C. Carnes, K. E. Epler, D. P. Padilla, G. K. Phillips, R. E. Castillo, D. C. Wilkinson, B. S. Wilkinson, C. A. Burgard, R. M. Kalinich, J. L. Townson, B. Chackerian, C. L. Willman, D. S. Peabody, W. Wharton and C. J. Brinker, *ACS Nano*, 2012, **6**, 2174–2188.

358 Y. Fan, X. Cao, T. Hu, X. Lin, H. Dong and X. Zou, *J. Phys. Chem. C*, 2016, **120**, 3955–3963.

359 M. R. Sommer, M. Schaffner, D. Carnelli and A. R. Studart, *ACS Appl. Mater. Interfaces*, 2016, **8**, 34677–34685.

360 M. R. Sommer, J. R. Vetsch, J. Leemann, R. Müller, A. R. Studart and S. Hofmann, *J. Biomed. Mater. Res., Part B*, 2016, DOI: 10.1002/jbm.b.33737.

361 N. A. Kotov, Y. Liu, S. Wang, C. Cumming, M. Eghtedari, G. Vargas, M. Motamedi, J. Nichols and J. Cortiella, *Langmuir*, 2004, **20**, 7887–7892.

362 Y. Liu, S. Wang, J. W. Lee and N. A. Kotov, *Chem. Mater.*, 2005, **17**, 4918–4924.

363 Y. Zhang, S. Wang, M. Eghtedari, M. Motamedi and N. A. Kotov, *Adv. Funct. Mater.*, 2005, **15**, 725–731.

364 S. J. Bryant, J. L. Cuy, K. D. Hauch and B. D. Ratner, *Biomaterials*, 2007, **28**, 2978–2986.

365 N. V. Dziomkina and G. J. Vancso, *Soft Matter*, 2005, **1**, 265–279.

366 O. Vickreva, O. Kalinina and E. Kumacheva, *Adv. Mater.*, 2000, **12**, 110–112.

367 A. R. Studart, J. Studer, L. Xu, K. Yoon, H. C. Shum and D. A. Weitz, *Langmuir*, 2011, **27**, 955–964.

368 A. D. Dinsmore, M. F. Hsu, M. G. Nikolaides, M. Marquez, A. R. Bausch and D. A. Weitz, *Science*, 2002, **298**, 1006–1009.

369 A. Boker, J. He, T. Emrick and T. P. Russell, *Soft Matter*, 2007, **3**, 1231–1248.

370 Y. Lin, H. Skaff, A. Böker, A. D. Dinsmore, T. Emrick and T. P. Russell, *J. Am. Chem. Soc.*, 2003, **125**, 12690–12691.

371 D. Wang, H. Duan and H. Mohwald, *Soft Matter*, 2005, **1**, 412–416.

372 H. Skaff, Y. Lin, R. Tangirala, K. Breitenkamp, A. Böker, T. P. Russell and T. Emrick, *Adv. Mater.*, 2005, **17**, 2082–2086.

373 A. Donev, I. Cisse, D. Sachs, E. A. Variano, F. H. Stillinger, R. Connelly, S. Torquato and P. M. Chaikin, *Science*, 2004, **303**, 990–993.

374 J. W. Kim, R. J. Larsen and D. A. Weitz, *Adv. Mater.*, 2007, **19**, 2005–2009.

375 R. Aveyard, B. P. Binks and J. H. Clint, *Adv. Colloid Interface Sci.*, 2003, **100**, 503–546.

This journal is © The Royal Society of Chemistry 2017

Chem. Soc. Rev., 2017, **46**, 855–914 | 909

376 A. Fang, C. Gaillard and J.-P. Douliez, *Chem. Mater.*, 2011, **23**, 4660–4662.

377 A. Fang and B. Cathala, *Colloids Surf., B*, 2011, **82**, 81–86.

378 B. Wang, H. C. Shum and D. A. Weitz, *ChemPhysChem*, 2009, **10**, 641–645.

379 D. Dendukuri, S. S. Gu, D. C. Pregibon, T. A. Hatton and P. S. Doyle, *Lab Chip*, 2007, **7**, 818–828.

380 D. Dendukuri, P. Panda, R. Haghgooie, J. M. Kim, T. A. Hatton and P. S. Doyle, *Macromolecules*, 2008, **41**, 8547–8556.

381 D. C. Appleyard, S. C. Chapin, R. L. Srinivas and P. S. Doyle, *Nat. Protoc.*, 2011, **6**, 1761–1774.

382 J.-H. Jang, D. Dendukuri, T. A. Hatton, E. L. Thomas and P. S. Doyle, *Angew. Chem., Int. Ed.*, 2007, **46**, 9027–9031.

383 K. W. Bong, D. C. Pregibon and P. S. Doyle, *Lab Chip*, 2009, **9**, 863–866.

384 D. C. Pregibon, M. Toner and P. S. Doyle, *Science*, 2007, **315**, 1393–1396.

385 R. G. Harrison, *Protein purification process engineering*, CRC Press, Marcel Dekker, New York, 1994.

386 M. V. Badiger, M. E. McNeill and N. B. Graham, *Biomaterials*, 1993, **14**, 1059–1063.

387 M. Li, D. Joung, J. A. Kozinski and D. K. Hwang, *Langmuir*, 2017, **33**, 184–190.

388 R. F. Shepherd, P. Panda, Z. Bao, K. H. Sandhage, T. A. Hatton, J. A. Lewis and P. S. Doyle, *Adv. Mater.*, 2008, **20**, 4734–4739.

389 R. Fan, O. Vermesh, A. Srivastava, B. K. H. Yen, L. Qin, H. Ahmad, G. A. Kwong, C.-C. Liu, J. Gould, L. Hood and J. R. Heath, *Nat. Biotechnol.*, 2008, **26**, 1373–1378.

390 A. V. Fotin, A. L. Drobyshev, D. Y. Proudnikov, A. N. Perov and A. D. Mirzabekov, *Nucleic Acids Res.*, 1998, **26**, 1515–1521.

391 D. C. Pregibon and P. S. Doyle, *Anal. Chem.*, 2009, **81**, 4873–4881.

392 K. W. Bong, K. T. Bong, D. C. Pregibon and P. S. Doyle, *Angew. Chem., Int. Ed.*, 2010, **49**, 87–90.

393 C. L. Lewis, Y. Lin, C. Yang, A. K. Manocchi, K. P. Yuet, P. S. Doyle and H. Yi, *Langmuir*, 2010, **26**, 13436–13441.

394 S. A. Lee, S. E. Chung, W. Park, S. H. Lee and S. Kwon, *Lab Chip*, 2009, **9**, 1670–1675.

395 S. E. Brunker, K. B. Cederquist and C. D. Keating, *Nanomedicine*, 2007, **2**, 695–710.

396 N. H. Finkel, X. Lou, C. Wang and L. He, *Anal. Chem.*, 2004, **76**, 352A–359A.

397 K. B. Cederquist, S. L. Dean and C. D. Keating, *Wiley Interdiscip. Rev.: Nanomed. Nanobiotechnol.*, 2010, **2**, 578–600.

398 K. W. Bong, S. C. Chapin, D. C. Pregibon, D. Baah, T. M. Floyd-Smith and P. S. Doyle, *Lab Chip*, 2011, **11**, 743–747.

399 S. C. Chapin, D. C. Appleyard, D. C. Pregibon and P. S. Doyle, *Angew. Chem., Int. Ed.*, 2011, **50**, 2289–2293.

400 S. C. Chapin, D. C. Pregibon and P. S. Doyle, *Lab Chip*, 2009, **9**, 3100–3109.

401 C. A. Mirkin, C. S. Thaxton and N. L. Rosi, *Expert Rev. Mol. Diagn.*, 2004, **4**, 749–751.

402 D. C. Appleyard, S. C. Chapin and P. S. Doyle, *Anal. Chem.*, 2011, **83**, 193–199.

403 S. C. Chapin and P. S. Doyle, *Anal. Chem.*, 2011, **83**, 7179–7185.

404 R. L. Srinivas, S. C. Chapin and P. S. Doyle, *Anal. Chem.*, 2011, **83**, 9138–9145.

405 S. K. Suh, S. C. Chapin, T. A. Hatton and P. S. Doyle, *Microfluid. Nanofluid.*, 2012, **13**, 665–674.

406 J. Lee, P. W. Bisso, R. L. Srinivas, J. J. Kim, A. J. Swiston and P. S. Doyle, *Nat. Mater.*, 2014, **13**, 524–529.

407 Y. Xia and G. M. Whitesides, *Annu. Rev. Mater. Sci.*, 1998, **28**, 153–184.

408 D. K. Hwang, J. Oakey, M. Toner, J. A. Arthur, K. S. Anseth, S. Lee, A. Zeiger, K. J. Van Vliet and P. S. Doyle, *J. Am. Chem. Soc.*, 2009, **131**, 4499–4504.

409 M. Li, M. Humayun, J. A. Kozinski and D. K. Hwang, *Langmuir*, 2014, **30**, 8637–8644.

410 H. Wei, B.-H. Chueh, H. Wu, E. W. Hall, C.-W. Li, R. Schirhagl, J.-M. Lin and R. N. Zare, *Lab Chip*, 2011, **11**, 238–245.

411 S. Yamamura, H. Kishi, Y. Tokimitsu, S. Kondo, R. Honda, S. R. Rao, M. Omori, E. Tamiya and A. Muraguchi, *Anal. Chem.*, 2005, **77**, 8050–8056.

412 Y.-S. Hwang, B. G. Chung, D. Ortmann, N. Hattori, H.-C. Moeller and A. Khademhosseini, *Proc. Natl. Acad. Sci. U. S. A.*, 2009, **106**, 16978–16983.

413 S. Selimovic, F. Piraino, H. Bae, M. Rasponi, A. Redaelli and A. Khademhosseini, *Lab Chip*, 2011, **11**, 2325–2332.

414 Y. S. Schiffenbauer, Y. Kalma, E. Trubniykov, O. Gal-Garber, L. Weisz, A. Halamish, M. Sister and G. Berke, *Lab Chip*, 2009, **9**, 2965–2972.

415 J. R. Bostwick and W.-D. Le, *Anal. Biochem.*, 1991, **192**, 125–130.

416 C. Rensch, S. Hell, M. V. Schickfus and S. Hunklinger, *Appl. Opt.*, 1989, **28**, 3754–3758.

417 L. P. Ghislain, V. B. Elings, K. B. Crozier, S. R. Manalis, S. C. Minne, K. Wilder, G. S. Kino and C. F. Quate, *Appl. Phys. Lett.*, 1999, **74**, 501–503.

418 A. Revzin, R. J. Russell, V. K. Yadavalli, W.-G. Koh, C. Deister, D. D. Hile, M. B. Mellott and M. V. Pishko, *Langmuir*, 2001, **17**, 5440–5447.

419 D. Qin, Y. Xia and G. M. Whitesides, *Adv. Mater.*, 1996, **8**, 917–919.

420 B. D. Gates, Q. Xu, M. Stewart, D. Ryan, C. G. Willson and G. M. Whitesides, *Chem. Rev.*, 2005, **105**, 1171–1196.

421 L. Ren, Q. Wu, C. Yang, L. Zhu, C. Li, P. Zhang, H. Zhang, X. Meng and F.-S. Xiao, *J. Am. Chem. Soc.*, 2012, **134**, 15173–15176.

422 Z. Shan, Z. Lu, L. Wang, C. Zhou, L. Ren, L. Zhang, X. Meng, S. Ma and F.-S. Xiao, *ChemCatChem*, 2010, **2**, 407–412.

423 S. Proch, J. Herrmannsdörfer, R. Kempe, C. Kern, A. Jess, L. Seyfarth and J. Senker, *Chem. – Eur. J.*, 2008, **14**, 8204–8212.

424 F.-S. Xiao, L. Wang, C. Yin, K. Lin, Y. Di, J. Li, R. Xu, D. S. Su, R. Schlögl, T. Yokoi and T. Tatsumi, *Angew. Chem.*, 2006, **118**, 3162–3165.

425 F.-S. Xiao, L. Wang, C. Yin, K. Lin, Y. Di, J. Li, R. Xu, D. S. Su, R. Schlögl, T. Yokoi and T. Tatsumi, *Angew. Chem., Int. Ed.*, 2006, **45**, 3090–3093.

910 | *Chem. Soc. Rev.*, 2017, **46**, 855–914

This journal is © The Royal Society of Chemistry 2017

426 U. Balakrishnan, N. Ananthi, S. T. Selvan, R. Pal, K. Ariga, S. Velmathi and A. Vinu, *Chem. – Asian J.*, 2010, **5**, 897–903.

427 S. Wu, Y. Han, Y.-C. Zou, J.-W. Song, L. Zhao, Y. Di, S.-Z. Liu and F.-S. Xiao, *Chem. Mater.*, 2004, **16**, 486–492.

428 F.-S. Xiao, Y. Han, Y. Yu, X. Meng, M. Yang and S. Wu, *J. Am. Chem. Soc.*, 2002, **124**, 888–889.

429 B. Frank, M. Morassutto, R. Schomäcker, R. Schlögl and D. S. Su, *ChemCatChem*, 2010, **2**, 644–648.

430 X. Liu, B. Frank, W. Zhang, T. P. Cotter, R. Schlögl and D. S. Su, *Angew. Chem.*, 2011, **123**, 3376–3380.

431 X. Liu, B. Frank, W. Zhang, T. P. Cotter, R. Schlögl and D. S. Su, *Angew. Chem., Int. Ed.*, 2011, **50**, 3318–3322.

432 L. Shao, W. Zhang, M. Armbrüster, D. Teschner, F. Girgsdies, B. Zhang, O. Timpe, M. Friedrich, R. Schlögl and D. S. Su, *Angew. Chem.*, 2011, **123**, 10414–10418.

433 L. Shao, W. Zhang, M. Armbrüster, D. Teschner, F. Girgsdies, B. Zhang, O. Timpe, M. Friedrich, R. Schlögl and D. S. Su, *Angew. Chem., Int. Ed.*, 2011, **50**, 10231–10235.

434 D. S. Su, *ChemSusChem*, 2011, **4**, 811–813.

435 J.-P. Tessonnier, M. Becker, W. Xia, F. Girgsdies, R. Blume, L. Yao, D. S. Su, M. Muhler and R. Schlögl, *ChemCatChem*, 2010, **2**, 1559–1561.

436 M. A. Al-Daous and A. Stein, *Chem. Mater.*, 2003, **15**, 2638–2645.

437 B. T. Holland, C. F. Blanford and A. Stein, *Science*, 1998, **281**, 538–540.

438 G. S. Chai, I. S. Shin and J. S. Yu, *Adv. Mater.*, 2004, **16**, 2057–2061.

439 A. Stein and R. C. Schroden, *Curr. Opin. Solid State Mater. Sci.*, 2001, **5**, 553–564.

440 X.-Y. Yang, A. Leonard, A. Lemaire, G. Tian and B.-L. Su, *Chem. Commun.*, 2011, **47**, 2763–2786.

441 X.-Y. Yang, G. Tian, L.-H. Chen, Y. Li, J. C. Rooke, Y.-X. Wei, Z.-M. Liu, Z. Deng, G. Van Tendeloo and B.-L. Su, *Chem. – Eur. J.*, 2011, **17**, 14987–14995.

442 Y.-L. Zhang, S. Liu, S. Liu, F. Liu, H. Zhang, Y. He and F.-S. Xiao, *Catal. Commun.*, 2011, **12**, 1212–1217.

443 R. V. Wasielewski, M. Mengel, S. Gignac, L. Wilkens, M. Werner and A. Georgii, *J. Histochem. Cytochem.*, 1997, **45**, 1455–1459.

444 M. Choi, H. S. Cho, R. Srivastava, C. Venkatesan, D.-H. Choi and R. Ryoo, *Nat. Mater.*, 2006, **5**, 718–723.

445 Q. Liu, X. Guo, Y. Li and W. Shen, *Langmuir*, 2009, **25**, 6425–6430.

446 J. P. Nolan and L. A. Sklar, *Trends Biotechnol.*, 2002, **20**, 9–12.

447 N. Christodoulides, S. Mohanty, C. S. Miller, M. C. Langub, P. N. Floriano, P. Dharshan, M. F. Ali, B. Bernard, D. Romanovicz and E. Anslyn, *Lab Chip*, 2005, **5**, 261–269.

448 N. Christodoulides, M. Tran, P. N. Floriano, M. Rodriguez, A. Goodey, M. Ali, D. Neikirk and J. T. McDevitt, *Anal. Chem.*, 2002, **74**, 3030–3036.

449 Y. Xia, B. Gates and Z. Y. Li, *Adv. Mater.*, 2001, **13**, 409–413.

450 J. E. G. J. Wijnhoven and W. L. Vos, *Science*, 1998, **281**, 802–804.

451 Y. A. Vlasov, X.-Z. Bo, J. C. Sturm and D. J. Norris, *Nature*, 2001, **414**, 289–293.

452 W. Cheng, J. Wang, U. Jonas, G. Fytas and N. Stefanou, *Nat. Mater.*, 2006, **5**, 830–836.

453 M. Trau and B. Battersby, *Adv. Mater.*, 2001, **13**, 975–979.

454 L. Yang, D. K. Tran and X. Wang, *Genome Res.*, 2001, **11**, 1888–1898.

455 P. S. Eastman, W. Ruan, M. Doctolero, R. Nuttall, G. de Feo, J. S. Park, J. S. F. Chu, P. Cooke, J. W. Gray, S. Li and F. F. Chen, *Nano Lett.*, 2006, **6**, 1059–1064.

456 H. Xu, M. Y. Sha, E. Y. Wong, J. Uphoff, Y. Xu, J. A. Treadway, A. Truong, E. O'Brien, S. Asquith, M. Stubbins, N. K. Spurr, E. H. Lai and W. Mahoney, *Nucleic Acids Res.*, 2003, **31**, e43.

457 B. J. Battersby, D. Bryant, W. Meutermans, D. Matthews, M. L. Smythe and M. Trau, *J. Am. Chem. Soc.*, 2000, **122**, 2138–2139.

458 M. Han, X. Gao, J. Z. Su and S. Nie, *Nat. Biotechnol.*, 2001, **19**, 631–635.

459 D. Wang, A. L. Rogach and F. Caruso, *Nano Lett.*, 2002, **2**, 857–861.

460 M. Kuang, D. Wang, H. Bao, M. Gao, H. Möhwald and M. Jiang, *Adv. Mater.*, 2005, **17**, 267–270.

461 F. Cunin, T. A. Schmedake, J. R. Link, Y. Y. Li, J. Koh, S. N. Bhatia and M. J. Sailor, *Nat. Mater.*, 2002, **1**, 39–41.

462 J. H. Holtz and S. A. Asher, *Nature*, 1997, **389**, 829–832.

463 B. H. King, A. M. Ruminski, J. L. Snyder and M. J. Sailor, *Adv. Mater.*, 2007, **19**, 4530–4534.

464 M. M. Orosco, C. Pacholski and M. J. Sailor, *Nat. Nanotechnol.*, 2009, **4**, 255–258.

465 J. D. Debord and L. A. Lyon, *J. Phys. Chem. B*, 2000, **104**, 6327–6331.

466 Z. Hu, X. Lu and J. Gao, *Adv. Mater.*, 2001, **13**, 1708–1712.

467 Y. Takeoka and M. Watanabe, *Langmuir*, 2003, **19**, 9104–9106.

468 S. Kubo, Z.-Z. Gu, K. Takahashi, A. Fujishima, H. Segawa and O. Sato, *J. Am. Chem. Soc.*, 2004, **126**, 8314–8319.

469 T. Kanai, D. Lee, H. C. Shum and D. A. Weitz, *Small*, 2010, **6**, 807–810.

470 J. Y. Wang, Y. Cao, Y. Feng, F. Yin and J. P. Gao, *Adv. Mater.*, 2007, **19**, 3865–3871.

471 H. Li, J. Wang, L. Yang and Y. Song, *Adv. Funct. Mater.*, 2008, **18**, 3258–3264.

472 P. Kang, S. O. Ogunbo and D. Erickson, *Langmuir*, 2011, **27**, 9676–9680.

473 Z. Wang, J. Zhang, J. Xie, Z. Wang, Y. Yin, J. Li, Y. Li, S. Liang, L. Zhang, L. Cui, H. Zhang and B. Yang, *J. Mater. Chem.*, 2012, **22**, 7887–7893.

474 E. Tian, J. Wang, Y. Zheng, Y. Song, L. Jiang and D. Zhu, *J. Mater. Chem.*, 2008, **18**, 1116–1122.

475 J. H. Kim, J. H. Moon, S.-Y. Lee and J. Park, *Appl. Phys. Lett.*, 2010, **97**, 103701.

476 R. Xuan, Q. Wu, Y. Yin and J. Ge, *J. Mater. Chem.*, 2011, **21**, 3672–3676.

477 A. C. Arsenault, T. J. Clark, G. von Freymann, L. Cademartiri, R. Sapienza, J. Bertolotti, E. Vekris, S. Wong, V. Kitaev, I. Manners, R. Z. Wang, S. John, D. Wiersma and G. A. Ozin, *Nat. Mater.*, 2006, **5**, 179–184.

This journal is © The Royal Society of Chemistry 2017

Chem. Soc. Rev., 2017, **46**, 855–914 | 911

478 H. Fudouzi and T. Sawada, *Langmuir*, 2006, **22**, 1365–1368.

479 Y. J. Lee and P. V. Braun, *Adv. Mater.*, 2003, **15**, 563–566.

480 J. Wang and Y. Han, *Langmuir*, 2009, **25**, 1855–1864.

481 H. Saito, Y. Takeoka and M. Watanabe, *Chem. Commun.*, 2003, 2126–2127.

482 Y. Kang, J. J. Walish, T. Gorishnyy and E. L. Thomas, *Nat. Mater.*, 2007, **6**, 957–960.

483 Y. Ahn, E. Kim, J. Hyon, C. Kang and Y. Kang, *Adv. Mater.*, 2012, **24**, OP127–OP130.

484 M. Kamenjicki, I. K. Lednev, A. Mikhonin, R. Kesavamoorthy and S. A. Asher, *Adv. Funct. Mater.*, 2003, **13**, 774–780.

485 K. Matsubara, M. Watanabe and Y. Takeoka, *Angew. Chem., Int. Ed.*, 2007, **46**, 1688–1692.

486 T. S. Shim, S.-H. Kim, J. Y. Sim, J.-M. Lim and S.-M. Yang, *Adv. Mater.*, 2010, **22**, 4494–4498.

487 E. Redel, J. Mlynarski, J. Moir, A. Jelle, C. Huai, S. Petrov, M. G. Helander, F. C. Peiris, G. von Freymann and G. A. Ozin, *Adv. Mater.*, 2012, **24**, OP265–OP269.

488 M. G. Han, C. G. Shin, S.-J. Jeon, H. Shim, C.-J. Heo, H. Jin, J. W. Kim and S. Lee, *Adv. Mater.*, 2012, **24**, 6438–6444.

489 J. Ge, Y. Hu and Y. Yin, *Angew. Chem., Int. Ed.*, 2007, **46**, 7428–7431.

490 L. Xu, J. Wang, Y. Song and L. Jiang, *Chem. Mater.*, 2008, **20**, 3554–3556.

491 J. Kim, Y. Song, L. He, H. Kim, H. Lee, W. Park, Y. Yin and S. Kwon, *Small*, 2011, **7**, 1163–1168.

492 S. Wong, V. Kitaev and G. A. Ozin, *J. Am. Chem. Soc.*, 2003, **125**, 15589–15598.

493 P. Jiang, J. F. Bertone, K. S. Hwang and V. L. Colvin, *Chem. Mater.*, 1999, **11**, 2132–2140.

494 A. Mihi, M. Ocaña and H. Míguez, *Adv. Mater.*, 2006, **18**, 2244–2249.

495 P. Jiang and M. J. McFarland, *J. Am. Chem. Soc.*, 2004, **126**, 13778–13786.

496 P. A. Rundquist, P. Photinos, S. Jagannathan and S. A. Asher, *J. Chem. Phys.*, 1989, **91**, 4932–4941.

497 S. A. Asher, J. Holtz, L. Liu and Z. Wu, *J. Am. Chem. Soc.*, 1994, **116**, 4997–4998.

498 S.-H. Kim, S.-J. Jeon, W. C. Jeong, H. S. Park and S.-M. Yang, *Adv. Mater.*, 2008, **20**, 4129–4134.

499 O. D. Velev and S. Gupta, *Adv. Mater.*, 2009, **21**, 1897–1905.

500 S.-H. Kim, S. Y. Lee, G.-R. Yi, D. J. Pine and S.-M. Yang, *J. Am. Chem. Soc.*, 2006, **128**, 10897–10904.

501 S.-H. Kim, S.-J. Jeon and S.-M. Yang, *J. Am. Chem. Soc.*, 2008, **130**, 6040–6046.

502 Z.-Z. Gu, S. Kubo, W. Qian, Y. Einaga, D. A. Tryk, A. Fujishima and O. Sato, *Langmuir*, 2001, **17**, 6751–6753.

503 H. Gu, Y. Zhao, Y. Cheng, Z. Xie, F. Rong, J. Li, B. Wang, D. Fu and Z. Gu, *Small*, 2013, **9**, 2266–2271.

504 M. Kuang, J. Wang, B. Bao, F. Li, L. Wang, L. Jiang and Y. Song, *Adv. Opt. Mater.*, 2014, **2**, 34–38.

505 E. V. Anslyn and V. M. Rotello, *Curr. Opin. Chem. Biol.*, 2010, **14**, 683–684.

506 M. Kyo, K. Usui-Aoki and H. Koga, *Anal. Chem.*, 2005, **77**, 7115–7121.

507 M. P. Schwartz, S. D. Alvarez and M. J. Sailor, *Anal. Chem.*, 2007, **79**, 327–334.

508 J. L. Urraca, M. C. Moreno-Bondi, G. Orellana, B. Sellergren and A. J. Hall, *Anal. Chem.*, 2007, **79**, 4915–4923.

509 Z. Xie, K. Cao, Y. Zhao, L. Bai, H. Gu, H. Xu and Z.-Z. Gu, *Adv. Mater.*, 2014, **26**, 2413–2418.

510 J. Ge and Y. Yin, *Angew. Chem., Int. Ed.*, 2011, **50**, 1492–1522.

511 W. Shen, M. Li, C. Ye, L. Jiang and Y. Song, *Lab Chip*, 2012, **12**, 3089–3095.

512 B. Ye, F. Rong, H. Gu, Z. Xie, Y. Cheng, Y. Zhao and Z. Gu, *Chem. Commun.*, 2013, **49**, 5331–5333.

513 H. Zhang, Y. Liu, D. Yao and B. Yang, *Chem. Soc. Rev.*, 2012, **41**, 6066–6088.

514 Z. Mao, H. Xu and D. Wang, *Adv. Funct. Mater.*, 2010, **20**, 1053–1074.

515 K. D. Hermanson, S. O. Lumsdon, J. P. Williams, E. W. Kaler and O. D. Velev, *Science*, 2001, **294**, 1082–1086.

516 J. F. Galisteo-López, M. Ibisate, R. Sapienza, L. S. Froufe-Pérez, Á. Blanco and C. López, *Adv. Mater.*, 2011, **23**, 30–69.

517 S.-H. Kim, S. Y. Lee, S.-M. Yang and G.-R. Yi, *NPG Asia Mater.*, 2011, **3**, 25–33.

518 P. S. Dittrich and A. Manz, *Nat. Rev. Drug Discovery*, 2006, **5**, 210–218.

519 R. Langer, *Nature*, 1998, **392**, 5–10.

520 D. A. LaVan, T. McGuire and R. Langer, *Nat. Biotechnol.*, 2003, **21**, 1184–1191.

521 H. A. Santos, *Biomatter*, 2012, **2**, 237–238.

522 T. M. Allen and P. R. Cullis, *Science*, 2004, **303**, 1818–1822.

523 H. A. Santos and J. Hirvonen, *Nanomedicine*, 2012, **7**, 1281–1284.

524 D. Liu, B. Herranz-Blanco, E. Mäkilä, L. R. Arriaga, S. Mirza, D. A. Weitz, N. Sandler, J. Salonen, J. Hirvonen and H. A. Santos, *ACS Appl. Mater. Interfaces*, 2013, **5**, 12127–12134.

525 E. J. Anglin, L. Cheng, W. R. Freeman and M. J. Sailor, *Adv. Drug Delivery Rev.*, 2008, **60**, 1266–1277.

526 L. M. Bimbo, M. Sarparanta, H. A. Santos, A. J. Airaksinen, E. Mäkilä, T. Laaksonen, L. Peltonen, V.-P. Lehto, J. Hirvonen and J. Salonen, *ACS Nano*, 2010, **4**, 3023–3032.

527 S. P. Low, N. H. Voelcker, L. T. Canham and K. A. Williams, *Biomaterials*, 2009, **30**, 2873–2880.

528 A. Rosengren, L. Wallman, M. Bengtsson, T. Laurell, N. Danielsen and L. M. Bjursten, *Phys. Status Solidi A*, 2000, **182**, 527–531.

529 T. Tanaka, B. Godin, R. Bhavane, R. Nieves-Alicea, J. Gu, X. Liu, C. Chiappini, J. R. Fakhoury, S. Amra, A. Ewing, Q. Li, I. J. Fidler and M. Ferrari, *Int. J. Pharm.*, 2010, **402**, 190–197.

530 J.-H. Park, L. Gu, G. von Maltzahn, E. Ruoslahti, S. N. Bhatia and M. J. Sailor, *Nat. Mater.*, 2009, **8**, 331–336.

531 B. Godin, J. Gu, R. E. Serda, R. Bhavane, E. Tasciotti, C. Chiappini, X. Liu, T. Tanaka, P. Decuzzi and M. Ferrari, *J. Biomed. Mater. Res., Part A*, 2010, **94A**, 1236–1243.

532 X. Huang and B. Voit, *Polym. Chem.*, 2013, **4**, 435–443.

533 W. Wang, M.-J. Zhang, R. Xie, X.-J. Ju, C. Yang, C.-L. Mou, D. A. Weitz and L.-Y. Chu, *Angew. Chem., Int. Ed.*, 2013, **52**, 8084–8087.

912 | *Chem. Soc. Rev.*, 2017, **46**, 855–914

This journal is © The Royal Society of Chemistry 2017

534 H. A. Santos, L. M. Bimbo, V.-P. Lehto, A. J. Airaksinen, J. Salonen and J. Hirvonen, *Curr. Drug Discovery Technol.*, 2011, **8**, 228–249.

535 H. Jaganathan and B. Godin, *Adv. Drug Delivery Rev.*, 2012, **64**, 1800–1819.

536 L. M. Bimbo, O. V. Denisova, E. Mäkilä, M. Kaasalainen, J. K. De Brabander, J. Hirvonen, J. Salonen, L. Kakkola, D. Kainov and H. A. Santos, *ACS Nano*, 2013, **7**, 6884–6893.

537 P. J. Kinnari, M. L. K. Hyvönen, E. M. Mäkilä, M. H. Kaasalainen, A. Rivinoja, J. J. Salonen, J. T. Hirvonen, P. M. Laakkonen and H. A. Santos, *Biomaterials*, 2013, **34**, 9134–9141.

538 D. Liu, L. M. Bimbo, E. Mäkilä, F. Villanova, M. Kaasalainen, B. Herranz-Blanco, C. M. Caramella, V.-P. Lehto, J. Salonen, K.-H. Herzig, J. Hirvonen and H. A. Santos, *J. Controlled Release*, 2013, **170**, 268–278.

539 L. T. Canham, C. L. Reeves, J. P. Newey, M. R. Houlton, T. I. Cox, J. M. Buriak and M. P. Stewart, *Adv. Mater.*, 1999, **11**, 1505–1507.

540 M.-A. Shahbazi, M. Hamidi, E. M. Mäkilä, H. Zhang, P. V. Almeida, M. Kaasalainen, J. J. Salonen, J. T. Hirvonen and H. A. Santos, *Biomaterials*, 2013, **34**, 7776–7789.

541 J. Liu, X. Jiang, C. Ashley and C. J. Brinker, *J. Am. Chem. Soc.*, 2009, **131**, 7567–7569.

542 M. Vallet-Regí, F. Balas and D. Arcos, *Angew. Chem., Int. Ed.*, 2007, **46**, 7548–7558.

543 R. Langer and J. Vacanti, *Science*, 1993, **260**, 920–926.

544 M. P. Lutolf and J. A. Hubbell, *Nat. Biotechnol.*, 2005, **23**, 47–55.

545 S. E. Kim, J. H. Park, Y. W. Cho, H. Chung, S. Y. Jeong, E. B. Lee and I. C. Kwon, *J. Controlled Release*, 2003, **91**, 365–374.

546 R. Langer and D. A. Tirrell, *Nature*, 2004, **428**, 487–492.

547 D. Horák, F. Lednický, V. Řehák and F. Švec, *J. Appl. Polym. Sci.*, 1993, **49**, 2041–2050.

548 S. Bhat, A. Tripathi and A. Kumar, *J. R. Soc., Interface*, 2011, **8**, 540–554.

549 K. Bloch, A. Vanichkin, L. G. Damshkaln, V. I. Lozinsky and P. Vardi, *Acta Biomater.*, 2010, **6**, 1200–1205.

550 M. B. Dainiak, I. U. Allan, I. N. Savina, L. Cornelio, E. S. James, S. L. James, S. V. Mikhalovsky, H. Jungvid and I. Y. Galaev, *Biomaterials*, 2010, **31**, 67–76.

551 M. Jurga, M. B. Dainiak, A. Sarnowska, A. Jablonska, A. Tripathi, F. M. Plieva, I. N. Savina, L. Strojek, H. Jungvid, A. Kumar, B. Lukomska, K. Domanska-Janik, N. Forraz and C. P. McGuckin, *Biomaterials*, 2011, **32**, 3423–3434.

552 N. Kathuria, A. Tripathi, K. K. Kar and A. Kumar, *Acta Biomater.*, 2009, **5**, 406–418.

553 G. Akay, M. A. Birch and M. A. Bokhari, *Biomaterials*, 2004, **25**, 3991–4000.

554 M. W. Hayman, K. H. Smith, N. R. Cameron and S. A. Przyborski, *Biochem. Biophys. Res. Commun.*, 2004, **314**, 483–488.

555 M. A. Bokhari, G. Akay, S. Zhang and M. A. Birch, *Biomaterials*, 2005, **26**, 5198–5208.

556 A. Barbetta, M. Massimi, L. Conti Devirgiliis and M. Dentini, *Biomacromolecules*, 2006, **7**, 3059–3068.

557 R. S. Moglia, J. L. Holm, N. A. Sears, C. J. Wilson, D. M. Harrison and E. Cosgriff-Hernandez, *Biomacromolecules*, 2011, **12**, 3621–3628.

558 S. Zhou, A. Bismarck and J. H. G. Steinke, *J. Mater. Chem. B*, 2013, **1**, 4736–4745.

559 J. L. Robinson, R. S. Moglia, M. C. Stuebben, M. A. McEnery and E. Cosgriff-Hernandez, *Tissue Eng., Part A*, 2014, **20**, 1103–1112.

560 S. Caldwell, D. W. Johnson, M. P. Didsbury, B. A. Murray, J. J. Wu, S. A. Przyborski and N. R. Cameron, *Soft Matter*, 2012, **8**, 10344–10351.

561 P. Tayalia, C. R. Mendonca, T. Baldacchini, D. J. Mooney and E. Mazur, *Adv. Mater.*, 2008, **20**, 4494–4498.

562 D. Wang, E. McLaughlin, R. Pfeffer and Y. S. Lin, *Chem. Eng. J.*, 2011, **168**, 1201–1208.

563 M. O. Adebajo, R. L. Frost, J. T. Kloprogge, O. Carmody and S. Kokot, *J. Porous Mater.*, 2003, **10**, 159–170.

564 Y. Zhang, S. Wei, F. Liu, Y. Du, S. Liu, Y. Ji, T. Yokoi, T. Tatsumi and F.-S. Xiao, *Nano Today*, 2009, **4**, 135–142.

565 Z. Yue, C. Mangun, J. Economy, P. Kemme, D. Cropek and S. Maloney, *Environ. Sci. Technol.*, 2001, **35**, 2844–2848.

566 E. J. Bouwer and P. B. Crowe, *J. – Am. Water Works Assoc.*, 1988, **80**, 82–93.

567 D. Ceylan, S. Dogu, B. Karacik, S. D. Yakan, O. S. Okay and O. Okay, *Environ. Sci. Technol.*, 2009, **43**, 3846–3852.

568 S. Panpanit and C. Visvanathan, *J. Membr. Sci.*, 2001, **184**, 59–68.

569 M. Inagaki, A. Kawahara, Y. Nishi and N. Iwashita, *Carbon*, 2002, **40**, 1487–1492.

570 X. Gui, H. Li, K. Wang, J. Wei, Y. Jia, Z. Li, L. Fan, A. Cao, H. Zhu and D. Wu, *Acta Mater.*, 2011, **59**, 4798–4804.

571 H. H. Sokker, N. M. El-Sawy, M. A. Hassan and B. E. El-Anadouli, *J. Hazard. Mater.*, 2011, **190**, 359–365.

572 A. Li, H.-X. Sun, D.-Z. Tan, W.-J. Fan, S.-H. Wen, X.-J. Qing, G.-X. Li, S.-Y. Li and W.-Q. Deng, *Energy Environ. Sci.*, 2011, **4**, 2062–2065.

573 O. Carmody, R. Frost, Y. Xi and S. Kokot, *J. Therm. Anal. Calorim.*, 2008, **91**, 809–816.

574 C. Yang, U. Kaipa, Q. Z. Mather, X. Wang, V. Nesterov, A. F. Venero and M. A. Omary, *J. Am. Chem. Soc.*, 2011, **133**, 18094–18097.

575 J. G. Reynolds, P. R. Coronado and L. W. Hrubesh, *J. Non-Cryst. Solids*, 2001, **292**, 127–137.

576 V. G. Parale, D. B. Mahadik, M. S. Kavale, A. V. Rao, P. B. Wagh and S. C. Gupta, *Soft Nanosci. Lett.*, 2011, **1**, 97–104.

577 Q. Zhu, F. Tao and Q. Pan, *ACS Appl. Mater. Interfaces*, 2010, **2**, 3141–3146.

578 A. Abbaspourrad, N. J. Carroll, S.-H. Kim and D. A. Weitz, *Adv. Mater.*, 2013, **25**, 3215–3221.

579 M. Bosnes, A. Deggerdal, A. Rian, L. Korsnes and F. Larsen, in *Scientific and Clinical Applications of Magnetic Carriers*, ed. U. Häfeli, W. Schütt, J. Teller and M. Zborowski, Springer US, Boston, MA, 1997, pp. 269–285.

This journal is © The Royal Society of Chemistry 2017

Chem. Soc. Rev., 2017, **46**, 855–914 | 913

580 A. S. Dynal, *Biomagnetic Techniques in Molecular Biology*, Dynal Corp., Oslo, Norway, 1998, 3rd edn.

581 S. Derveaux, B. G. Stubbe, K. Braeckmans, C. Roelant, K. Sato, J. Demeester and S. C. De Smedt, *Anal. Bioanal. Chem.*, 2008, **391**, 2453–2467.

582 S. Chan, P. Fauchet, Y. Li, L. Rothberg and B. Miller, *Phys. Status Solidi A*, 2000, **182**, 541–546.

583 J. Zhang, X. Liu, S. Wu, M. Xu, X. Guo and S. Wang, *J. Mater. Chem.*, 2010, **20**, 6453–6459.

584 C. Sun, S. Rajasekhara, Y. Chen and J. B. Goodenough, *Chem. Commun.*, 2011, **47**, 12852–12854.

585 D. Dendukuri, T. A. Hatton and P. S. Doyle, *Langmuir*, 2007, **23**, 4669–4674.

586 S. F. Kingsmore, *Nat. Rev. Drug Discovery*, 2006, **5**, 310–321.

587 K. Haupt, *Analyst*, 2001, **126**, 747–756.

588 M. Zourob, S. Mohr, A. G. Mayes, A. Macaskill, N. Perez-Moral, P. R. Fielden and N. J. Goddard, *Lab Chip*, 2006, **6**, 296–301.

589 R. Wilson, A. R. Cossins and D. G. Spiller, *Angew. Chem., Int. Ed.*, 2006, **45**, 6104–6117.

590 A. A. Ellington, I. J. Kullo, K. R. Bailey and G. G. Klee, *Clin. Chem.*, 2010, **56**, 186–193.

591 Q. Fu, J. Zhu and J. E. Van Eyk, *Clin. Chem.*, 2010, **56**, 314–318.

592 N. D. Petkovich and A. Stein, *Hierarchically Structured Porous Materials*, Wiley-VCH Verlag GmbH & Co. KGaA, 2011, pp. 55–129.

593 W. Li, E. W. K. Young, M. Seo, Z. Nie, P. Garstecki, C. A. Simmons and E. Kumacheva, *Soft Matter*, 2008, **4**, 258–262.

594 T. Nisisako, T. Torii, T. Takahashi and Y. Takizawa, *Adv. Mater.*, 2006, **18**, 1152–1156.